Low Power, High Throughput Continuous Flow PCR Instruments for Environmental Applications

by

Tathagata Ray

A Dissertation Presented in Partial Fulfillment
of the Requirements for the Degree
Doctor of Philosophy

Approved November 2013 by the
Graduate Supervisory Committee:

Cody Youngbull, Co-Chair
Michael Goryll, Co-Chair
Jennifer Blain Christen
Hongyu Yu

ARIZONA STATE UNIVERSITY

December 2013

ABSTRACT

Continuous monitoring in the adequate temporal and spatial scale is necessary for a better understanding of environmental variations. But field deployments of molecular biological analysis platforms in that scale are currently hindered because of issues with power, throughput and automation. Currently, such analysis is performed by the collection of large sample volumes from over a wide area and transporting them to laboratory testing facilities, which fail to provide any real-time information.

This dissertation evaluates the systems currently utilized for *in-situ* field analyses and the issues hampering the successful deployment of such bioanalytial instruments for environmental applications. The design and development of high throughput, low power, and autonomous Polymerase Chain Reaction (PCR) instruments, amenable for portable field operations capable of providing quantitative results is presented here as part of this dissertation.

A number of novel innovations have been reported here as part of this work in microfluidic design, PCR thermocycler design, optical design and systems integration. Emulsion microfluidics in conjunction with fluorinated oils and Teflon tubing have been used for the fluidic module that reduces cross-contamination eliminating the need for disposable components or constant cleaning. A cylindrical heater has been designed with the tubing wrapped around fixed temperature zones enabling continuous operation. Fluorescence excitation and detection have been achieved by using a light emitting diode (LED) as the excitation source and a photomultiplier tube (PMT) as the detector. Real-time quantitative PCR results were obtained by using multi-channel fluorescence excitation and detection using LED, optical fibers and a 64-channel multi-anode PMT for measuring continuous real-time fluorescence. The instrument was evaluated by comparing the results obtained with those obtained from a commercial instrument and

found to be comparable. To further improve the design and enhance its field portability, this dissertation also presents a framework for the instrumentation necessary for a portable digital PCR platform to achieve higher throughputs with lower power.

Both systems were designed such that it can easily couple with any upstream platform capable of providing nucleic acid for analysis using standard fluidic connections. Consequently, these instruments can be used not only in environmental applications, but portable diagnostics applications as well.

To my wife Sandhita

ACKNOWLEDGMENTS

I would like to express my sincere gratitude to my advisor, Dr. Cody Youngbbull for his supervision and support during the course of my graduate studies. I owe much respect and gratefulness to Dr. Andrew Hatch, for his guidance and help with his technical knowledge and expertise. I am extremely grateful to my co-chair Dr. Michael Goryll for all his mentoring and encouragement throughout my graduate studies. I also want to thank my committee members, Dr. Jennifer Blain Christen and Dr. Hongyu Yu for taking an interest in my work and providing valuable advise to me.

I would also like to extend my gratitude to the engineering support staff at CSSER for their valuable suggestions and assistance with the microfabrication work. My heartfelt thanks to the members of my group, Kelly Lintecum, Greg Wells, Rachel Ganger, Andres Mora, and Sean Seunghyun Jun for their help and support.

I would also like to acknowledge our collaborators at the Monterey Bay Aquarium and Research Institute for their technical guidance and assistance. This work would not have been possible with the financial support from the Gordon and Betty Moore Foundation who funded this project through Grant Number 2728.

In addition, a special thanks to my wife, Sandhita Saha Ray for her support and patience during this effort. And finally, I am forever thankful to my parents and brother for their love, affection and support that I have enjoyed all my life.

TABLE OF CONTENTS

Page

CHAPTER Page

CHAPTER Page

CHAPTER Page

LIST OF TABLES

LIST OF FIGURES

Figure Page

Figure Page

Figure Page

Figure Page

CHAPTER 1

OVERVIEW

1.1 INTRODUCTION

Real time monitoring and characterization of the dynamic biogeochemical properties of the marine environment in large temporal and spatial scales are essential in the design and development of early warning systems and containment strategies. In most situations, biogeochemical variability in the environment takes place over long time-periods. Consequently, in order to properly evaluate the state of environmental conditions, and to plan remediation strategies; accurate, exhaustive, long-term and continuous acquisition of the target data is critical [1].

1.2 IMPORTANCE OF MARINE MEASUREMENT

Oceans cover almost 72% of the earth's surface thereby providing the largest environment for life on earth. But, besides being home to hundreds of thousands of species, it also impacts life on the entire planet as a whole by influencing climate and weather patterns. Also, it is an important source of food for humans all around the world with seafood accounting for around 15% of the average animal protein consumed by most of the population [2]. The world's oceans also play an important role in various other ways, *viz*. extraction of raw materials, waste disposal and transport, which has a profound impact on humans. As such, monitoring of the world's oceans is of great importance not only for the direct benefit of human health, but for exploration and scientific interest in habitat protection and biodiversity. Kröger and Law in their review paper [3] outlines some of the motivations that has driven marine research and monitoring in the recent years. Specifically, the interest in ocean observation stems from the fact that there is still so much that is unknown with regards to the ocean and the part that ocean microbes play in the maintaining the overall climate, food web and

biogeochemical cycling. There is also a great interest in monitoring the presence of harmful microorganisms and their potential impact on humans.

Apart from scientific interest, the other motivator towards understanding and monitoring of marine environments have been legislative initiatives and pollution control, which in part is again driven by food safety and human health. With the increasing focus on marine monitoring, researchers and policy makers have the ability to rapidly detect and formulate mitigation strategies to environmental threats like the occurrence of hypoxic and anoxic areas, toxicants and pollutants, trace metals, eutrophication, ecotoxicology and most importantly harmful algal bloom outbreaks. Harmful algal bloom outbreaks are of particular concern as they can cause mass scale fish kills and could accumulate in filter feeders, which can then get transferred to humans potentially impacting human health [1], [3].

1.3 Issues and Strategies

One of the issues in continuous monitoring of the world's oceans is its vastness. In order to get a proper understanding of the environment it is essential to analyze the collected data in the appropriate temporal and spatial scale. The United States Geological Survey (USGS) in 1972 began a pilot program for the collection of hydrologic data via satellite telemetry to tackle the problem associated with large-scale data collections. Based on the success and utility of satellite monitoring, in subsequent years, a series of Landsat satellites have been operated by the USGS to monitor the biological, chemical and physical characteristics of coastal waters [1]. However, although satellite techniques are great in continuously monitoring a large area, they are still inadequate in providing information that requires sampling and analyzing marine biota and deep-sea conditions.

Until recently, a lot of the information collected from marine environments have been limited to conductivity, and temperature with respect to depth, popularly knows as

CTD sensors. However, recently there has been a great interest in studying a broader spectrum of chemical and biological variables in relation to marine microorganisms. In order to properly characterize the marine ecosystem, there is a need to understand the distribution of microorganisms and their interaction with each other, their specific functions and how their activities relate to the ocean biogeochemical cycle. These methods can also provide a measure of the abundance of different species under specific environmental conditions and their taxonomic and functional gene marker expression by comparing their differences in nucleic acid composition and sequence [4]. Molecular probe assays also offers high throughput, highly specific and sensitive detection and quantification of a range of different organisms in a repeatable manner. Zehr *et. al.* reports on the proliferation of the use of molecular biological methods for the study of marine organisms and provides a comprehensive review of the various approaches that can be implemented on a sensing platform for rapid *in-situ* environmental analysis [5].

But the use of molecular analysis techniques for environmental analysis has traditionally required the return of the samples to a traditional laboratory. Consequently, for analyzing marine samples, the approach has been to collect the water samples in bulk using ships and then either analyzing them on shipboard laboratories or transporting to laboratories on shore. This is a really labor and time intensive process, not to mention the high costs of sample collection, conditioning and transport. Even though these periodic efforts do provide a lot of information on the analytes of interest, they are inadequate on the temporal and spatial scales to formulate a response plan to transient fluctuations in the environment. Furthermore, the samples collected in the field have to be specially treated so as to preserve the snapshot of the conditions during the collection. The preserved samples are then analyzed in a laboratory sometimes days, or even months later, potentially introducing artifacts in the outcomes of those analyses.

Cultivation of marine microbes in the laboratory is also not trivial as their genetic expressions are not a true representation of their expression levels in their natural environment. Additionally, most of the ocean microorganisms are yet to be successfully cultivated in a lab [5].

In order to alleviate these problems a lot of effort in recent years has been directed towards the design and development of portable and/or reusable instrument platforms [6]–[9]. In order to collect appropriate spatial and temporal data, remotely operated vehicles and submersibles have also been employed. But in most cases these types of mobile platforms do not have the capability to perform *in-situ* biogeochemical analyses. *In-situ* instruments with the capability of providing time scale data on moorings, drifters and bottom landers have also been employed; however they are not ideally suited for data collection over large-scale areas [3]. Most of these types of systems necessitate trained personnel and laboratory infrastructure to perform the entire sampling and data analyses process steps. A true vision of an ocean monitoring system would thus be a platform that can achieve not only adequate temporal and spatial resolution of the collected data, but have the capability of performing *in-situ* data analysis and have the intelligence to alert to possible harmful environmental variations in real-time, so that they can be addressed promptly and effectively.

CHAPTER 2

BACKGROUND

2.1 INTRODUCTION

The advances in molecular analysis techniques have provided us with a plethora of techniques that can be used to analyze any sample from any environment. These techniques however require pristine conditions that can only be afforded by a full-scale laboratory. The challenge is therefore to incorporate these analytical techniques onto a platform that retains its mobility while providing the capability to perform *in-situ* analysis in real-time. This calls for developing means of implementing these laboratory based techniques on a semi or fully autonomous platform that is robust enough to be deployed in the field. Scholin defines these classes of wet chemistry based molecular biology sensors on a field-portable platform from the standpoint of ocean water monitoring and research to be "ecogenomic sensors" [10]. These classes of sensors could be employed for detecting the presence and abundance of ocean microorganisms as well as their expression levels and metabolites in their natural environment [11].

2.2 ENVIRONMENTAL SAMPLE PROCESSOR PLATFORM

A platform that has met some of these challenges have been developed by the Monterey Bay Aquarium and Research Institute (MBARI) in the form of a patented device called the Environmental Sample Processor (ESP) [12], [13]. The primary goal of the ESP is to allow the researchers to perform molecular biology experiments remotely over an extended period of time whilst having the ability to direct the sequence of experiments and collect the data in real time interactively [14], [15]. It is developed as an electromechanical-based fluidic platform. The operating procedure involves sampling discrete volumes of seawater and then concentrating the microorganisms contained in that volume of water using filters. The microorganisms are then lysed using a

combination of thermal and chemical techniques and the DNA and RNA extracted and concentrated using a column-based nucleic acid extraction technique. The sample with the DNA/RNA content is then passed onto the analytical module for molecular biological analysis on-board. The ESP also has the ability of chemically preserving the microorganisms on the filters for whole cell archival for later validation and/or more intensive laboratory based procedures [16].

2.2.1 1G ESP Platform

The first generation of the ESP (1G ESP) was first deployed in 2001 and has been used until 2006 to carry out various oceanographic analyses both in the field and on the bench-top to fine-tune the system. In field deployments the 1G ESP was deployed in the ocean for durations up to 20 days. It was instrumental in validating the design concepts of this platform and went on to show its utility. In terms of analytical capabilities, the first generation ESP incorporated a CTD sensor along with prototype DNA probe arrays for harmful algal bloom detection [17], [18].

2.2.2 2G ESP Platform

Based on the results and building on the success of the first generation instrument, the second generation ESP (2G ESP) platform was developed which started its field trials in 2006. The 2G ESP platform developed by MBARI, was designed to be modular in nature, with three major distinct components, *viz.* external sampling module, analytical modules and the core ESP [19]. The external sampling module is designed as a shell for applications to enhance the flexibility of the ESP platform. Specialized versions of this module could potentially be used for different ocean depths or for other environments, like in a water or sewage treatment plant. Different modules could also be designed for varying sampling volume needs. Similarly, with a uniform interface specification, a variety of different analytical modules could be developed for various biological

techniques as and when required. They could be easily optimized for *in-situ* operation as long as they involve processing nucleic acids as provided by the upstream core ESP. Some examples of potential applications could be qPCR modules, microarray modules, trace metal sensors *etc*. The modular core of the 2G ESP is the heart of the instrument. It consists of syringe pumps and an array of valves for sampling water, archiving mechanism, DNA probe arrays and Enzyme-linked Immunosorbent Assays (ELISAs). Additionally, it also houses the fluidic components, power, interfaces for the analytical modules and specialized sampling modules and all the control electronics [16]. This modular nature opens up a myriad of opportunities and provides an incentive to the researchers to develop just the *in-situ* analytical module without worrying about the complexities of sample extraction in different environments. One such application is reported by Preston *et. al.* where a microfluidic block (MFB) (the analytical module) was integrated with the core ESP, thereby enabling *in-situ* two channel PCR on the platform autonomously for a month [20] as elaborated in the next section.

2.2.3 Existing MFB PCR Module

The add-on analytical module on the 2G ESP was custom developed for MBARI by the Lawrence Livermore National Laboratory (LLNL). It is based on the instrumentation developed by Belgrader *et. al.* [21]. It is a flow-through device which incorporates an automated fluid protocol that routes the fluid from inlet to waste through the on-board processes of mixing, thermal cycling and detection to achieve real-time PCR amplification and detection. However, there are a number of limitations to this approach. Firstly, an oscillating thermal cycler was used, that needed alternating heating and cooling of the heating block, which was an inefficient approach given the constraints of a mobile, portable platform. Secondly, their approach utilizes air to separate the reagents; this led to absorption of the reagent molecules to the sidewalls of the tubing.

This in turn to the potential for cross-contamination, which is why the entire fluidic path in between runs needed to be cleaned with 20% bleach [20]. Thus, it was possible to perform experiments only serially, thereby reducing the throughput. The bleach needed to clean the lines increased the volume of liquid that needed to be carried as well. The use of air also had the potential for metering errors due to variations caused by fluidic capacitance in the flexible Teflon tubing.

2.3 Motivation for Current Work

Although the 2G ESP is a great platform for analyzing and recording time series data of the ocean conditions it however still needed to be taken out to sea on board a ship. Normally it is moored at a fixed location to gather time-series data at a single location or set up to drift with the ocean currents to gather spatial and temporal data [22]. However, the later approach still requires close monitoring of the instrument from a nearby ship. Additionally, it limits the deployment of the ESP to potential sites of interest within a short period of time.

Leveraging on the success and experience with the 2G ESP in conjunction with the MFB block from LLNL, MBARI was looking to expand the ESP platform onto mobile platforms. They already have developed a new class of long range autonomous underwater vehicle (LRAUV) that is capable of month long missions in the open ocean within the upper 200 meters of the water column. The LRAUV also has the flexibility to perform as a drifter and vertical profiler without any active propulsion thereby greatly enhancing its range and endurance. Additionally, because of this capability, higher wattage sensor platforms can be integrated as payloads by operating them intermittently according to need [23].

Incorporating the ESP platform onto this mobile vehicle requires a significant redesign of both the front-end sampler as well as the back-end analytical module. This

work is part of the collaborative effort between MBARI and ASU towards the design and development of the third generation ESP (3G ESP) platform. The primary aim of this project was the development of the 3G ESP along with the analytical module and its integration with the LRAUV to enable real-time high throughput studies of the ocean microbial community and their role in the biogeochemical cycling.

Although the LRUV is equipped with a satellite link for real-time communication with on-shore facilities, the goal of this endeavor is for the 3G ESP to operate underwater for most of the time. Consequently, the analytical module needs to be capable of high-throughput biological analyses autonomously for extended periods of time. Furthermore, the analytical module should be able to fit within the size and power constraints of the LRAUV to be really effective for long-term autonomous operation in the open seas.

In a real world scenario, the operation of the 3G ESP on board the LRAUV is envisioned as follows. The LRAUV, equipped with some preliminary sensors *viz*. CTD sensors, chlorophyll concentration sensors *etc*., would be performing the determination of where to perform further analyses; or be directed via satellite link to target a specific location for analysis in response to specific events. Once the LRAUV determines the location for further analyses, it would signal the 3G ESP to initiate collection of seawater. The front end of the 3G ESP would be tasked with the sample collection and then to perform the extraction of nucleic acids from the lysate obtained from the organisms that are present in the sampled seawater [20]. The extracted nucleic acids after being purified and concentrated would then be delivered to the analytical module for analysis. A fraction of the sample would also be stored in the core ESP block for archival so that more exhaustive analyses can be performed later on certain samples if required.

The overall motivation for this work was thus the realization of an analytical module that can be used with the 3G ESP to offer a highly versatile mobile platform with

a significantly enhanced analytical capacity and throughput than is currently possible with the 2G ESP.

2.3.1 Requirements for the Analytical Module

The LRAUV platform, because of its long ranges, endurance and the ability to support an array of different payloads is an exciting platform for many different types of oceanic sensors. Quite understandably, the vision of MBARI thus is to make use of this platform for a multitude of distinct analytical modules performing various biogeochemical analyses. The idea therefore was to have modular components so that the ESP core, as the host, can be easily coupled with a variety of backend analytical modules. The ESP platform would thus perform the seawater sampling and pass on the nucleic acid samples to one or more analytical modules for analysis. Additionally, the ESP would be in the control of the power, data and communication with each of the modules. A schematic of this scheme is illustrated in Figure 2.1.

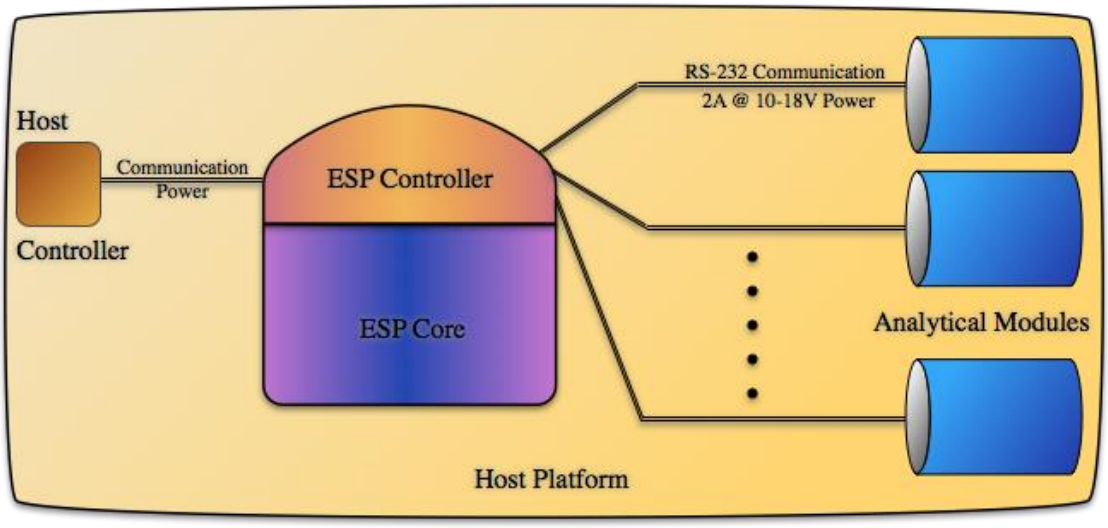

Figure 2.1: ESP Overall Architecture

The analytical modules were thus required to be designed as standalone units with a standard set of interface connections for fluid, power and communication. They should be designed with the flexibility of working with any platform as well that can

provide a sample input and power. Once it receives the sample, it should be able to independently perform its fluidic operations, biological analyses and data storage. Additionally, in order to be compatible with the LRAUV platform, the analytical module needs to be within a certain set of parameters as outlined in this section.

The primary objective of this analytical module is the ability to run up to 50 qPCR samples with each sample being tested against up to 50 different sets of primer and probe combinations. This module also needs to perform reverse transcriptase qPCR (RT-qPCR) for a similar number of samples. The module needs to execute its own internal fluidic functions, *viz.* pumping, valving, routing, reagent storage and waste collection. It needs to have the ability to run autonomously for up to 30 days in a temperature range of 2 ^{o}C to 37 ^{o}C. Because the analytical module would be sharing the space as well as the power with the core ESP module, it places some constraints on the power and volume of the entire module as well to be effective for long autonomous deployments. The analytical module needs to operate on battery power, with a maximum continuous current draw of 2 A at 10-18 Volts with a single electrical interface to the ESP core. It also needs to have a standard fluidic connector to set up the sample delivery path from the core. A RS-232 serial connector is required to be set up as a communication interface with the core as well. The overall dimension of the payload for the 3G ESP onboard the LRAUV is a cylinder 23.5 inches long and 11 inches in diameter. However, the space allocated for the analytical module is only 20% of this volume. The total volume of the instrument thus needs to be less than about 7.5 liters.

CHAPTER 3

OVERVIEW OF POLYMERASE CHAIN REACTION

3.1 INTRODUCTION

One of the most commonly used techniques in the realm of bioanalytical studies is the analysis of nucleic acids. Nucleic acids are essentially biological macromolecules that in the form of Deoxyribonucleic acid (DNA) and Ribonucleic acid (RNA) form the fundamental building blocks of all known life forms. They along with proteins are responsible for encoding and expressing genetic information, and transmitting this information along from one generation to the next using the nucleotide base sequences consisting of Adenine, Thymine, Guanine, Cytosine, and Uracil. The genetic makeup of any organisms, obtained from studying these nucleotide sequences can provide insights into their evolutionary history and taxa, while their gene expression levels can provide insights into their functions. Although the discovery of DNA was performed by Friedrich Miescher in the late 19th century, the study of it was largely limited by the inability to isolate and identify it [24].

However, the development of the PCR process by Kerry Mullis in 1983 [25], for which he was later awarded the Nobel Prize in 1993, enabled greater understanding of nucleic acids. Using this technique, specific sequences can be amplified rapidly and efficiently, which enables easy detection of DNA molecules. This is achieved by amplifying the a few copies of a target DNA molecule to generate up to a billion copies of the specific DNA sequence. In a typical setup, a reaction volume consists of primers, which are short DNA fragments with a sequence complimentary to the target sequence, a heat stable DNA polymerase, deoxynucleotide triphosphates (dNTPs), reaction buffer and magnesium along with the target DNA. This reaction volume is then subjected to alternate heating and cooling cycles, called thermal cycling, for denaturation of the DNA

and primer annealing and extension. In a two-step PCR, the denaturation step takes place for around 15 sec at about 95°C and the annealing and extension at about 60°C (dependent on the primers) for around a minute for every kilo base (kb) of the length of the target DNA molecule. Each of these cycles is called an amplification cycle, and in each cycle the number of DNA copies are ideally doubled over the previous cycle, with typically 20-40 cycles being used for standard analysis. A schematic of the PCR amplification process is shown in Figure 3.1, which illustrates the exponential rate of DNA formation with each cycle, with about a trillion copies of DNA easily obtained from a single DNA fragment. The amplified product is then run through agarose gel electrophoresis to determine the presence and the size of the target DNA.

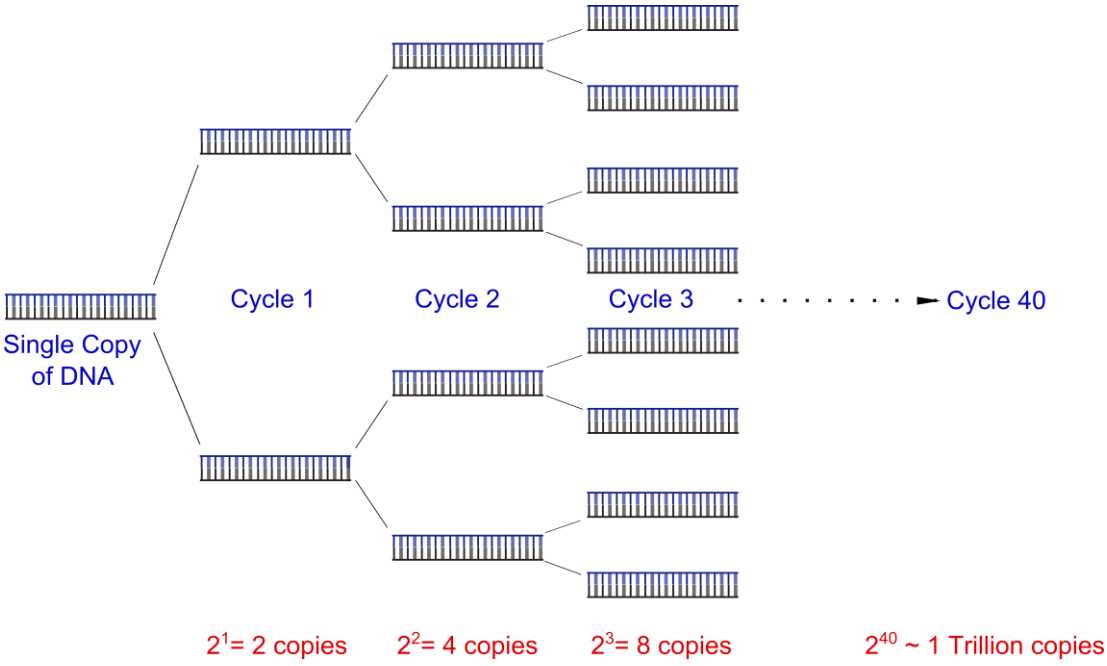

Figure 3.1: PCR Exponential Amplification Pathway

3.2 Quantitative PCR

This process of PCR product though very useful in detecting the presence of target DNA molecules was not really helpful in quantifying the starting concentration of the target DNA molecule. This is because, irrespective of the starting concentration, the end point

detection meant that the product being looked at has more or less the same amount of amplified DNA. The development of the real-time PCR, also known as quantitative PCR (qPCR) by Higuchi *et. al.* in 1992 addressed this issue [26]. This procedure follows the same basic principle as the original PCR procedure. The key difference as implemented by Higuchi *et. al.* was that they implemented a system to monitor amplification of the DNA product from cycle to cycle. This is achieved by using fluorophores that bind with the double stranded DNA, which increase in fluorescence intensity as more of the DNA product is formed.

There are two common methods of this binding mechanism that is currently employed, 1) non-specific fluorescent binding by intercalating with any double stranded DNA, and 2) specific binding by fluorescent reporters probes that interact only with the specific probe sequence in the DNA. One of the most common implementation of the latter mechanism is the Taq-man PCR as is illustrated in Figure 3.2. In this case, a fluorophore is attached at the 5´ end of the probe along with a quencher molecule at the 3´ end. Due to close proximity, the quencher molecule quenches the fluorescence emission by the fluorophore under excitation via Fluorescence resonance energy transfer (FRET), thereby resulting in no net fluorescence of the probe. As the Taq polymerase extends the primer along the DNA, its exonuclease activity results in the release of the fluorophore from the probe, which now can fluoresce without the quenching activity due to the increase in separation. The detected increase in fluorescence intensity in qPCR thus is directly proportional to the amount of DNA product in each cycle.

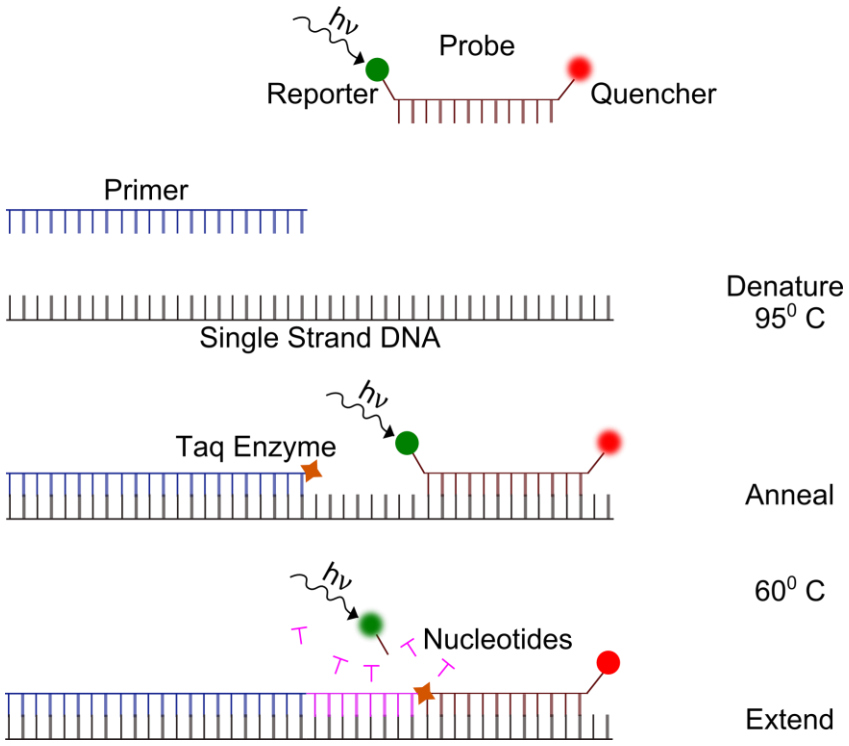

Figure 3.2: The Real-time PCR Process

As the DNA product amplifies, the fluorescence signal level increases exponentially until it reaches a plateau. A threshold is defined in terms of fluorescence intensity and the number of amplification cycles required for the sample to reach this intensity value, called the C_t value. Based on different starting concentrations, the number of cycle required to reach this value would be different, with higher concentrations reaching this level quicker, as a sample containing higher molecules requires less number of amplification cycles to attain the threshold intensity level. The difference in C_t values can provide us a relative estimate of the starting concentrations, and in the presence of a standard, can provide an absolute quantification of the starting sample concentration as illustrated in Figure 3.3. The threshold values are set somewhat arbitrarily by taking into consideration the background fluorescence levels and other instrument specific parameters like excitation intensity and detector sensitivity. Consequently, C_t values should not be compared between multiple instruments.

Assuming 100% efficiency, which translates to doubling of the DNA content in each run, the C_t value is related to the starting concentration according to Equation 3.1

$$\frac{[C_0]_A}{[C_0]_B} = 2^{(C_{tB} - C_{tA})} \qquad \text{Eqn. 3.1}$$

where, $[C_o]_A$ and $[C_o]_B$ are the initial copy numbers and C_{tA} and C_{tB} are the corresponding C_t values for the samples A and B respectively. Relative concentration difference between two samples can thus be readily determined from the above equation. For absolute quantification though, one of the initial sample copy numbers need to be known.

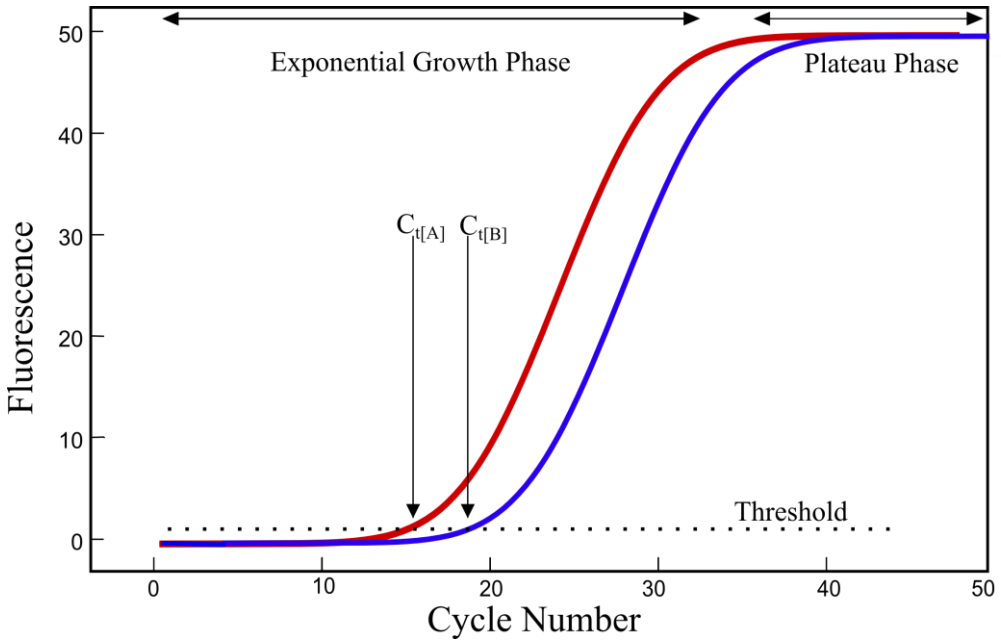

Figure 3.3: Real-time PCR Curves

However, in case of biological samples, typically an efficiency of 100% is rarely obtained due to various factors, like presence of inhibitors, sub-optimal primer probe design, temperature profile variations, inaccuracies in pipetting *etc*. To obtain the correct copy number concentrations, Equation 3.1 is generally modified to account for the efficiency as shown in Equation 3.2

$$\frac{[C_0]_A}{[C_0]_B} = (1+E)^{(C_{tB} - C_{tA})} \qquad \text{Eqn. 3.2}$$

where E is the PCR efficiency. Normally the PCR efficiency ranges from 90% (E = 0.9) to 110% (E = 1.1). Calculation of the efficiency and taking it into account to determine the initial template concentration is essential to get an accurate estimation.

In general, efficiency is calculated using the standard curve based serial dilution method using the slope of the C_t values from each dilution as outlined by Rutledge and Cote [27]. A dilution series is generated for the target template and the C_t calculated for at least 5 different dilutions. The C_t values are then plotted against the logarithm of the sample concentration (Figure 3.4). The data obtained is fitted using the following equation, where m is the slope of the fitted curve

$$C_t = m * log(C_0) + C_t[1] \qquad \text{Eqn. 3.3}$$

The PCR efficiency is then calculated using the following formula

$$E = 10^{-\frac{1}{m}} - 1 \qquad \text{Eqn. 3.4}$$

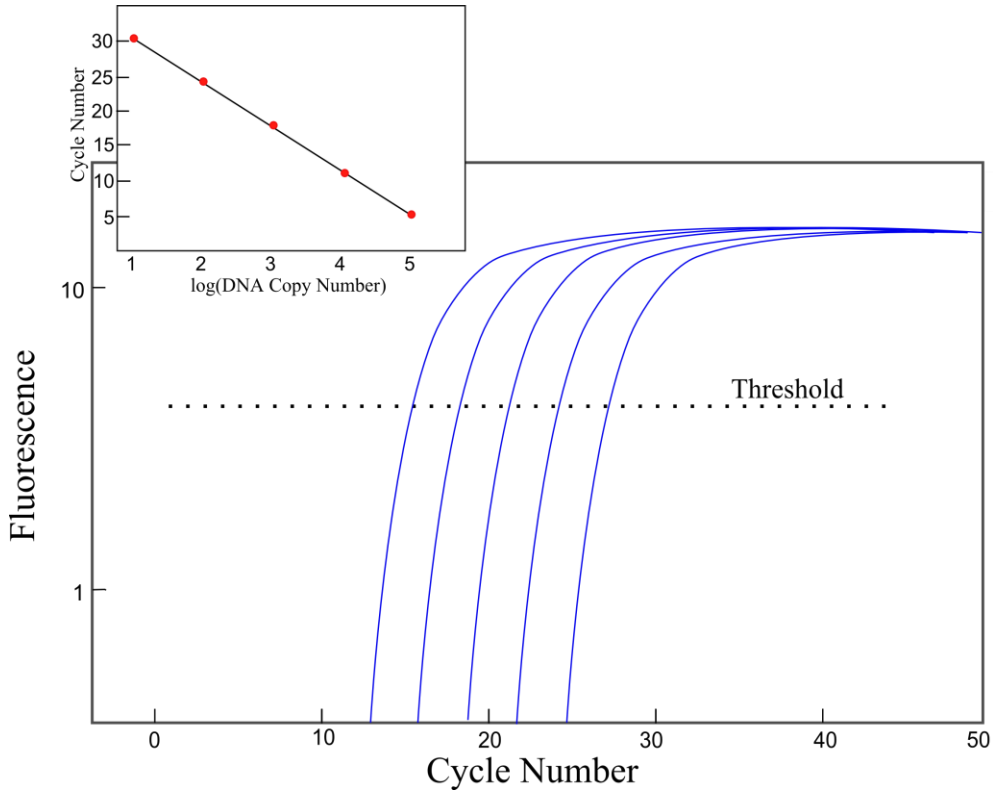

Figure 3.4: Real-Time PCR Standard Dilution Series Curve

Using this method, for an efficiency of 100% (E = 1.0) the slope comes out to be 3.3, which translates to difference in C_t of 3.3 for every 2 fold change in the starting template concentration. In addition, to determine the goodness of the fit to Equation 3.3, the coefficient of determination, denoted by R^2, is calculated as well. A value of R^2 close to 1 is indicative that that the data is a good fit to the equation. The efficiency in conjunction with the R^2 value is then used to qualify the PCR experiment.

3.3 EMULSION PCR

An emulsion is a mixture of two or more immiscible fluids in which one is dispersed in the other. The term emulsion is derived from the Latin word for "to milk" (as milk is an emulsion of fat in water). They are a subgroup of the general class of two-phase systems known as colloids in which both the continuous and dispersed phases are liquids. Normally, emulsion formed simply by mixing two immiscible phases together degrades over time due to coalescence and/or Ostwald ripening, because of the emulsion being in a metastable state. Furthermore, the droplets formed this way have a large variation in size and volume, represented by the standard deviation of the droplet diameters as a function of the mean droplet diameter, in the droplet sizes [28]–[30].

The use of emulsions in biological studies have been used since the 1950s, when Lederberg used water-in-oil emulsions to compartmentalize single bacteria inside emulsion droplets [31]. They are really attractive in isolating and compartmentalizing reagents of interest to study whole cells as well as different biological molecules and consequently they are getting used for the next-generation sequencing platforms. They are reported to have a higher sensitivity and amplification efficiency because of the compartmentalization of templates and the primer probes [32]. For an effective emulsion PCR system, the droplet sizes are expected to be in the range of 20 μm – 30 μm

and have a single template of the DNA molecule in each droplet. So essentially, millions of templates thus can be amplified individually in a single experiment [33].

However, the early schemes for emulsion generation had an inherent drawback, due to the non-uniformity of the emulsion droplets formed. This non-uniformity in the droplet volume introduced variations in the reaction conditions thereby making it difficult to compare droplet based analysis assays. The microfluidic platform to generate emulsion microdroplets however can provide tighter control on the variability of their volumes. A lot of studies thus have focused on the formation of mono-dispersed microdroplets as is reviewed by Theberge *et. al.* [34].

3.4 DIGITAL PCR

Digital PCR, also known as dig-PCR or dPCR, is a variation of the quantitative PCR process for the detection and quantification of nucleic acids first reported by Vogelstein and Kinzler in 1999. The exponential nature of the qPCR signal and the need for reference standards or endogenous controls are simplified in the dPCR technique by providing a linearized digital signal for quantification. In case of dPCR, the template is diluted to such an extent such that single molecule isolation can be achieved which are then amplified individually as a traditional PCR reaction [35]. This extensive dilution distributes the individual DNA templates into isolated compartments. The dilution of the sample to contain single template in compartmentalized volumes reduces the intensive data analysis required for estimating starting concentration in case of qPCR. The analysis thus involves counting the number of positive and negative droplets and fitting them to a Poisson statistical algorithm.

As illustrated in Figure 3.5 the bulk sample is partitioned into many partitions after diluting it so that ideally only one template is present in a only a fraction of the droplets that has any template in it. After that PCR amplification is performed on the

entire droplet partitions and then the number of partitions in which a reaction occurs is counted as positives. The number of positives is then considered to estimate the number of template molecules, which provides an absolute measure of the starting concentration. However, the ideal scenario of getting only one template in each partition is not feasible and one is more likely to get more than one templates in some of the droplets, thus introducing an error in the estimation of the starting concentration.

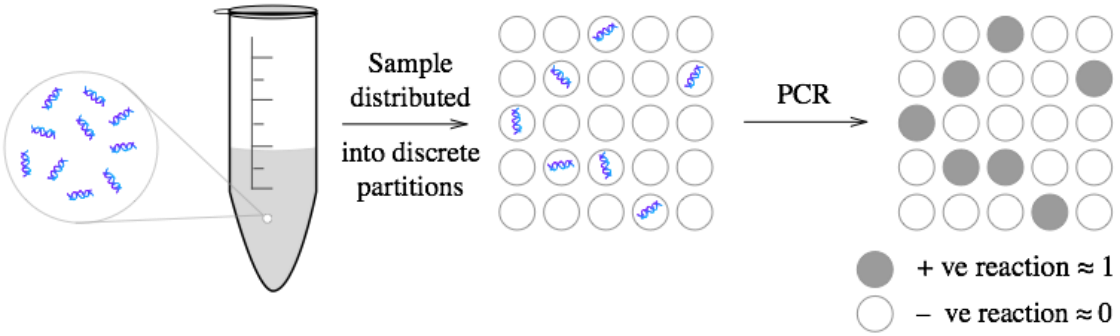

Figure 3.5: Schematic of the Digital PCR Process

Poisson distribution deals with the random distribution of independent events using which estimation can be made about the number of droplets containing 1, 2 or more templates molecules in each positive droplet. In a dPCR experiment, if the fraction of droplets with a positive reaction is counted to be p, then the Poisson distribution can be applied to obtain the correct number of copies per reaction chamber using Equation 3.5 as reported by Dube *et. al.* [36].

$$\lambda = -\ln(1-p) \qquad \text{Eqn.3.5}$$

All these assumptions in the determination of the initial concentration are dependent greatly on the individual sample volumes. Sample partitioning thus is a critical aspect of the dPCR. To that end, microfluidic techniques have the potential to achieve uniform and repeatable sample partitioning. Furthermore, droplet microfluidics can be used for the uniform generation of nano- to femtoliter sized droplet emulsions, which is ideally suited for digital PCR. This method of uniform droplet emulsions

generated using microfluidics providing controlled PCR volumes, known as droplet digital PCR (ddPCR), can thus be used with the analytical methods above.

Digital PCR provides a number of advantages over traditional PCR and qPCR. It does not rely on standards and controls for the quantification of the target concentration, instead providing an absolute measure without the need for internal calibration. Although qPCR can potentially provide a higher dynamic range, using proper dilution schemes, dPCR can also be used over large dynamic ranges as well. Furthermore, the dPCR technique is highly tolerant to the presence of inhibitors. This is because, in case of dPCR, the detection is performed at the very end, so the shift in C_t cycles because of inhibitors, that skew qPCR results, do not have an effect. The linear nature of the dPCR response also allows higher resolution of small differences in template concentration compared to other PCR techniques. Use of dPCR techniques is also been used extensively for the detection of rare mutations and copy number variations because of the accuracy and precision that can be achieved with this technique. Thus digital PCR builds on many of the limitations of qPCR and is quickly emerging as a technique in the ever-expanding toolbox of the molecular analysis techniques.

CHAPTER 4

MICROFLUIDICS FOR BIOLOGICAL ANALYSES

4.1 INTRODUCTION

Microfluidic technology has come a long way since it was first presented in the early 1950s for dispensing nano- and picoliter range liquids, which forms the basis of the ink-jet printer technology. Microfluidics is an engineering science dealing with the manipulation and control of minute amounts of fluids on the order of microliters or less using micro-channels that are on the order of tens to hundreds of micrometers. Since the 1990s microfluidics has grown rapidly as a technique based on its potential to revolutionize established analytical tools and techniques. Microfluidic devices has since gained widespread popularity owing to its obvious advantages in reducing sample volumes and reaction times at a fraction of the time and cost compared to traditional bench-top tools. Consequently, currently it is one of the top emerging technologies in the field of chemical and biological analyses [37]–[40]. Microfluidics as a technology can be applied in almost every aspect of scientific research spanning a wide range of application areas. There have been numerous reviews that have been written highlighting the proliferation of microfluidics in the fields of biological and chemical analysis [41]–[43], point of care diagnostics [44], micro-scale polymerase chain reaction (PCR) [45]–[47], forensic analysis [48], agri-food industries [49] *etc.*

4.2 MICROFLUIDICS FOR BIO-ANALYTICAL ANALYSES

Currently, there is tremendous research effort in the analysis of sub-cellular components and protein engineering. Microfluidic devices, with their characteristic lengths in the range of sub-cellular length scales, compatibility with aqueous analysis environments and fluid handling on the scale of cellular volumes are perfectly suited for this field. Another obvious advantage is reduction in the amount of expensive reagents required

due to reduction in assay volume used in the micro-channels. Additionally, microfluidics opens up the possibility of massively parallel processing enabling high throughput analysis of hundreds or more samples in a relatively short period of time. This technology provides the researcher with the means of studying cell behaviors in a population in the presence of precisely applied localized stimuli [50], [51]. Consequently, use of microfluidic components in this field is almost ubiquitous.

4.2.1 Advantages of Microfluidics

Various physical phenomena that previously placed a limitation on the time scale and sensitivity of bio-analytical analyses can be mitigated by simply reducing characteristic dimensions of the devices as is achieved in case of microfluidic devices. Although the laws of physics for these microscopic systems are similar to their macroscopic counterparts, the reduction in the scale gives rise to a different set of forces that in some cases dominate at these scales. The ratio of surface area to volume in fluidic systems, scales inversely with the characteristic length, which leads to rapid heat and mass exchange in case of microfluidic systems compared to the corresponding macroscopic components. Rapid heating and cooling as well as separation are much more efficient in the microfluidics domain as a result. Diffusion times, which scales to the characteristic length in the second order can easily be reduced many fold simply through miniaturization [39]. The increase in the surface area compared to the volume also leads to a dominance of various surface phenomena over volume phenomena. This enables passive liquid actuation techniques taking advantage of capillary forces by tuning the surface properties of the microfluidic devices. With the device sizes in the microns range frictional forces become increasingly relevant compared to inertial forces, thereby giving rise to fluid flow in the laminar flow regime. The laminar flow regime is characterized by smooth and constant fluid flow in which the fluid tends to flow in parallel layers with

minimal mixing between the layers. This opens up the possibilities of creating stable and precise liquid-liquid interfaces with a varying concentration gradient inside a single channel [37], [51].

4.2.2 Microfluidics and the Lab-on-a-chip concept

In case of microfluidic devices, because of the minute volumes of liquid involved, interfacing with macro devices and even in between discrete microfluidic devices becomes a challenge. This has given rise to the need of an integrated microfluidic platform approach. The concept of integrated microfluidic devices was first introduced by Manz *et. al.* [52] in the early 1990s and since then this concept has become the mainstay of various biological and chemical analysis processes. The entire process of sample handling through reaction, separation and detection performed previously using traditional bench-top protocols and instruments can be easily integrated onto a single chip quite easily. Integration on a single chip eliminates the possibilities of reagent loss and cross-contamination while enabling automation and parallelization. Integrated microfluidic devices have the ability to incorporate the essential components and functionality of an entire room-sized laboratory onto a single chip [37], [39], [53].

4.3 BASIC PRINCIPLES OF MICROFLUIDICS

Fluid behavior at the microscale is markedly different from that observed in the macroscale. Phenomenon like gravity and inertia, which are important in the realm of microfluidics are generally negligible in the case of microfluidics. Furthermore, in case of microfluidics, the effects of the boundaries of the devices have a significant bearing on its properties as the characteristic geometries generally have large surface-area-to-volume ratios, necessitating the study of fluid-structure interactions.

There are a wide variety of phenomena occurring in the microscale that distinguishes it from the fluid interactions in the macro scale. Viscous forces rather than

inertial forces primarily dominate mass transport in the microscale, a measure of which is provided by the Reynolds number (*Re*). It is a dimensionless number that quantifies the relative importance of the inertial and viscous forces for comparable flow conditions. It is defined as follows:

$$Re = \frac{inertial forces}{viscous forces} = \frac{\rho U_0 L}{\mu} = \frac{U_0 L}{\nu} \qquad \text{Eqn. 4.1}$$

where ρ is the fluid density, U_o is the mean velocity, L is the characteristic length of the system, μ is the dynamic viscosity and υ is the kinematic viscosity of the fluid. For microfluidic systems, with velocities in the range of 1 μm/s to 1 cm/s, channel radii of 1 – 100 μm, and with water as the sample fluid, the Reynolds number is calculated to be in the range of 10^{-6} to 10 from the above equation. It thus shows that in case of microfluidics the viscous forces overwhelm inertial forces. In this regime of low *Re* flow, the flow is completely laminar as it is characterized by smooth, constant fluid motion. With increasing *Re* numbers, the inertial forces start to dominate resulting in chaotic, turbulent flows in the range of *Re* = 2000. Fluid flows in microfluidic devices typically are characterized by *Re* < 100, thereby well within the laminar flow regime.

The laminar flow regime, typical of microfluidic systems, is defined as the flow of fluids, in which layers of fluid move in parallel with minimal interaction between neighboring layers that prevent miscible liquids from mixing rapidly. At the velocity scale of microfluidic systems, the fluids thus flow without much of lateral mixing. Mixing is thus limited to diffusion alone, which is inherently a much slower process. This is great for applications requiring transport of different reagents through the same channel simultaneously. Depending on the specific application of the microfluidic devices, both rapid mixing and separation of fluid streams are necessary either in separate devices of even in the same device. Consequently, the control of the dispersion of multiple fluids in microfluidics is of great importance. A measure of the relative importance of the

convective phenomenon with respect to the diffusive phenomenon is given by the Péclet number (*Pe*). It is a dimensionless number defined as the ratio of the convective transport rate to the diffusive transport rate.

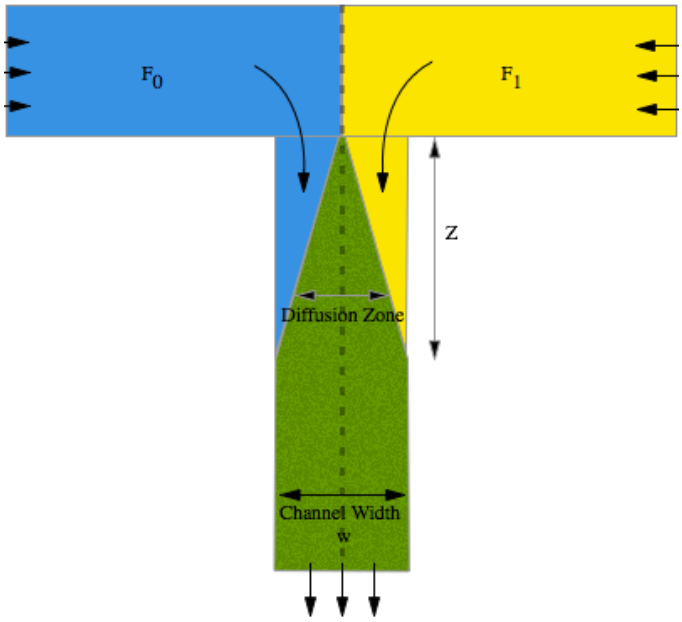

Figure 4.1: Diffusion of Two Fluids while Merging at a T-junction

In case of two fluid streams F_0 and F_1, as illustrated in Figure 4.1, when they merge at the same rate, a separation is formed initially because of the laminar flow regime. Over time however, the diffusion phenomenon will lead to dispersion of one phase into the other. The diffusion region grows gradually and after time $t \sim w^2/D$, the mixing zone is the same as the channel width, w, where D is the diffusion constant. The fluid in the meantime has moved a distance of $Z = U_0 t = U_0 w^2/D$. Thus, the number of channel widths necessary for the diffusion process to be complete can be estimated as

$$\frac{Z}{w} \approx \frac{U_0 w}{D} = Pe \qquad \text{Eqn. 4.2}$$

which also gives a measure of the relative importance of convection to diffusion, which is also the Péclet number.

Now, the ability of certain fluids to mix is given by the Schmidt number (S_c), which is defined by the ratio of the Péclet number to the Reynolds number. In terms of physical parameters it is thus the ratio of shear diffusivity (υ) to the diffusivity for mass transfer (D).

$$Sc = \frac{kinematic\ viscosity}{molecular\ diffusivity} = \frac{Pe}{Re} = \frac{\mu}{\rho D} = \frac{\nu}{D} \qquad \text{Eqn. 4.3}$$

A higher S_c number consequently indicates a lower propensity for diffusive mixing and vice versa. It is a factor that depends only on the properties of the liquid.

In case of immiscible fluids, another effect that needs to be looked into is the surface tension (γ) that affects the free surface dynamics. It is the energy required to increase the liquid surface area by a unit area. It results from an imbalance of the cohesive forces between liquid molecules. A number of effects, *viz*. beading, dripping, capillary action, emulsion formation *etc*. can be attributed to this phenomenon. Viscous forces, which dominate in the microscale are related to the surface tension by the dimensionless Capillary Number (Ca) and is given by Equation 4.4

$$Ca = \frac{\nu U_0}{\gamma} \qquad \text{Eqn. 4.4}$$

The surface tension between liquid-liquid and solid-solid interfaces can be manipulated to facilitate interesting applications in microfluidics. Capillary forces, resulting from the interaction of solid, liquid and gas surfaces at their interface due to surface tension, can be utilized for the manipulation and transport of fluids. Surface tension at liquid-solid interfaces can be modified making the surfaces either hydrophobic or hydrophilic. Using this property "wall-less" channels [54]–[56] and pressure-sensitive gates [56], [57] have been developed. In the former case patterned hydrophobic or hydrophilic surfaces form the channel walls that confine fluids of the opposite kind in streamlined structures, while

in the later case, application of pressure beyond the threshold of the capillary force can force fluids beyond a hydrophobic or hydrophilic barrier.

4.4 The Special Case of Microfluidic Droplets

In case of two immiscible fluids the surface arising at their interface is also known as interfacial tension. It plays an important role in the formation of emulsions where one immiscible fluid is dispersed in another forming droplets. Thorsen *et. al.* reported the formation of well-regulated droplet emulsions by the injection of water (the dispersed phase) into a stream of oil (the continuous phase) at a T-junction [58]. In the absence of any interfacial tension the two streams would flow side-by-side, however because of interfacial tension the overall surface area is minimized so that the free energy of the interface is reduced. Since for a given volume, sphere has the minimum surface area, the dispersed phase takes the shape of a droplet or bubble. Balancing the two competing stresses, the capillary stress (γ/R) and the viscous stress ($\nu U_0/h$) provides an estimate of the size of the droplet [59] as shown in Equation 4.5,

$$R = \frac{\gamma}{\nu U_0} h = \frac{h}{Ca} \qquad \text{Eqn. 4.5}$$

showing a direct relation between the channel height (h) and Capillary number (Ca) with the radius of the droplets (R) formed.

The interfacial tension and the viscosity both tend to dominate at the small scales, with the Capillary number, *Ca*, providing a relationship of their relative strengths. In case of low *Ca* systems, the stresses caused by interfacial tension dominate over viscous stresses, and in order to minimize the surface area over which interfacial tension acts, nearly spherical drops are formed. On the other hand, in case of high *Ca* systems, viscous effects are strong which leads to larger droplets with asymmetric shapes.

The interfacial tension thus plays a strong role in the formation and manipulation of droplets. Enhanced control over droplet creation and transport thus can be achieved if

the interfacial tension can be manipulated. Amphiphilic molecules, called surfactants, having different groups with different affinities for the immiscible phases in an emulsion are commonly used for this purpose. Generally, they lead to a reduction in the surface tension between the two phases, which can be estimated by the number of molecules adsorbed at the surface. Addition of the surfactant also introduces an energy barrier that works to stabilize the droplets in a metastable state. Surfactant molecules are generally made up of long hydrophobic tails and compact polar heads that aggregate at the interface of the immiscible fluids, aligning perpendicularly to the surface. The stabilization achieved using surfactants help in preventing coalescence of droplets in two primary ways. Firstly, the surfactant layer applies an electro-static repulsion force that prevents coalescence. Secondly, they are also responsible for slowing down the hydrodynamic flow at the interface because of Marangoni effects. The variation of the interfacial tension also provides a feedback, which influences the droplet formation and transport [60], [61]. Furthermore, it has been reported by Fuerstman *et. al.* that in the presence of surfactants the velocity of droplets can be reduced by up to 50% [62].

Formation and manipulation of these droplets opens up a whole new spectrum of applications in the area of bioanalytical studies. Studies on them have shown that they can be produced in a controlled and reproducible fashion. Droplet microfluidics also appeal to lab-on-a-chip type of applications as it addresses one of the basic issues of single-phase microfluidic applications; it provides control over dispersion and mixing of analytes by encapsulating them [63]. However, they introduce non-linearity in the linear flow regime because of variations in interfacial tensions, which introduces additional complexities in the analysis of their behavior.

The flow of emulsified dispersions in microchannels can be classified into two distinctive categories: i) transport of emulsions whose diameter is smaller than the size

of the channel, droplets as illustrated in Figure 4.2a; and ii) transport of emulsions that are larger than the channel size and therefore occupy most of the channel cross section, plugs, as illustrated in Figure 4.2b. In case of mono-dispersed droplets as is shown in the figure, they follow the flow velocity of the continuous phase. In case of plug flow as illustrated in Figure 4.2b, the flow is a strong function of capillary effects and the deformability of the droplet interfaces [61]. In the latter case, even though the droplet appears to be grazing the sidewalls, in reality, a thin film of the continuous phase envelops the droplet plug due to viscous entrainment. It has been theoretically and experimentally established that for low Capillary numbers, thin films of the continuous phase in the order of 1% - 5% of the channel half height, separate the droplet plugs from the channel walls [61].

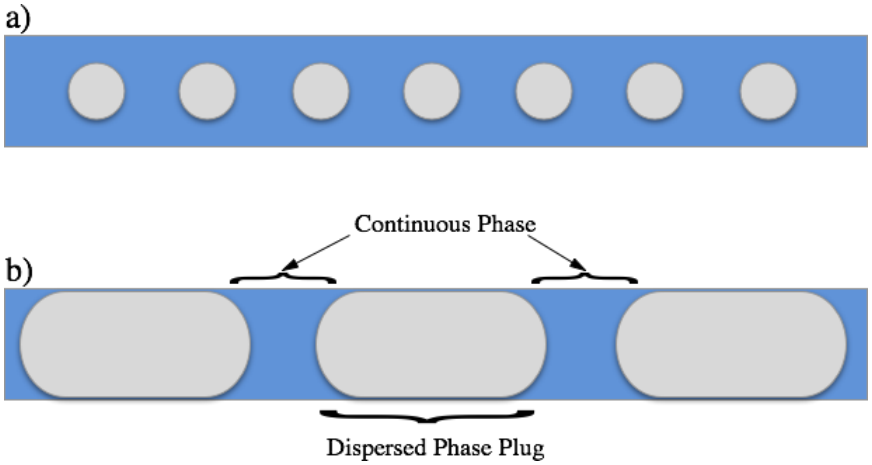

Figure 4.2: Droplet Emulsion in a Channel

In case of droplets, the Laplace pressure at the interface increase resulting in pressures inside the droplet to be larger than that of the outside. The pressure exerted by the droplet thus continuously ousts liquid from the thin film into the bulk. This pressure is in constant competition with the viscous drag of the continuous phase and has a direct bearing on the droplet plug velocity. In case of circular channels, where the droplet plug uniformly occupies most of the channel volume, it has been reported by Schwartz *et. al.* that longer plugs move faster than shorter plugs in the presence of the thin films, and

they showed experimentally that plugs in general move faster than the carrier fluid according to Equation 4.6 [64].

$$\frac{V_{droplet} - V_{carrier}}{V_{droplet}} \propto Ca^{\frac{2}{3}} \qquad \text{Eqn. 4.6}$$

An interesting phenomenon happens when the channels are rectangular in nature. In case of rectangular channels, the droplet plugs cannot completely fill up the channel cross-section and thus the continuous phase can flow past the droplet plugs through the corner gutters. In this scenario, it has been shown both experimentally [62] as well as theoretically [65], [66] that the carrier fluid moves faster than the droplet plugs according to Equation 4.7.

$$\frac{V_{droplet} - V_{carrier}}{V_{droplet}} \propto -Ca^{-\frac{1}{3}} \qquad \text{Eqn. 4.7}$$

In case of single-phase flow, the pressure drop across a certain section of microfluidic channel can be calculated using the Hagen–Poiseuille equation (Equation 4.8). The Hagen–Poiseuille equation assumes the flow to be laminar with a constant flow rate for a viscous and incompressible fluid.

$$\Delta P = \frac{8\mu L Q}{\pi r^4} = R_{hydro} Q \qquad \text{Eqn. 4.8}$$

Where, ΔP is the pressure drop, Q is the volumetric flow rate, L is the characteristic length of the system, and r is the radius of a circular microchannel. For a circular channel, as is illustrated in Equation 4.8, the hydrodynamic resistance of the channel is $R_{hydro} = \frac{8\mu L}{\pi r^4}$. The hydrodynamic resistance of the system relates the flow rate and the pressure drop in any microfluidic channel. For rectangular channels, the hydrodynamic resistance is given by $R_{hydro} = \frac{12\mu L}{wh^3(1-0.630\frac{h}{w})}$.

However, Laplace's law demonstrates that because of surface tension in case of curved interfaces, there is a pressure drop across it. It is estimated by the Young-Laplace

equation, which describes the difference in capillary pressure across the curved interface due to surface tension as illustrated in Equation 4.9, where R_1 and R_2 are the radius of curvature of the two curved surfaces.

$$\Delta P = \gamma(\frac{1}{R_1} + \frac{1}{R_2}) \qquad \text{Eqn. 4.9}$$

Therefore, for two-phase emulsion flows, to measure the pressure drop, the Laplace pressure drops needs to be accounted for. As illustrated in Figure 4.2b, the emulsion system can be considered as a succession of droplet plugs and plugs of the continuous phase. The total pressure drop thus can be calculated as the viscous contribution from the dispersed and continuous phase fluid plugs and the pressure due to the curved interfaces as shown in Equation 4.10.

$$\Delta P_{total} = \Delta P_{cont\ phase} + \Delta P_{disp\ phase} + \Delta P_{curved\ interface} \qquad \text{Eqn. 4.10}$$

Baroud *et. al.* derived the total pressure and has shown that the it is nonlinear, depends on the velocity of the droplet plugs and the velocity of the continuous phase, and increases in discrete steps as the number of droplet plugs increases [61]. The derived equation however involves a number of constants, which makes evaluating the pressure drop for different channels complicated. Additionally, the introduction of surfactants greatly changes the relationships making it difficult to come up with a single relationship for pressure drops in case of droplet emulsion flows.

4.5 Droplet Dynamics

4.5.1 Droplet generation schemes

The most important aspect of droplet microfluidics is the production of the droplets. For biological analyses, it is essential for the droplet volumes to be precise and repeatable and needs to be generated at certain rate. Using the advantage of the deterministic microfluidic flows, monodisperse droplets can be formed using a variety of

techniques. They can primarily be divided into active droplet generation techniques and passive droplet generation techniques.

Active droplet generation using electrohydrodynamic (EHD) techniques are dielectrophoresis (DEP) and electrowetting on dielectric (EWOD). DEP is used to generate uniform droplets by essentially drawing fixed volumes of the fluid from a reservoir. It however, requires that the dielectric permittivity of the droplet fluid be more than that of the surrounding fluid. EWOD on the other hand is based on the fact that using an electric field the interfacial energy between the fluid and the surface can be manipulated to make fluid flow in the desired direction via capillary forces. The droplet size is a function of the electric field intensity, frequency and the channel width. EHD techniques require no external pump and because of the intricate control over the droplet that can be achieved can be used for really complicated fluid routing [67], [68].

In case of passive droplet generation, there are three techniques that have emerged as a means of controlling droplet generation based on the geometry and the flow. They are (i) droplet generation in a co-flowing stream (Figure 4.3a), (ii) droplet generation in a cross-flowing T-junction (Figure 4.3b), and (iii) droplet generation in a flow-focusing configuration (Figure 4.3c). In all the cases, the dispersed phase flows into a microchannel where it encounters the immiscible continuous phase. The geometry of the junction along with the flow rates and the physical properties of the fluids determines the localized flow fields leading to droplet formation due to the shearing of the dispersed phase by the continuous phase.

In case of the co-flowing droplet generation, a cylindrical glass capillary is aligned inside another outer square or rectangular capillary, first reported by Cramer *et. al.* Two distinct droplet generation regimes can be seen in this case, dripping, where droplets are generated right at the tip of the inner capillary, and jetting, where the droplets are

generated from an extended thread off the tip of the inner capillary with the transition taking place over a certain critical velocity of the continuous phase fluid [69].

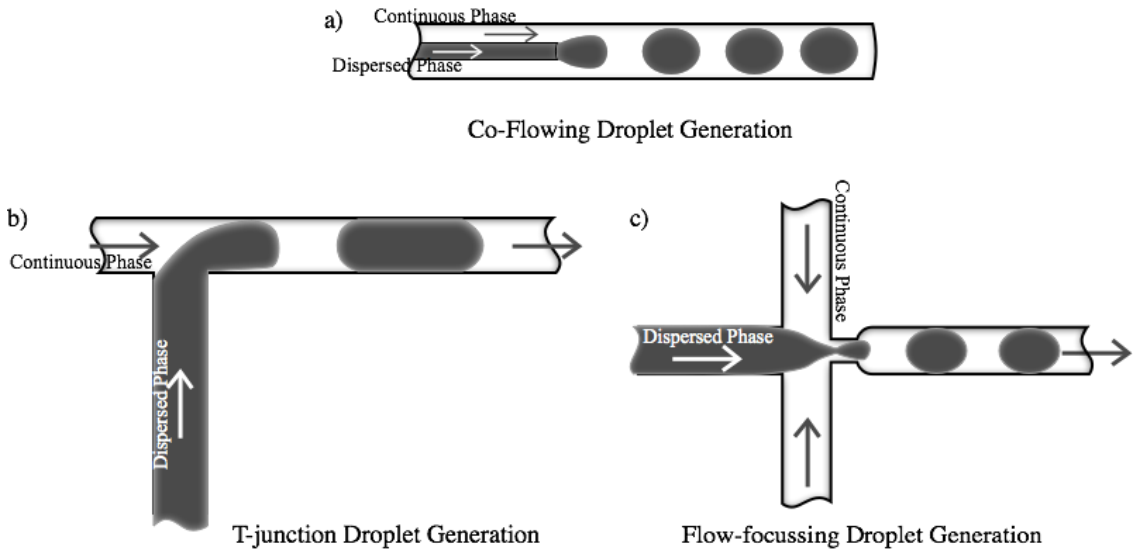

Figure 4.3: Geometry Based Passive Droplet Generation Schemes

In case of T-junction, first reported by Thorsen *et. al.* the dispersed fluid is introduced perpendicularly to the continuous phase [58]. The droplet formation dynamics depend on the geometry channels, the flow rates and the viscosities of the two fluids. Three distinct regimes can be observed in this setup. In the first case, when the width of the dispersed phase channel is much smaller than the width of the continuous phase channel and the capillary number is large enough, droplets are generated before they get the opportunity to block off the cross-channel because of shear stress. Droplets are generated when the viscous stress overcome the interfacial tension between the fluids [61]. In case of the two widths being similar, and a low capillary number, the dispersed phase fills up the cross-channel, constricting the continuous phase. This leads to an increase in pressure leading to necking and pinch off of the droplet plug. Yet another regime is observed when the dispersed phase velocity is greater than the continuous phase flow by a certain critical amount, no droplet generation is observed. Rather the two phases co-flows downstream of the droplet generation junction. The

critical value is a function of the viscosity, with an increase in viscosity of the dispersed phase reducing the critical value.

In case of flow-focusing devices, first proposed by Anna *et. al.* [28] and Dreyfus *et. al.* [70], the dispersed phase is forced through a narrow region with two counter-flowing continuous phase streams with the dispersed phase broken up by the Rayleigh-Plateau instability to form droplets. This scheme of droplet generation provides a greater degree of control over the droplet generation, producing more uniform and stable droplets. As in the other two cases, the channel geometry, flow rates and viscosities all play an important role in the droplet generation speed and size. However, it has been shown by Garstecki *et. al.* that this scheme of droplet formation is largely independent of the Capillary number [71]. This provides a robust generation of droplets, with greater control over the uniformity and frequency.

4.5.2 Mixing inside droplets

Because of laminar nature of the flow, one of the issues of single phase laminar flow in microfluidic systems have been that, it really limited mixing of analytes necessary for certain chemical reactions.

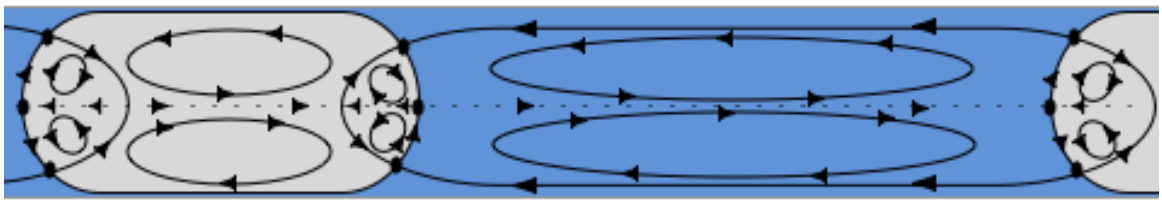

Figure 4.4: Schematic Showing Recirculation in a Droplet Emulsion System

Two-phase flow introduces a tumbling like motion of the droplet plugs that introduce recirculating zones inside them which is a function of the viscosity ratio [72] as is illustrated in Figure 4.4. The droplet mixing is aided by the cross-flow advection. However, as is clear from the figure, the mixing can be inefficient in certain areas as the top and the bottom half of the channel are hydrodynamically isolated. To mitigate this

problem, Song *et. al.* reported a type of microchannel with sharp transitions wherein they could achieve homogeneous mixing inside the droplets in about 10 ms [63], [73]. This scheme along with emulsion droplet microfluidics provided a means of rapid mixing strategy even in the laminar flow regime.

4.5.3 Merging of droplets

In order for any bio analytical experiment to take place, the mixing of different reagents in the proper concentrations is really critical. Consequently, the fusion of droplets in case of droplet microfluidics needs to take place in a repeatable and robust manner with control over the timing. There are two approaches to droplet fusion, passive fusion techniques, which are purely based on geometry which relies on widening and then contracting the channel dimension so that the droplets come close together leading to drainage of the continuous phase fluid between them. Drops have been observed to merge under decompression merging, when they are being pulled apart after coming together [74], or under compressive merging when they merge while they are being pushed into one another [75].

The passive approach works fine in merging droplets in cases where the surfactant concentration, used to stabilize the droplets formed, are minimal or absent altogether. In the presence of higher surfactant concentrations however, this approach fails to yield repeatable results as the surfactant layers in the adjacent droplets interact to retard the merging. This requires the use of active merging techniques either by using an electric field or by localized heating. Electro-fusion is by far the most popular method of fusing droplets in a repeatable manner over a wide range of voltages and frequencies and has been extensively characterized [76]–[79]. Priest *et. al.* theorized that the underlying mechanism involves the destabilization of the interface leading to the formation a liquid bridge and then eventually fusion [80]. Electrodes are patterned underneath the

microchannels on chip and hooked up with a high frequency AC or DC voltage source. Successive droplets can then be merged using either an optical feedback system or by actively trapping the droplet in the electrode region [81].

Another approach to droplet fusion is the localized heating of two adjacent droplets to disrupt the surfactant layer between them. Huebner *et. al.* used a focused laser, that can be fine-tuned, to achieve heating over a precise location of the microchannel to achieve droplet fusion using a trap to bring the droplets together [82].

CHAPTER 5

OVERVIEW OF MICROFABRICATION TECHNIQUES

5.1 INTRODUCTION

As is evident from the previous chapter, the advantages of microfluidics are primarily owing to the effects of miniaturization. And this miniaturization of the components is the primary motivation for microfabricating microfluidic devices. Microfabrication have been around for decades in the semiconductor industry and the processes are already well established. Consequently, these same processes can easily be implemented for the microfabrication of microfluidic devices. This chapter thus provides an overview of the microfabrication techniques that are pertinent to the fabrication of microfluidic devices.

Microfabrication can be described as the set of techniques utilized for the fabrication of structures in the millimeter or smaller range. Historically, the semiconductor manufacturing industry in their bid to shrink the size of the integrated circuits drove the research and the subsequent development of this field. Taking advantage of the established fabrication techniques, various niche areas have been developed over the years through the augmentation and adaptation of those processes for specific applications. Some of the more prominent adaptations of this technique are the development of Micromechanical systems (MEMS), micromachining, microfluidics devices that have opened the way for lab-on-a-chip (LOC) and micro total analysis systems (μTAS).

With the growing interest in high-throughput, automated, fast bioanalytical systems necessitating low regent volume consumptions like drug testing and discovery, single cell analysis, sequencing *etc.* there is a great demand for micro-fabricated microfluidic devices. Microfabrication techniques have been applied to miniaturize not

only standard bench-top biological instrumentation, but have enabled the design and development of novel application specific devices in the field of biology and medicine.

Normally, a device is microfabricated on the substrate material either by an additive process on its surface, also called surface micromachining, or by taking out material from the bulk material, also called bulk micromachining. In most cases however the devices are made using a combination of both these techniques to achieve the desired structures. The basic process steps include, deposition or growth, photolithography or patterning and etching or removal from a base substrate.

5.2 SUBSTRATE MATERIALS

A wide variety of materials *viz*. Silicon, glass, quartz, ceramics, plastics, and metals have been successfully used for microfabrication based on the application. However for applications in biology and medicine, Silicon, glass and plastics generally have been used more than others.

Transitioning from the integrated-circuit fabrication techniques, silicon appeared to be the natural choice because of well-established fabrication processes with the first microfluidic channels being developed in it [83]. Furthermore, it has suitable mechanical properties, excellent chemical properties, and is conducive to the integration of sensing circuitry right on the same substrate producing monolithically integrated microsystems. Although many microfluidic devices have been realized in silicon, they are not quite ideally suited for most biological or medical systems, owing to its lack of optical transparency as most bioanalytical devices call for some sort of optical detection.

Glass substrates can be fabricated using classical microfabrication techniques. Most biological applications where optical transparency, low electrical conductance and most importantly biocompatibility are required, glass have been the substrate of choice. Fused silica in particular can withstand high temperatures, have low autofluorescence,

and are optically transparent down to shorter wavelengths of light. Glass devices can also be bonded to silicon substrates thereby enabling integration of electrical circuitry while still maintaining partial transparency from one side.

Both glass and silicon substrates however are quite expensive and thus are not conducive for disposable devices. Consequently, polymers or plastics have become really popular substrates for microfluidic devices owing to their lower cost, biochemical compatibility, and rapid fabrication. Also, having disposable devices reduces the need for sterilizing and cleaning. Plastic substrates most commonly used are polyimide, poly (methyl methacrylate) (PMMA), polyethylene, polydimethylsiloxane (PDMS) and polycarbonate. Although they are great for rapid prototyping and as disposable chips, they do have issues with tolerances because of their softness and autofluorescence.

5.3 THIN FILM FORMATION

Thin film deposition and growth on top of the substrates is an essential step towards the fabrication of most devices. They are essential for a variety of purposes, *viz*. as masking materials, sacrificial layers, structural materials *etc*. Thin film deposition can take place either by chemical reaction at the deposition surface, known as Chemical Vapor Deposition (CVD) or by a physical process, known as Physical Vapor Deposition (PVD).

In case of PVD, the material to be deposited is converted either into its vapor state by heating (thermal evaporation), or physically bombarded out using ions (sputtering). The vaporized form of the material to be deposited is then condensed onto the surface of the target uniformly.

In one form of CVD, gaseous precursors are introduced inside a chamber under vacuum and then heated up to high temperatures, when the gasses react at the surface of the material to be coated to form a uniform thin film. The precursors are chosen so as the by-products formed are gaseous as well and they are pumped away from the surface.

Thin films can also be grown on surfaces using epitaxial growth, where the substrate acts as the seed crystal. Another technique used for both thin and thick films is electroplating where a conductive seed layer is deposited on the surface to be electroplated. The substrate is then immersed in an electrochemical bath where electrochemical reactions produce a uniform metal layer on the substrate.

Plastics or polymer films can be deposited by a variety of methods. Polyimides, spin-on-glass (SOG), PDMS, photo sensitive chemicals (photoresists) are used both as mechanical structures or sacrificial layers. They are normally deposited by dispensing a small amount of the material on the surface of a flat wafer and then spinning at a high speed, which gets rid of the excess material while leaving behind a uniform layer of the material.

5.4 PHOTOLITHOGRAPHY

Photolithography is the process of transferring patterns from an optical mask onto the surface of bulk material with the help of a photosensitive chemical known as photoresist. The pattern to be transferred is first patterned onto a glass plate using microfabrication or printed onto transparency films. Based on the type of photoresist being used, the mask could either be a negative of the desired pattern on the substrate surface or a positive pattern. In order to fabricate a complete device, a set of optical masks is generally used, with each mask used for the patterning of a specific layer.

Photoresists can either be positive or negative. In case of positive resists, the areas exposed by ultraviolet (UV) light undergo chemical changes making it soluble in a chemical solution, called the developer. The transferred pattern is thus an exact replica of the pattern on the mask as illustrated in Figure 5.1. In case of negative resist, the exposed areas undergo a chemical reaction, making it resistant to the developer solution. The transferred pattern thus in this case is the inverse of the pattern on the mask.

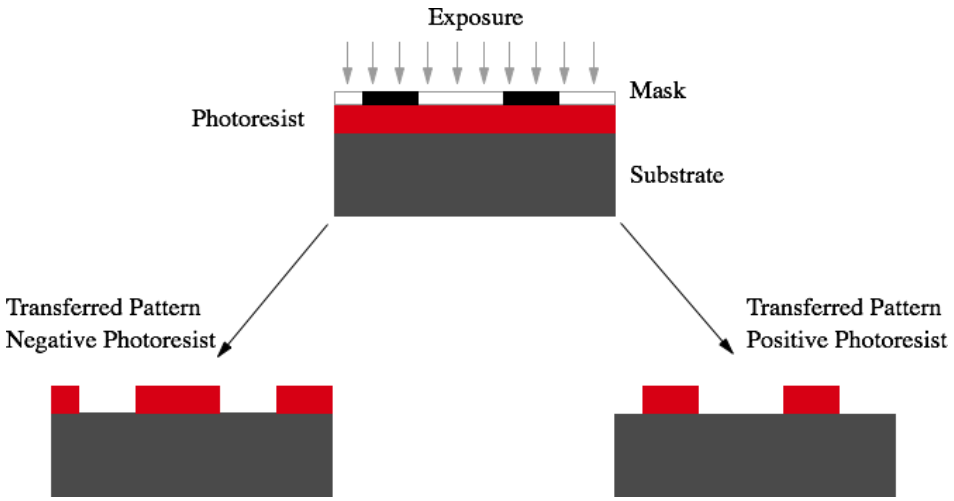

Figure 5.1: Positive and Negative Photoresists

The first step in the photolithography process is the application of a uniform coating of the photoresist material onto the wafer. Spin coating the resist onto a wafer is the most commonly used technique to achieve this, although other methods are used as well. In case of spin coating, a small amount of the photoresist (depending on the wafer size) is dispensed on the surface and then allowed to spread on the wafer. In case of low viscosity resists, the spreading takes place on its own, while in case of high viscosity resists, it is achieved by spinning the wafer at a few hundred RPMs. The spin speed is then rapidly ramped up to a few thousand RPMs depending on the type of resist and the desired resist thickness to achieve a partially dry thin film of the photoresist.

At this point, the amount of solvent present in the resist is still too high for the processing to proceed. The wafer with the resist coating on top is thus heated up to remove almost all of the solvent. This process is called soft baking. The soft baking time and temperature is based on the type of photoresist and its thickness. The soft baking also helps in stabilizing the film by annealing out any residual stress and improving adhesion, resulting in a smoother film. It also helps in reducing the tackiness of the resist surface.

Once the wafer has been properly soft-baked, the wafer with the resist coating is exposed through the optical mask for the pattern transfer. For most applications, mercury lamps have been used as the illumination source. The broadband mercury light source with a wavelength range of 200 nm to 600 nm for the strongest peaks could be used for most of the standard photoresists, *viz*. I-line (365 nm), H-Line (405 nm), G-Line (436 nm) and E-Line (546 nm). In the simplest form, a 1:1 exposure system is used, in which the mask is kept either in contact or in close proximity to the photoresist coated wafer as is illustrated in Figure 5.2. Contact lithography requires inexpensive hardware and can achieve high optical resolution. However, in case where even higher resolutions are required, projection printing is used. In this case, a smaller image field is stepped through the wafer in discrete steps. The reduction system allows coarser mask design while still enabling finer features on the photoresist substrate. Reductions of 4X or 5X are typically used in this process.

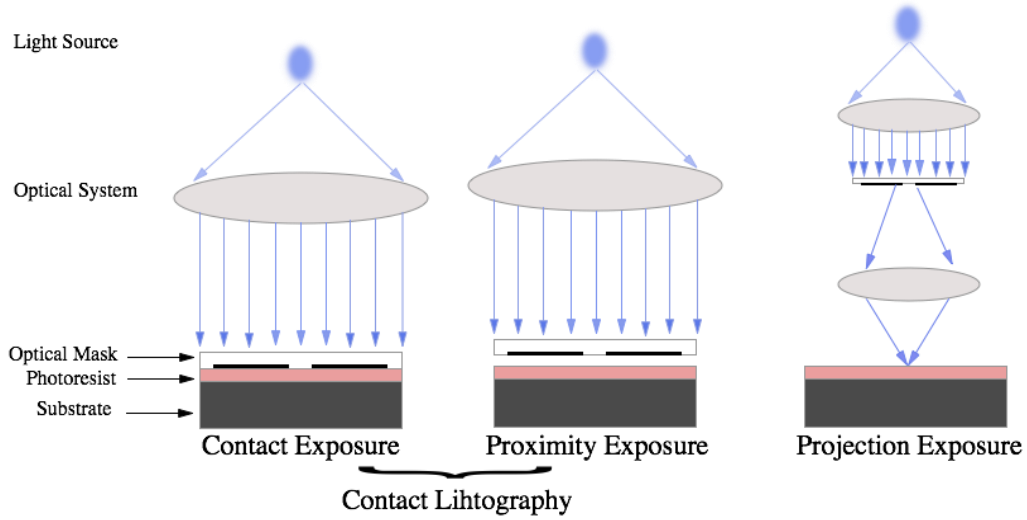

Figure 5.2: Types of Exposure Techniques Used in Photolithography

The exposed photoresist coated wafer is then developed in a chemical solution, which removes either the exposed or the unexposed areas according to the type of photoresist used. The final step in the photolithography process is the hard baking. In

this step, the resist and the wafer is heated to a temperature higher than the soft-bake temperature to completely get rid of the solvent, enhancing adhesion to the substrate and hardening the material to withstand the subsequent processes.

5.5 ETCHING

Etching is a critical step in the microfabrication process, and normally multiple etching steps would be required for the fabrication of a complete device. Etching involves the chemical removal of a material in the microscale, usually in the presence of another material that is resistant to the chemical used for etching, called the mask. It is used both in case of surface micromachining to remove surface layers, and in case of bulk micromachining to fabricate deep structures in the substrate. A proper choice of chemical and the masking material is essential to ensure a good selectivity of the etching process. The etch selectivity is defined as the ratio of etching rates of the substrate material and the masking material. A higher selectivity thus means the material to be etched gets etched at a faster rate than the masking layer and is thus preferred.

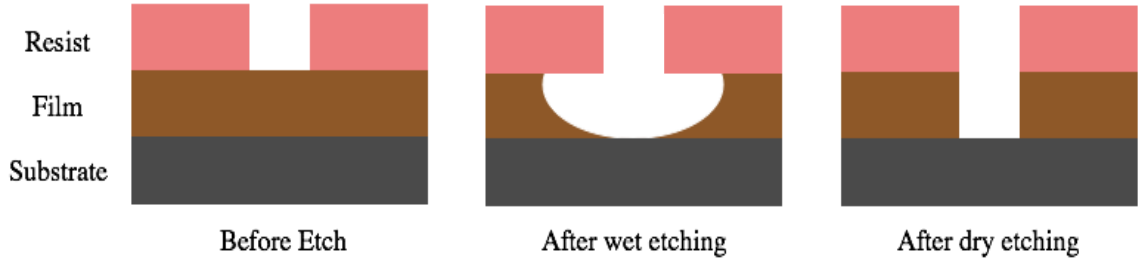

Figure 5.3: Schematic of Wet and Dry Etching Outcomes

The etching process can be categorized into two distinct categories based primarily on the type of etchant used. When the etchant is liquid phase, it is called wet etching, and when the etchant is plasma phase, it is called dry etching. The profiles of the etched material after wet and dry etching are illustrated in Figure 5.3. Each of these types of etching can be further categorized into two sub-categories *viz.* isotropic etching and anisotropic etching. In case of isotropic etching, the etchant etches the material

equally in all directions. In case of anisotropic etching on the other hand, the etchant preferentially etches in one direction over the other.

In case of wet etching, the material to be etched is immersed in a bath of the etchant chemical. For better process control and to ensure uniform etching of deep structures, agitation of the etchant solution is generally employed. Wet etching is generally isotropic, requiring compensation of the mask opening geometry to account for the undercut etching underneath the mask in the lateral direction as seen in Figure 5.3. However, in certain cases, wet etchants can also be used for anisotropic etching when used to etch crystalline materials. This is because of the preferential etching of one crystalline orientation over the other. For instance, in case of silicon, potassium hydroxide (KOH) etches <100> crystal face 400 times faster than the <110> face. Anisotropy in silicon, for instance, can also be achieved by selective doping of the material thus changing the etch rate of the doped region with respect to the bulk material. Wet etching is not ideally suited however in a variety of scenarios where fine control over the etched features are required. Because of isotropic nature of the etching, geometry compensation becomes a critical parameter and the same mask cannot be reused for different etch depths thus limiting their reusability. Also, high aspect ratio structures cannot be achieved as the lateral direction is always etched at the same rate as the vertical direction. Additionally, wet etching places a stringent requirement on the integrity and adhesion of the masking material. However, They have a lower processing cost, can provide a very high etch selectivity and the chemistry can be tuned to yield relatively high etch rates leading to faster turnaround times. Consequently, it is one of the most commonly used techniques in laboratory environments.

The dry etching process involves the interaction of ion and neutral species produced in a plasma discharge with the substrate. The plasma is essentially a partially

ionized gas containing positive and negative ions, reactive neutrals, electrons and radicals formed by the application of a large electromagnetic field to the gas inside the reactor [84]. The dry etching technique can be broadly classified into three types:

1. Plasma Etching, which is essentially a chemical etching of the target material using plasma in the gaseous phase. It has a high etch rate and good selectivity, but is isotropic in nature.

2. Ion Beam Etching, also known as ion milling, which is purely a physical sputtering process without chemical reactions utilizing noble gas ions. It is completely directional in nature, but has a poor selectivity and very low etch rate.

3. Chemical Physical Etching, which is a combination of both chemical plasma etching and ion beam etching. Consequently, it has a reasonable etch rate with good anisotropicity and acceptable selectivity.

The two most important factors in case of dry etching are anisotropicity and selectivity. A perfectly directional process would have zero etch rate in the lateral direction and an infinitely selective process would have zero etch rate of the masking material [84]. However, it is not possible to have an etch process satisfying both of these conditions. Ion milling is a type of fully directional etch, while in case of plasma etching a higher selectivity can be achieved since the process is dominated more by chemical reactions rather than sputtering thereby making the process faster as well. Of the three techniques mentioned above, Chemical Physical etching forms the basis of most of the critical etch processes that are being carried out currently. In case of the chemical physical etching the chemical etching component and the ion milling component can be tuned to generate the desired etch profile. The Chemical Physical Etching is further classified according to the reactor type namely, Reactive Ion Etching (RIE), Inductively Coupled Plasma (ICP), Magnetically enhanced RIE (MRIE) *etc*. However, compared to

wet etching, dry etching has a higher processing cost, much lower etch rates and lower selectivity.

During the fabrication of a complete device however, both wet and dry etching techniques are employed depending on the requirements of the particular process step.

5.6 SOFT LITHOGRAPHY

Soft lithography is defined as a set of techniques that encompasses a number of techniques for the patterning of elastomeric materials like polyimide, PMMA, polyethylene, PDMS *etc*. using methods such as printing and molding to transfer required patterns using elastomeric stamps or molds respectively. Because of the use of elastomeric materials, which are essentially "soft" materials, this method of pattern transfer using these materials are called soft lithography.

Although soft lithography builds on the process of photolithography, it is markedly different from it as it focuses on a one-time fabrication step of the master and then replicating subsequent devices using elastomeric materials. The master fabrication takes up a lot of effort and resources, however, since the molding is performed using the cheaper elastomeric materials, it has a huge cost and complexity benefit over standard photolithography techniques. Soft lithography can be performed at ambient room conditions and does not require the use of a clean room thereby needing minimal capital investments. The standard semiconductor photolithography process also generates a lot of chemical waste. Having a single master generation step using traditional photolithography techniques thus reduces the overall waste generation as well. The fabricated elastomeric chips being so cheap can be used as disposable devices, which makes it really attractive for biology and biochemistry where contamination is a concern. Because of the need for only one microfabrication step, soft lithography devices molded

out of an elastomeric material can be realized from an idea in less than a day, thus they are ideal for fast prototyping during the design phase.

5.6.1 PDMS as a soft lithography material

Although a variety of materials have been used for soft lithography, the use of PDMS as the casting material has become the material of choice for the fabrication of various microfluidic devices for not only rapid prototyping, but for some commercial devices as well. PDMS have been around for a long time, being used as caulk, heat sink material, implants, *etc.* before it gained popularity as a material for the fabrication of research devices. Being much cheaper than other materials normally used in microfabrication, it can be thus be utilized in rapid prototyping and the fabrication of disposable devices without worrying about material and processing costs. As such it has been extensively characterized and studied and its attributes make it an ideal choice for life science applications.

It is normally available as a two-part polymer that needs to be mixed at a certain ratio for it to set into a viscoelastic polymer. The curing time after mixing is greatly dependent on the temperature, and can be achieved anywhere between 24 hours at room temperature to 1 hour at 80 ^{o}C. This increases the shelf life of the individual components as the individual components doesn't cure on its own. It is extremely easy to work with and very forgiving both in terms of the mixing ratio and the curing temperature/time. Although popularly used a casting material, photopatternable PDMS have also been explored [85], [86]. Additionally, PDMS can also be spin coated after diluting it using hexane or Tertiary butyl alcohol (TBA) to form thin films [87].

Being optically transparent in the visible and UV range, it is an excellent material of choice for applications requiring imaging, which is an important consideration for biological devices. Most applications in biology deal with some type of fluorescence

imaging, and PDMS have been reported to have a very low constant autofluorescence across a wide range of excitation wavelengths similar to glass [88]. Furthermore, the biocompatibility of PDMS has been well established with it being used as implants in human health applications for decades. It is also stable under exposure to most chemicals. The gas permeability of PDMS is also used to the advantage of supplying oxygen to cells inside otherwise fluidically closed cell culture chips. Being a soft material, PDMS is easily deformable and this allows for the realization of fluid-tight connectors as well as diaphragm membranes for the realization of on-chip valves. Peristaltic pumps have also been realized in PDMS, which take advantage of its elastic nature.

PDMS is also both thermally and electrically insulating. It is also stable at the temperature ranges normally associated with biological processes. Being electrically insulating, it allows the integration of electronic circuits and heating elements inside the devices fabricated using PDMS. PDMS is also used as a protective layer to protect electrical pads and connectors from being corroded or shorted in the presence of ionic solutions common in microfluidic applications.

Another appealing aspect of PDMS devices is the ease with which they can be bonded to one another and to silicon or glass surfaces. Silicon can be bonded both reversibly or irreversibly to those surfaces. By nature PDMS is hydrophobic, however plasma treating the PDMS surface can render it hydrophilic as is necessitated under certain experimental conditions. Plasma treatment is also performed in order to irreversibly bond PDMS to glass surfaces to form sealed devices.

However, there are certain limitations to the use of PDMS. Being intrinsically hydrophobic, PDMS tends to absorb small hydrophobic biomolecules and proteins on its surface. Furthermore, water has been reported to evaporate through PDMS thereby changing the osmolality of the cell culture solutions in case of cell-based studies using

PDMS devices. Nonetheless, the advantages of PDMS far outweigh the disadvantages and researchers have approached to design around those advantages and in many cases used it to their advantages [89].

CHAPTER 6

DESIGN APPROACH

6.1 INTRODUCTION

There are a number of miniaturized, microfluidic PCR chips that have been developed over the years. A comprehensive review of the various solutions is provided by Zhang and Xing [46] in which they review and compare various microfluidic chips based on PCR chip architecture, on chip PCR volume, reaction speed, cross-contamination issues, fluidic and temperature controls and detection techniques. However, the unique requirements of the platform envisioned by MBARI in requiring a high-throughput, fully integrated and automated platform with the constraints as mentioned in the previous section presented a unique challenge in itself. Consequently, this body of research is aimed towards the design and development of a integrated microfluidics based quantitative PCR device by building on the current technologies and implementing novel enhancements in the design and fabrication for fluidic components, PCR thermal cycling, optical emission and detection, embedded control and systems integration. As reviewed by Zhang and Xing [46], [90], there are a number of microfluidics based PCR devices, however most of these systems are isolated devices, and thus are not suitable for deployment as fully automated integrated devices.

In order to come up with the best fit solution that meets the expectations while remaining within the constraints laid down by the long-range AUV platform as outlined in the previous section, an extensive study of the possible approaches was necessitated. At the heart of this implementation is the PCR device. There are a number of different approaches to perform PCR that has the potential to be miniaturized as reviewed in [46], [90]. So, in the first phase of this work I worked on the identification of the PCR approach that would be feasible with the requirements and constraints. Advances in PCR

technology have provided a wide variety of approaches and protocols that make it possible to detect even single molecules. However not all of those technologies are compatible with a small sized, low power and field deployable platform. Consequently, during the initial phases, the focus was to identify the appropriate technological approach that can be implemented on this type of platform.

An automated platform necessitates reagent storage and delivery along with the actual PCR procedure. In most laboratory settings, the PCR reagents and primers are stored under controlled temperature conditions inside a freezer. However, this is unrealistic for field deployments. Consequently, in order to identify the optimum qPCR method, the PCR reagent storage and delivery was looked at first. I came up with a decision tree as illustrated in Figure 6.1 and evaluated all the possible approaches to come up with the optimum solution.

Since the primary objective of this work is achieving qPCR, the entire process is broken down into the main components of the process. They process was split up into the primer storage and the partitioning technique that dictated the fluidic system design, the thermal cycling technique and the imaging technique.

6.2 Fluid Handling Mechanism

The first task was the identification of the type of primer storage as it determines the overall design of the system. There are three possible approaches of storing or functionalizing the primers needed for the PCR experiment as illustrated in the Figure 6.1, the primers can either be in the solid phase, in a lyophilized state or in a liquid phase.

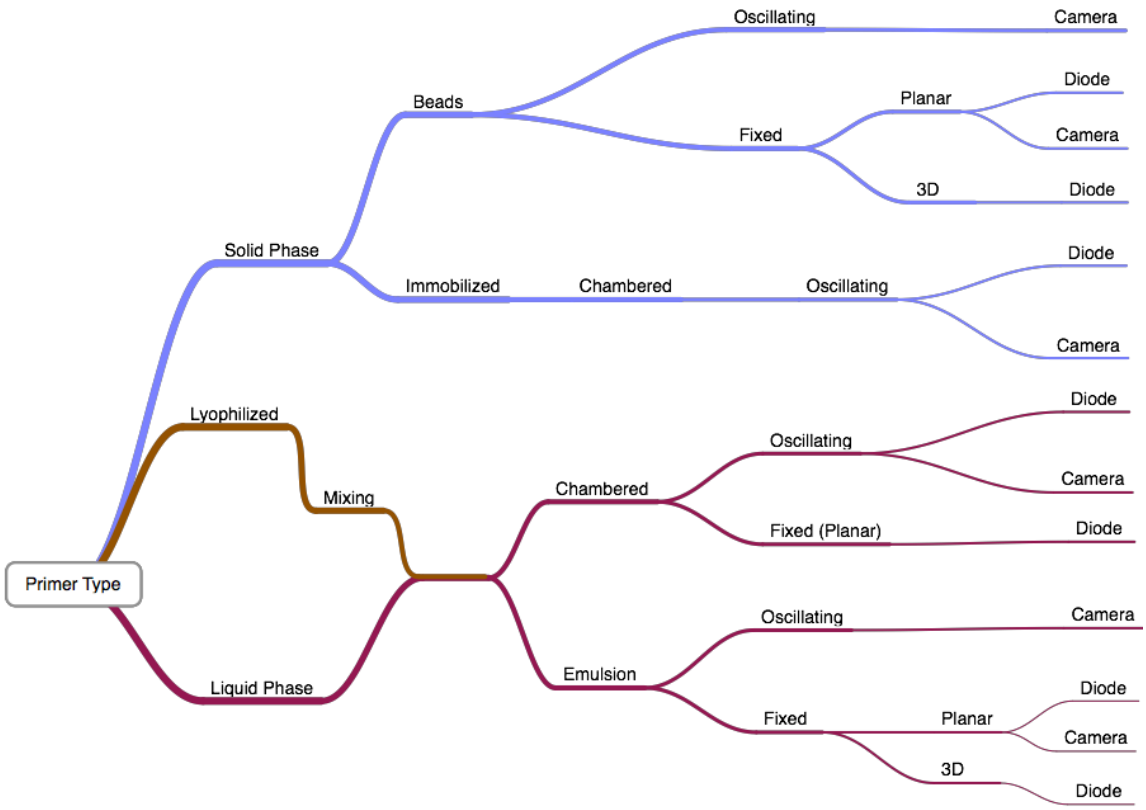

Figure 6.1: Decision Tree Showing Possible PCR Analysis Pathways

In case of solid phase, the PCR primers are covalently bonded to a functionalized surface and thus instead of free-floating primers, surface-bound primers are used to amplify DNA. Normally, the 5´-end of the primer is covalently bonded to the surface leaving the 3´-end to take part in the DNA hybridization. For solid-phase PCR the surface, the density of the attached primers need to be dense enough for detection post hybridization. Also, the covalent linkage of the primer to the surface needs to withstand the heating and cooling cycles associated with the PCR process [91]. The primers can either be functionalized on the surface of the chip or on beads that are suspended in the solution. In any case, since the primers are bound, the diffusion of the DNA strands alone leads to hybridization, which is not an attractive option for microfluidic devices in which fluid flow is laminar. Furthermore numerous studies have found the efficiency of solid-phase PCR to be significantly less than traditional solution based PCR [92], [93].

Lyophilization is a process by which biological samples are freeze-dried to preserve them for long periods. It is essentially a dehydration process in which the material is frozen and then the surrounding pressure reduced to sublimate the water directly from the solid to the vapor phase. The powdered material is then reconstituted in a buffer solution prior to the experiment making it an attractive option for the purposes of long time storage of the primers inside the mobile ESP platform. The reconstitution of the freeze-dried primers is a critical step that needs to ensure that the entire material is re-suspended in the buffer; otherwise it will change the ratio of the components in the PCR mix. Furthermore, care must be taken to ensure that the lyophilized powder is stored in a completely sealed environment to prevent reabsorption of moisture. Attaining a hermetic seal in an environment that is expected to get really humid, and to solubilize the powder completely in the buffer solution in an automated matter repeatedly, is not quite feasible using a microfluidic device.

Performing PCR with the primer, probe and Mastermix in the liquid phase is the most commonly used technique that is the standard in most lab environments. Furthermore, it is the most widely used technique for microfluidic adaptation both to reduce expensive reagent consumption as well as to enhance automation [46]. Thus, this form of reagent storage was identified as the best solution for the development of the analytical module.

The next critical step that was focused on was the reagent delivery process. There are in general two methodologies of forming the actual PCR reaction volume in case of high-throughput microfluidic devices. The first approach deals with compartmentalizing the reaction volumes into separate wells like what is achieved in the Fluidigm® Dynamic Array™ integrated fluidic circuits (IFCs). These chips from Fluidigm® have thousands of individual reaction chambers along with an intricate network of on-chip microfluidic

channels that also performs various liquid handling functions like merging, mixing, valving *etc.* [94]. But although this type microfluidic device is good for high-throughput analysis it is not quite reusable because of cross-contamination issues even with cleaning. For a platform like the ESP, which requires completely autonomous operation, cross-contamination is a critical factor as is reusability. An emulsion based system on the other hand by the nature of it is quite robust against cross-contamination as the reagents are contained in droplets in an immiscible medium. Furthermore, in case of a droplet emulsion based system, the system can be scaled up without increasing the device size or complexity. The continuous generation of the droplets also is ideal for the high-throughput requirements. A droplet emulsion system can provide a lot of flexibility in the experimental design as well, since simply changing the flow rates can vary generation rate and reaction volume sizes. The droplet generation parameters can be easily tuned to generate uniform sized droplets consistently, which allows quantification of the resultant products. Consequently, this approach was chosen for this work.

6.3 THERMAL CYCLING MECHANISM

One of the most critical steps to achieve a successful PCR experiment is to properly control the temperature of the hot and cold cycles. Too high of a temperature during the denature step potentially can kill off the enzymes; while too low of a temperature would not even let the denaturation to take place. Similarly, for the anneal step, too high of a temperature would not allow proper annealing and extension of the DNA. Consequently, the identification of a proper thermal cycler mechanism is essential for the success of the device. Additionally, because of the constraints of this project of a low-power and portable platform, the thermocycler needs to be optimized for low power consumption, as it is the most power hungry component of the entire device. In case of an oscillating heater, the reagent solution is held in place and a heating element alternatively heats up

and cools down to maintain the temperatures required for the PCR. One issue with the oscillating heater approach is that, the reagent solution needs to be held static, potentially reducing the throughput that can be achieved. Furthermore, because of the nature of the oscillating heater, it requires an active cooling step leading to higher power consumption. Thus, in tune with the requirement to support continuous flow PCR with low power consumption; a continuous flow thermocycler with fixed temperature zones has been identified as the optimum approach for this work. A continuous flow thermocycler can be developed on a planar chip with the heating blocks underneath [95], or as a cylinder heater [96].

The planar chip has its advantages because of the fact that the entire device starting from emulsion generation to detection can be achieved in a single chip. However, because of the long length of the channel necessary, the pressures in such a planar serpentine channel could be very high. The numerous bends also has the potential to introduce non-uniformity in the flow, thereby impacting the duration of the reagent at the two temperature zones. The cylindrical design however is a straightforward and compact approach, ideally suited for continuous flow PCR. In this approach the tubing is wrapped around the two zone heating block with each turn of the tubing around the heater constituting one PCR cycle. This also provides the added flexibility of changing the number of PCR cycles simply by changing the number of wraps around the heaters instead of the need to fabricate a completely new chip, as is the case in a planar thermocycler. The cylindrical design is also advantageous as the entire thermocycler can be wrapped in insulation to reduce heat loss and thus power consumption. Consequently, the cylindrical design was chosen as the optimum design for this work.

6.4 DETECTION MECHANISM

The next part was the identification of a proper imaging technique. Two approaches were evaluated for the detection of the end products of the PCR reaction. In one approach the fluorescence intensities of the end products can be imaged using a charge coupled device (CCD) camera at the end of each cycle [97]. However, CCD approaches are more ideally suited for chip-based solutions with a small imaging area, since highly sensitive CCD with a large sensor area is hard to develop. With the cylindrical thermocycler approach because of the larger area that needs to be visualized, a CCD is not the ideal option. A scanning approach can be used, but it overtly complicates the system design and also for a continuous flow design scanning is not an ideal approach, as multiple wraps would normally contain the emulsions with intensity data. Additionally a CCD camera consumes much more power compared to a photodiode detector or a photo-multiplier tube (PMT), which also has a much better sensitivity under low light conditions.

Because of the enormity of the design and development of the entire system, the PCR device architecture was divided into a number of sub-modules based on the functionality as illustrated in Figure 6.2.

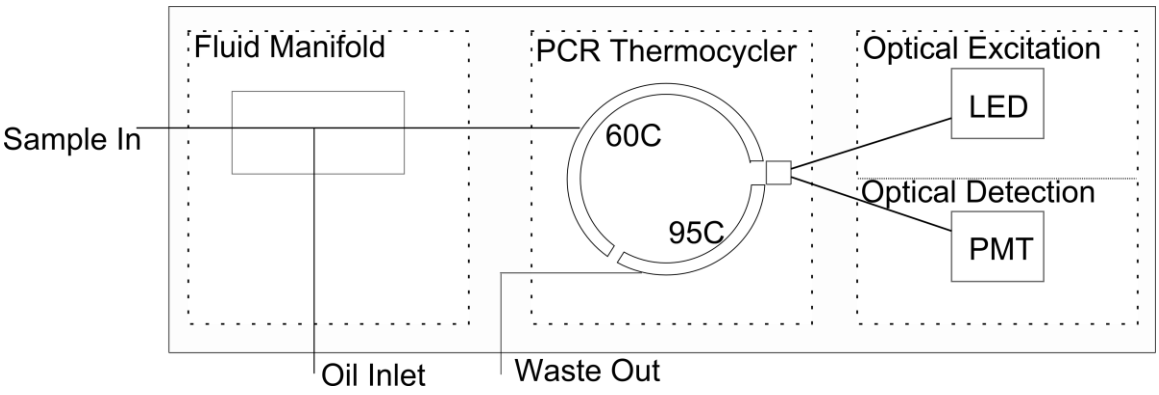

Figure 6.2: Basic System Architecture

As illustrated in Figure 6.2, the envisioned system is schematically represented with the sample coming in to the system as provided by MBARI. Once the sample is

handed over to the bio-analytical instrument, there is no further involvement of the upstream components thereby making it an independent module. The various sub modules as illustrated in the above figure thus are as follows:

1. Fluidic Module
2. Thermocycler Module
3. Optical Excitation and Detection Module

Encompassing all of these modules is the electronic control and the embedded system architecture development towards the functioning of not only the individual components but the integration of the different modules as well for the overall system. Design and development of a fully autonomous device with a strict set of design rules is a challenging effort, as it requires proper definition of interfaces between the various components. In developing the individual modules this was an important consideration keeping in mind the eventual systems integration.

The overall architecture of the embedded system that was envisioned was that of a distributed architecture. In this manifestation, individual microcontrollers would be controlling the sub-modules like thermocycling, optical excitation and detection, pumping, fluid handling *etc.* A master controller would then control all of these individual microcontrollers by coordinating their actions as well as dealing with fault conditions.

This dissertation deals with the design and development of these individual modules as part of the instrumentation necessary for the LRAUV platform. The goal of this work was to have individual functional modules that can be incorporated as part of the platform keeping the constraints and requirements specified earlier as the target.

CHAPTER 7

DESIGN AND DEVELOPMENT OF THE FLUIDIC MODULE

7.1 INTRODUCTION

The first component of the real-time PCR instrument as illustrated in Figure 6.2 was the fluidic module. This was the module that would interface with the upstream sample extraction module. The fluidic module design involves not only the emulsion generation but also additional downstream functions like mixing, coalescence *etc.* Generation of droplet emulsions was best suited for microfluidic chips because of the stability and repeatability of the produced emulsions. This work here presents a system for the mixing of different reagents and the subsequent generation of emulsions and their subsequent detection.

7.2 MATERIALS AND METHODS

7.2.1 Microfluidic Design

The primary consideration for the design of this system was to have a system capable of high-throughput operation in an automated fashion. A microfluidic platform provides the flexibility of producing different sizes of the reagent volume as well. A microfluidic system also can be designed to be robust enough to have a low variability in the sizes of the generated emulsions. To accomplish high throughput generation, emulsions can be formed using microfluidic chips using either of the three emulsion generation schemes discussed earlier.

In this work, the T-junction was identified as the optimal emulsion generation scheme after evaluating all the emulsion generation schemes. One of the challenges faced in the design of the emulsion generation scheme was figuring out a way of to increase throughput that could accommodate up to 50 different primers for a single sample. This entailed mixing of the different primers with an aliquot of the original 50-µL DNA

solution. Consequently, the T-junction geometry was chosen because it holds the greatest promise in terms of scaling up by incorporating multiple emulsion generation channels. Multiple emulsion generation paths can be set up quite easily just by adding additional T-junctions across a single continuous flow channel [98]. Different primers with unique fluorophores then can be used to distinctly identify reactions from each of the channels. Since the sizes of the generated emulsions are a function of the flow rates and the geometry in a multi-channel design it also provides the flexibility to have different reaction volumes.

Consequently, using the T-junction as the base design multitudes of designs were evaluated to identify the parameters of flow rates and channel geometry for achieving emulsions of a certain volume. Another aspect of the design was to come up with a robust way of mixing up to 50 different primers with 50 partitions of the DNA sample. One of the first iterations of the design that was evaluated is illustrated in Figure 7.1. The idea was that the DNA sample would be branched equally into n number of channels where it would come together with the different primers and generate emulsions. By varying the relative flow rates of the sample line and the primers the ratio of sample and primer inside the emulsion can be tuned to the right ratio. Because of the laminar flow nature of the flows, the co-flowing primer and the sample wouldn't mix with each other, but once inside the emulsion because of the tumbling motion of the emulsion through the channel, adequate mixing between the reagents can be achieved in a short period of time.

The use of such an extensive network of on-chip channels to deliver the primers does have a downside however because of the need for a plethora of on-chip valves that needs to be actuated precisely and repeatedly. Furthermore, because of the need for the

entire device to be reusable, the paths exposed to the DNA sample needed to be cleaned with bleach in between runs.

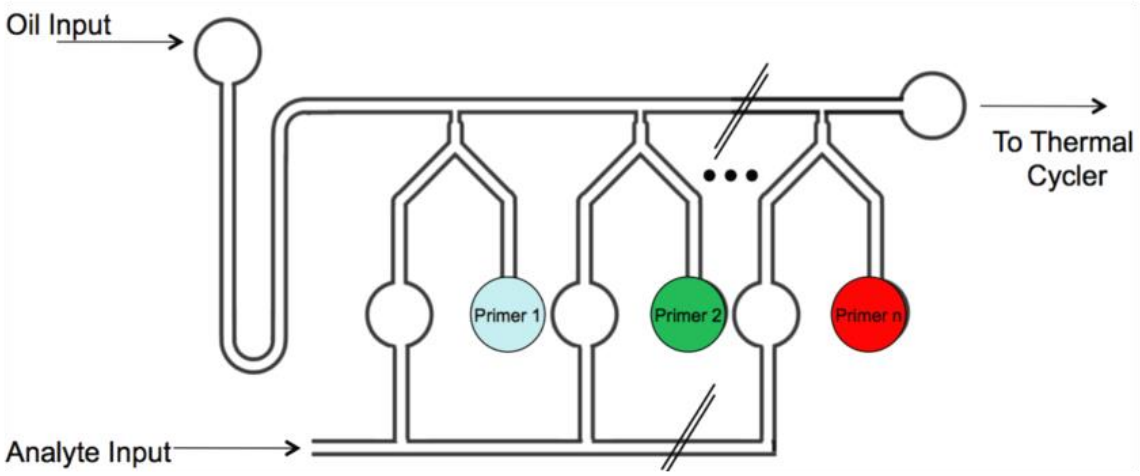

Figure 7.1: Schematic of Microfluidic Device

With the design illustrated in Figure 7.1, achieving a dedicated path to clean the entire system while ensuring that the primers do not get contaminated with the bleach was no mean task. Additionally, on-chip valves can easily trap bleach solutions in them resulting in failure of the subsequent runs. Consequently, an alternate solution in which a single T-junction is required was envisioned as illustrated in Figure 7.2. The emulsion was still generated on the chip; however, the reagent mixing was now performed off the chip thereby making the design more modular as well. The sample delivery path still needs to be cleaned with bleach however, but since the sample after being mixed in the mixing chamber was pushed out with oil as an emulsion already, the sample was not coming in contact with the side channels of the device. This eliminates the need for cleaning out the microfluidic chip after every run. And the device can still be cleaned with bleach without the chip being exposed to the bleach. As illustrated in the figure, the valve can also be external to the chip, which simplifies the chip design aiding in its reusability.

The sample and the reagents are introduced into the mixing chamber by opening the sample inlet valve and the reagent inlet valve while the top valve was closed. After allowing for sample mixing the reagent and sample inlet valves are closed and the reaction volume pushed out by the oil to the emulsion generator chip via the open top valve.

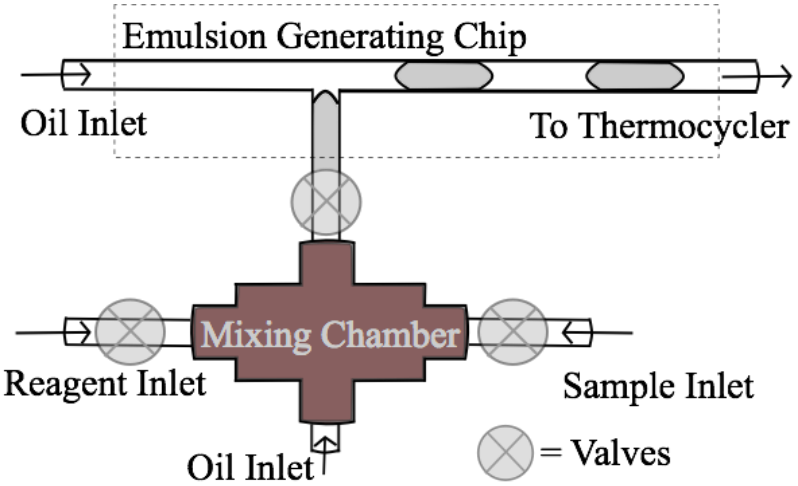

Figure 7.2: The Fluid Routing Scheme

Both approaches were evaluated with the relative merits and demerits of each approach determining the optimal solution for designing the overall system.

7.2.2 Microfluidic Device Fabrication

Because of the constantly changing requirements due to the complexity of the design, to arrive at the optimum design a number of design iterations needed to be evaluated. This necessitated a prototyping design process with a quick turnaround and low material cost. Consequently, for the fabrication of the microfluidic devices, two approaches were followed as part of this work. Some initial devices were fabricated out of polymeric laminates for quick testing, while later devices were fabricated as glass-PDMS hybrid chips for greater control over the channel features.

A number of designs were evaluated to study the importance of the geometry and flow rate of the continuous phase and the dispersed phase in the uniformity of emulsion generation both in terms of generation frequency and volume. Four T-junction designs were evaluated to find the best design in which to bring in two different fluids and form uniform emulsions as illustrated in Figure 7.3.

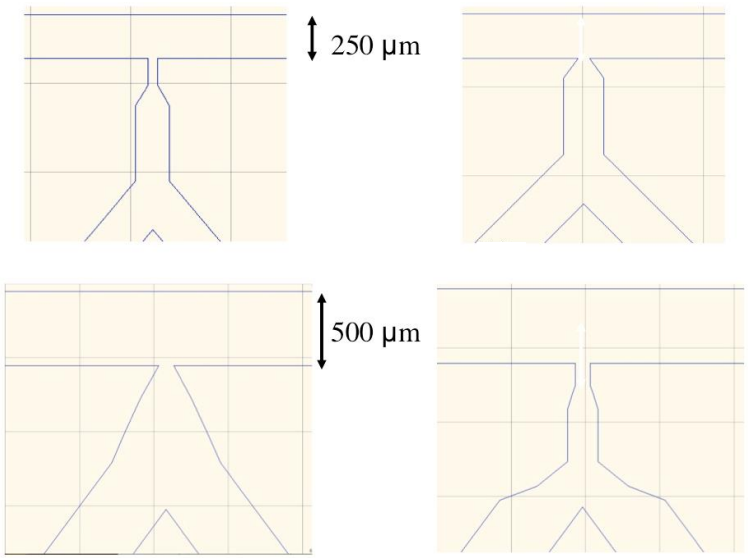

Figure 7.3: Different Designs for the T-channel Emulsion Generator

7.2.2.1 Fabrication of Polymeric Laminate devices

Initial device designs were fabricated with polymeric laminates in which thin sheets of Mylar was bonded together with adhesives as has been demonstrated by Munson and Yager [99]. Thin sheets of Mylar, some of them with an adhesive backing are stacked up in layers with the features cut out using a laser to form these devices.

The first step in the fabrication of these devices started with the design of the features in Autocad®. The design used for the characterization of the emulsion generation parameters was similar to that illustrated in Figure 7.3, albeit for the purpose of simplification using a single channel. Two types of Mylar films were used, one without any adhesive backing, and one with adhesive backing on both sides (ACA) (Fralock, Canoga Park, CA, USA). The Mylar films used were about 250 µm thick while the ACA

films were 50 µm thick with the adhesive being 25 µm thick on each side of the carrier Mylar film giving a total thickness of 100 µm. In order to provide stability to the device, the Mylar and ACA films were sandwiched between two rigid layers of Acrylic sheets that were 0.03 inches thick.

All the polymeric sheets were cut using a 25W CO_2 laser (Universal Laser Systems, Scottsdale, AZ, USA) that interfaced with the AutoCAD® software though a print driver. In order to account for the laser beam width of around 160 µm, the dimensions in the AutoCAD® drawing was compensated accordingly. The devices in this work were fabricated with 5 layers; 2 layers of ACA, 1 layer of Mylar and 2 layers of Acrylic. The bottom layer and the top layer were made out of the Acrylic. The layers immediately adjacent to the Acrylic layers were the ACA layers, the adhesive backing on which helped put bond together the multi-layer device. Figure 7.4a illustrates the features on each of the individual layers with the device being assembled bottom up starting from layer 1. Figure 7.4b illustrates how the final device looks like with a composite of all the layers stacked up.

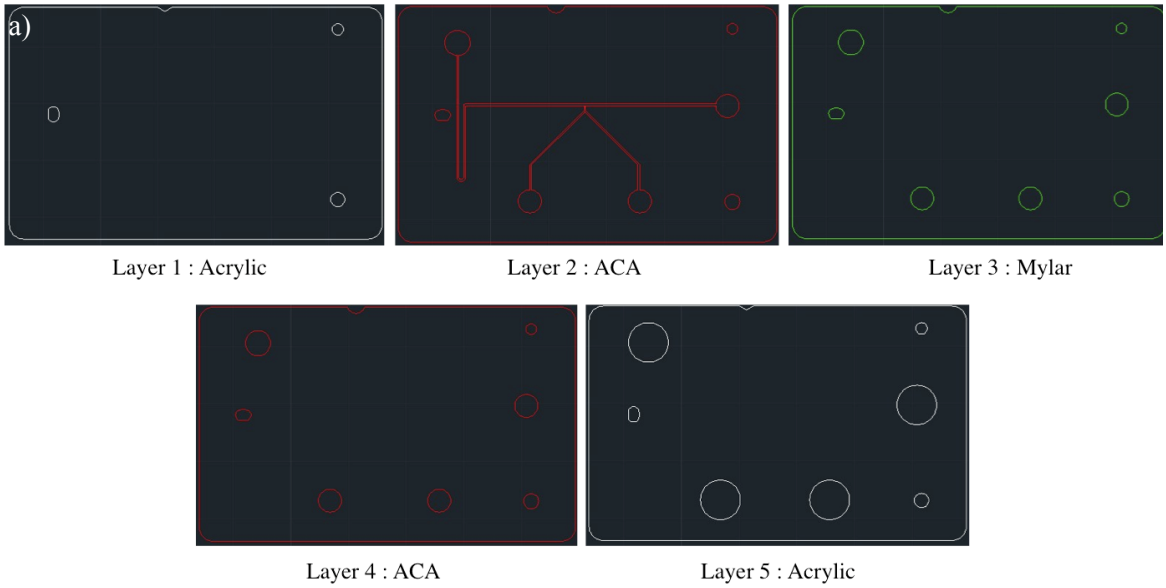

b)

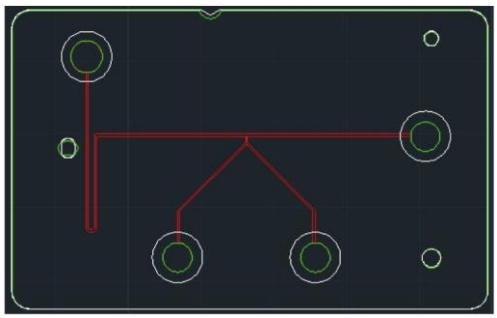

Figure 7.4: a) Features on the Individual Layers on the Polymeric Laminates b) The Design of the Final Device

As illustrated in Figure 7.4a, the actual microfluidic channel was cut in the first ACA layer providing an inclusive channel height of 100 µm. This ACA layer was sandwiched between the lower Acrylic layer and the top Mylar layer. The reason for this was to minimize the adhesive surface in the actual fluidic channel. The additional Mylar layer was incorporated to provide additional thickness to the inner device. The top ACA layer was designed to aid in the bonding of the first three layers to the top Acrylic layer. Additionally, the access holes were designed such that the final ACA layer provides an adhesive surface to aid the attachment of fluidic connectors. Access ports were designed in the top acrylic layer to accommodate Nanoport™ fittings (Upchurch Scientific, WA, USA). After cutting the individual layers they were assembled using a custom built three-prong assembly jig to align the layers. Care was taken during assembly to minimize air bubbles between the layers by squeezing out bubbles using a rolling pin. The Nanoport™ connectors were connected to the device with UV-curable glue to minimize leaks and form a strong bond. The device was connected to a syringe pump (Harvard Apparatus, MA, USA) using PEEK™ (Upchurch Scientific, WA, USA) tubing with an outer diameter (OD) of 1/16th inch and inner diameter (ID) of around 450 µm. The entire device once fabricated was placed on an inverted microscope for visualization as illustrated in Figure 7.5.

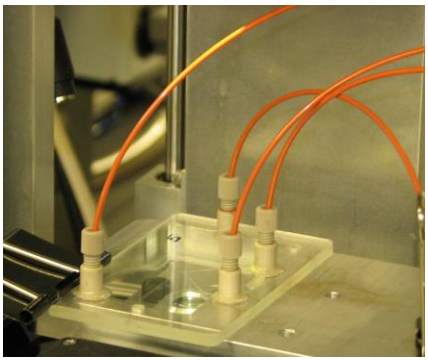

Figure 7.5: The Completed Laminate Microfluidic Chip with the Fluidic Connectors

7.2.2.2 Fabrication of Glass-PDMS hybrid devices

Although polymeric laminates can provide a quick and cheap way of testing a design concept, they are not reliable in their functioning. They tend to clog often as the adhesive reacts with the reagents and develop leaks as well. Consequently for proper analysis of fluidic properties devices were fabricated using PDMS and bonded to glass substrates to form the glass-PDMS hybrid devices.

Master Mold Fabrication

The first step in the fabrication of PDMS devices requires the fabrication of the master molds. The process involves the patterning of a hardened photoresist on a Silicon wafer that acts as the master for the subsequent replica molding of the PDMS polymer.

Using the computer aided design software, Autocad® the mask was first drawn up. In this work, a negative photoresist was identified as the optimum photoresist for the fabrication of the master molds. Consequently, the mask was designed to be the negative of the image to be transferred to the mold. Traditionally masks are made out of soda lime glass plates with patterned chrome features. These masks are great for production runs and applications requiring small feature sizes. However, they are quite expensive especially during the design phase when multiple design revisions are expected. Transparency masks on the other hand provide a much cheaper alternative to the glass plate masks in applications with larger feature sizes. The mask was essentially printed on

a transparent Mylar film using a high-resolution printer. Features as small as 6 μm can be printed with a resolution of around 65000 dpi, while features more than 25 μm can easily be printed with a resolution of around 10000 dpi. While working with epoxy based photoresists, they tend to leave residue on the masks during exposure, which can be difficult to remove. Transparency masks being so cheap can simply be discarded when they become contaminated.

In this work, once the mask design was completed the masks were sent out to an external printing house (Fineline Imaging, CO USA) to get them printed on 5-inch by 5-inch Mylar transparency squares.

KMPR® Process Development

For the fabrication of the masters, in this work, a chemically amplified negative tone I-line photoresist, KMPR® (Microchem Corporation, MA USA), was chosen. It is a high contrast, epoxy based negative photoresist, which can be developed in a standard aqueous alkaline developer, Tetramethylammonium hydroxide (TMAH). KMPR® has similar properties as SU-8, but with less stringent processing conditions and is easier to strip off from the wafer using NMP (N-methyl- 2-pyrrolidone) or Microchem Remover PG. They have a very good adhesion to the substrates, near vertical sidewalls and aspect ratios as high as 18:1 has been reported on Silicon wafers [100].

In order to deal with the range of volumes of the reagents in this work, it was necessary to form high-aspect ratio rectangular channels. This required fabrication of the master really tall structures for the master mold. As part of this work, a process was developed for the fabrication of 200 μm thick KMPR® features on Silicon. The basic process flow for the coating KMPR® onto a wafer involves spin coat, soft-bake, expose, post-exposure bake (PEB) followed by development and rinsing. In order to attain features as thick as 200 μm however, a multi-layer processing was necessary.

A blank silicon wafer was first subjected to dehydration bake at 120°C for about 30 minutes to achieve a completely dry substrate. After taking it out of the oven and allowing it to cool down to room temperature an adhesion promoter, HMDS, was dispensed on the wafer and then spun at 3500 rpm for 30 seconds. Following that, the KMPR® photoresist was dispensed covering the entire wafer. Care was taken to ensure there were no air bubbles as KMPR® is viscous photoresist (Viscosity - 4800 cSt; % Solids - 63.8%). The spin recipe used was a 500 rpm spin for 5 seconds with an acceleration of 100 rpm/second followed by the thickness determining spin with an acceleration of 300 rpm/second at 700 rpm. After allowing the wafer to rest for about 5 minutes to reduce stress it was baked at 100 °C for 20 minutes on a hot plate. After the initial bake, the wafer was allowed to cool to room temperature and then returned to the hot plate at the same temperature for 5 minutes. This process was repeated three times to achieve a uniform soft-bake. After that the second layer of KMPR® was coated on the wafer using the same process parameters. The optimized soft-bake time for the second layer was greater than the first layer. This was because when the second layer of KMPR® was dispensed onto the wafer already coated with the first layer, the solvent from the fresh KMPR® gets absorbed into the preceding layer, which requires a longer soft-bake time to get rid of the solvent at the very end. The initial bake for the second layer was done for 35 minutes and then the wafer was allowed to cool down to room temperature and then heated again at 100 °C for 5 minutes. This process was again repeated 3 times.

The exposure dose for the 200 μm photoresist was then optimized after extensive experimentation as the datasheet didn't provide the exposure dose for thicknesses beyond 80 μm, and it has been reported in [100] that the exposure dose beyond that doesn't follow a linear relationship. Furthermore, because KMPR® is an I-line resist, a long pass filter, PL-360-LP filter from Omega Opticals, was used as it has been reported

to provide superior results [101]. The use of the filter reduces the exposure intensity by about 40% and thus the exposure dose was optimized to account for that as well. The exposure was performed using a EVG620 mask aligner (EV Group Inc, Austria) at a Class 100 clean-room at the Center for Solid State Electronics Research (CSSER) in Arizona State University (ASU). After the exposure, a post exposure bake was performed at 100 ºC for 4 minutes followed by a development step in a 2.38% TMAH aqueous alkaline developer solution (MF-26A) from Microchem Corp. for 30 minutes. The optimized processing parameters for the 200-µm thick KMPR® process are summarized in Table 7.1 below.

Table 7.1: Processing Parameters for 200-µm Thick KMPR® Photoresist

	Spin Speed / Time	Soft-bake Temp / Time	UV Exposure Dose	PEB Temp / Time	Develop Time
Spin 1	700 rpm / 30 sec	100 ºC / 35 min	-	-	-
Spin 2	700 rpm / 30 sec	100 ºC / 50 min	2000 mJ/cm²	100 ºC / 4 min	25 mins

Once the features have been developed on the wafer, the patterned KMPR® was hard-baked at 150 ºC for about 30 minutes to harden the photoresist from further processing. Being thermally quite stable, no reflow was observed and the KMPR® photoresist maintained its vertical sidewall profile, which was essential for obtaining rectangular PDMS channels. Also, the uniformity of the resist thickness was observed to be good. Thus, an optimized process to obtain 200-µm thick KMPR® features on Silicon have been developed and reported here that was used for replica molding PDMS channels.

As part of this work, in order for characterizing the fluidic properties of the emulsion generation, channels with a height of around 90 µm were also evaluated as part of this project. The process development for 90 µm thick KMPR® was undertaken

similarly as described above. In this case however, a single layer process was enough to achieve uniform KMPR® thickness of 90 μm across the entire wafer. The processing parameters for the 90-μm thick KMPR® are provided in Table 7.2. The soft-bake was initially performed for 20 minutes and the cooled down to room temperature before heating and cooling the wafer twice for 5 minutes each at 100 °C.

Table 7.2: Processing Parameters for 90-μm Thick KMPR® Photoresist

Spin Speed / Time	700 rpm / 40 sec
Soft-bake Temp / Time	30 mins / 100° C
UV Exposure Dose	1700 mJ/cm^2
PEB Temp / Time	4 min / 100 °C
Development Time	17 min

Replica Molding the PDMS structures

Once the master mold was fabricated on the Silicon substrate, it could be used for the replica molding of multiple PDMS devices quite easily. Uncured PDMS was poured over the master and then peeled off once cured to give a PDMS structure which was complimentary to the master structure; i.e. raised structures in the master are troughs in the PDMS device and vice versa.

PDMS polymer available as a two-part polymer (base and the curing agent) as part of the Sylgard 184 (Dow Corning, NY USA) kit was used in his work. The base part was added along with the curing agent in a 10:1 ratio by weight and the then mixed thoroughly. Because of the really high viscosity of PDMS, this mixing process introduces air bubbles in the mixture. The mixture was therefore degassed inside a vacuum chamber for about 30 minutes to get rid of the bubbles. The PDMS mixture was then cast onto the master mold.

In order to ensure that the tubing connections to the PDMS structure do not leak, it is recommended to have a thick layer of PDMS so that it forms a press-fit with the tubing and also holds it in place. To achieve thick PDMS layer, thus a containment chamber needs to be formed over the wafer. This was done by cutting out a circular piece of Acrylic bonded with a rubber gasket on the side facing the wafer and using that as the chamber. In order to prevent seeping of PDMS from underneath the Acrylic structure, four binder clips were used to clamp it to the wafer as shown in Figure 7.6. Although PDMS separates from Silicon surfaces after curing, it is not uncommon to have some stiction that leads to tearing of the PDMS around sharp edges of the structures of the master. For this reason, the entire thing illustrated in Figure 7.6 was silanized to passivate the surfaces to aid in the release of the PDMS after curing. To silanize the surfaces, few drops of (Tridecafluoro-1,1,2,2-Tetrahydrooctyl)-1-Triclorosilane was added to a piece of Kimwipe™ wiper paper and placed along with the surfaces to be modified inside a vacuum desiccator for a couple of hours.

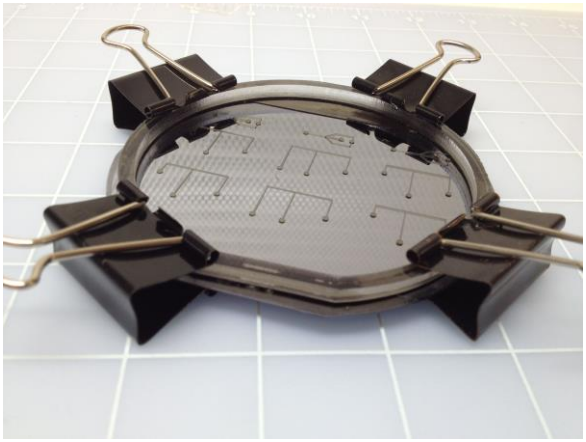

Figure 7.6: The Apparatus for Replica Molding PDMS

During the process of pouring the pre-polymer mixture onto the master, additional air bubbles are formed. Similarly as before, the entire contraption was placed inside a vacuum chamber to get rid of the bubbles for about 30 minutes. Because PDMS

cures very slowly at room temperature, the process was very forgiving. After that the entire contraption was moved inside a 60-^{0}C oven for curing overnight making sure that it sits completely flat so that the cured PDMS doesn't have non-uniform thickness.

Once the PDMS have been completely cured, it was trimmed from the edges and then slowly peeled off of the Silicon master. For this work, individual designs were cut out from the PDMS and bonded permanently to 2-inch by 3-inch glass slides so that they can be easily visualized under a microscope during operation. Once the individual chips were cut out from the PDMS mold, access holes were cored into them for fluidic connections. A metal syringe needle with its tip sharpened with an OD slightly smaller than 1/16th inch was used to core out the holes so that 1/16th inch tubing can be directly interfaced with the chip.

Once the PDMS chips are ready, they are cleaned with Isopropyl Alcohol (IPA) and dried with Nitrogen (N_2) after clearing out the debris using Scotch Tape. The glass slide to which the PDMS layer was to be bonded was also cleaned with IPA and dried out with N_2. Both of these parts are then put inside a plasma chamber (Harrick Plasma, NY USA) for oxygen plasma treatment. The oxygen plasma treatment modifies the surface properties of both glass and the normally hydrophobic PDMS to hydrophilic. The plasma treatment was performed at 350 mTorr pressure at the Medium power setting for about a minute and a half. The two pieces are then brought together to form a permanent bond and then put in a 60^{0}-C oven overnight to reinforce the bond and to return the PDMS to its naturally hydrophobic state. Performing the plasma treatment for an inadequate time was found to not form a strong bond between the glass and the PDMS. Treating the PDMS for longer times in the plasma chamber causes the surface to become crystalline which causes cracking and also causes poor bonding. Figure 7.7 illustrates the process

flow steps to fabricate the glass-PDMS hybrid microfluidic devices that were followed in this work.

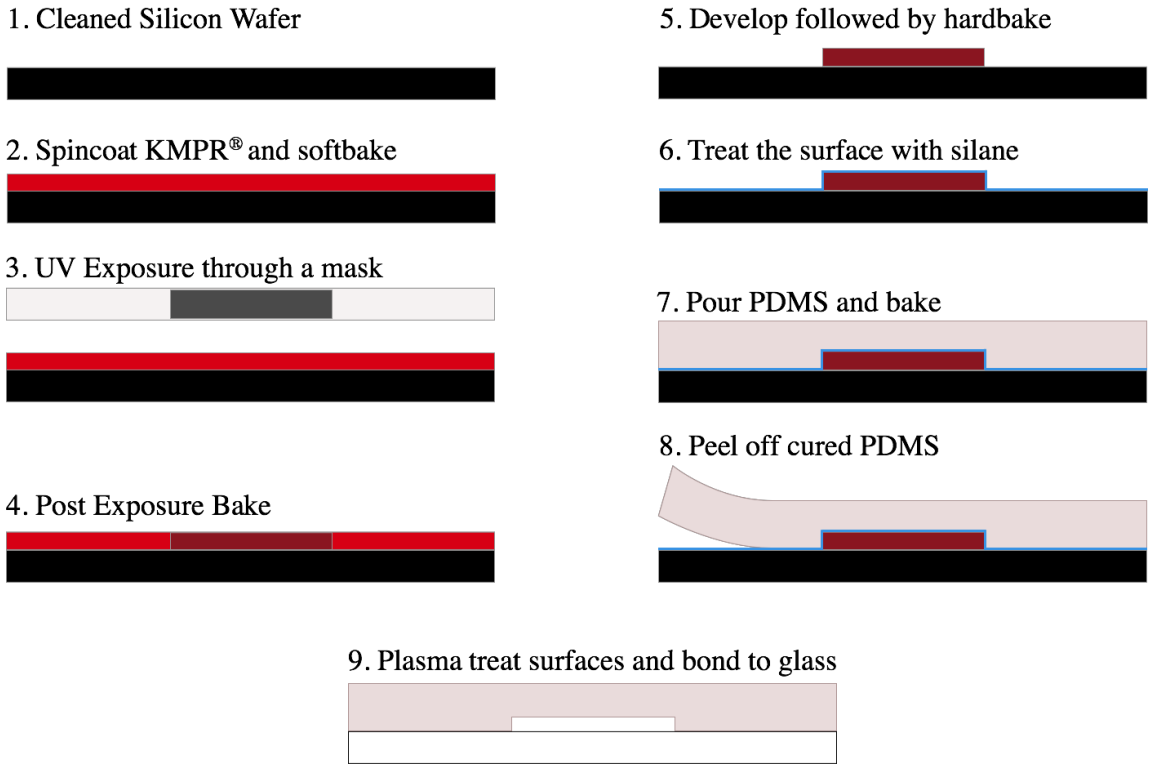

Figure 7.7: Glass-PDMS Microfluidic Device Fabrication Process Flow

7.2.3 Surface Modification of the Microfluidic Chip

Working with biological samples in PDMS devices, especially in the realm of microfluidics is a challenge because of the interaction between biomolecules present in the reagent and the surface of the chip. Because of the hydrophobic nature of PDMS, it also becomes prone to non-specific adsorption of protein molecules. The increase in the surface area to volume ratio in the scales of microfluidic devices also leads to greater adsorption of enzymes and protein molecules to the surface. There are primarily two approaches by which this can be mitigated, either by the chemical modification of the substrate or by the addition of solute molecules in the medium like Bovine Serum Albumin (BSA) [102], polyvinylpyrrolidone (PVP) [95] etc, that preferentially gets absorbed to the surface thereby performing a dynamic coating of the surface of the

device. Interestingly BSA has also been shown to improve the amplification efficiency in emulsion based systems by preventing the denaturation of the enzymes at the oil/water interface [103], but, it has also been reported to cause complications in the fluorescence detection because of its possible interaction with the fluorescent dye/probe [46].

Various surface modification methods have also been used by a number of researchers. One of the challenges is that in case of glass-PDMS hybrid chip, there are two surfaces that both need to be coated with a material with similar properties. Although the use of emulsion microfluidics prevents the reagent molecules to coming on contact with the channels directly, the surface still needs to be modified to ensure that the carrier oil wets the channels preferentially to form a thin film around the reagent volume. Various ways have been extensively reported to make the surfaces hydrophobic and fluorophillic (for when fluorinated oils are used as the continuous phase carrier fluid) using fluorosilanes [104], [105], Aquapel [106], Sigmacote™ [107] . Since DNA has both hydrophobic (the nitrogenous bases: A, T, G, C) and hydrophilic components (deoxyribose sugar and phosphates) a surface that allows the carrier oil phase to preferentially wet it ensures that the reagent molecules doesn't come in contact with the surfaces thereby contaminating it. In this work, all these approaches were evaluated along with the addition of BSA to the reagent solution as well as PicoGlide™ (Dolomite Microfluidics, UK). In this work the coatings were applied to the fabricated devices following the protocol as reported in the manufacturer datasheet.

7.2.4 Selection of Oil for the Continuous Phase

Material selection was a critical part of this work as it had a bearing not only on the functioning of the device but because of the need for compatibility of the materials with the bioanalytical reagents. Identification of the proper oil for the continuous phase was a critical step in the development of this instrument. As explained earlier, the use of

surfactants also plays a critical role in the stability and uniformity of the emulsions generated aside from preventing coalescence of the individual reaction chambers contained in the emulsions.

Successful emulsion based PCR have been reported by researchers using a variety of oils and surfactants. The most number of emulsion based microfluidic PCR work reported in literature have made use of mineral oil using a variety of surfactants like Span® 80, ABIL® EM 90, Tween® *etc.* [32], [103], [108]–[110]. Many researchers have also performed successful PCR using silicone oils like AR-20 [111], [112]. However, an increasing number of researchers are using fluorinated oils in conjunction with fluorosurfactants for emulsion based microfluidic PCR applications like HFE-7500 [113], FC-40 [114] *etc.*

The interest in the use of fluorinated oils for the purposes of PCR has been an appealing choice because of the fact that most organic compounds are insoluble in them which helps in the compartmentalization of the reaction volumes and minimizing transfer between adjacent reagent plugs. Furthermore, they are biocompatible as well [60]. Fluorinated oils have also been reported to solubilize gasses [115] and thus are helpful in microfluidic systems to remove air bubbles to some extent. Fluorinated oils like FC40 and HFE-7500 have very low viscosities (2.2 cSt and 0.77 cSt respectively), and thus was an attractive option, especially in this application because of the long length of tubing required for the entire PCR instrument.

Consequently, for this work, two types of oils were identified for further evaluation. One was the AR-20 oil from Sigma Aldrich (MO, USA) and the other being fluorinated oils (HFE-7500 and FC-40) from 3M (MN, USA). The two fluorinated oils were evaluated independently as well as in a mixture. Because the viscosity of HFE-7500 was so low, it was mixed with FC-40 to attain an intermediate viscosity.

7.2.5 Surfactant Selection

As explained earlier, surfactants play an important role not only in ensuring the stability and uniformity of the emulsion generation process, but also aids in the prevention of coalescence of the emulsions in the system. In this system, the separations of individual reaction chambers are critical as adjacent droplets might contain completely different primers and any coalescence between them would lead to erroneous outcomes.

Based on literature survey, Span® 80 was identified as the surfactant to be used with the AR-20 silicone oil. Span® 80 is a non-ionic surfactant used as an emulsifying agent in the food and pharmaceutical industry. It has been extensively studied as a surfactant for use in microfluidic applications as a surfactant for AR-20 oil. Lorenz *et. al.* performed a series of tests by mixing different ratios of Span® 80 with AR-20 from 0.01% to 1% by weight. Lower concentrations did not produce emulsions at all, while higher concentrations produced too many. They reported their best results using a concentration of 0.1% by weight of Span® 80 [98]. Consequently, that was used as a starting point for the experiments in this work. Two solution were mixed up, one with 0.1% and another with 0.05% by weight of Span® 80. Because of the high viscosity of Span® 80, after adding it to the AR-20 oil, the mixture was vigorously shaken in a shaker and then degassed in a vacuum chamber.

The range of surfactants available for fluorinated oils on the other hand is still quite limited especially for biological applications. This is mostly because of the questionable biocompatibility of some of the surfactant molecules that are found in fluorosurfactants. Fluorosurfactants are generally perfluoropolyethers-PFPE- with a hydrophilic head group that helps in stabilizing emulsions of water in fluorinated oil. Carboxylic terminated PFPE has been reported to have poor biocompatibility [116]. Consequently, chemical modification of the hydrophilic head-group have been

undertaken to enhance the biocompatibility (estimated by the amount of protein adsorption at the emulsion interfaces) of the surfactant. One of the approaches being replacing the carboxylic head-group with a short ethylenoxide chain as reported by Roach *et. al.* [104]. PFPE-PEG based fluorosurfactants have been reported to have shown the most promise for biocompatible PCR applications. However, those surfactants have been either been prepared for some specific applications in the lab or as in most cases, a proprietary surfactant, not available for general use.

For this work, a couple of fluorosurfactants were used for evaluation. Also, based on literature survey a custom fluorosurfactant (FluorN-14600) was obtained from Cytonix (Beltsville, MD USA). It was synthesized in PFC160 oil with a PFPE block (having a molecular weight in the range of 3500-7000) and a PEG block (having a molecular weight of 550). Another fluorosurfactant that was evaluated was Pico-Surf™ from Dolomite Microfluidics. Apart from these, another oil was evaluated that is a proprietary formulation from Bio-Rad, that is sold as a mixture of the oil and the surfactant, marketed as the droplet generation oil as part of their QX100™ Droplet Digital PCR System.

7.2.6 Tubing Selection

Glass capillary tubing was obtained from Polymicro Technologies (Phoenix, AZ USA) with a polyimide cladding to act as the tubing to be used for the continuous flow PCR. Because of the polyimide cladding, these capillary tubing could be wrapped around the cylindrical thermocycler. The glass capillary was chosen because of its rigid structure that would help minimize the effects of fluid capacitance in the long length of tubing resulting in stable fluid flow. Because of the polyimide cladding the capillary had a reddish-brown hue on the outside.

Fluorinated tubing was also identified as another option of tubing for this work owing to their inert nature, flexibility and smoothness. Fluorinated surfaces are also hydrophobic and fluorophilic, which makes it an ideal material for use with fluorinated oils. PTFE (polytetrafluoroethylene) tubing however was not quite transparent which made it difficult to be used for optical fluorescence detection. Consequently, a material similar to PTFE, called Fluorinated ethylene propylene or FEP was chosen as the tubing to be wrapped around the cylindrical thermocycler. FEP retains all the attractive properties of PTFE and on top of that is more flexible and highly transparent. The refractive index of FEP tubing and fluorinated oils used in this work was very similar, which made it an attractive option for optical interrogation. The FEP tubing used for this instrument had an OD of 1 mm and an ID of 500 μm.

7.2.7 Pressure Measurement Scheme

Because of the long length of tubing that would be required in the final instrument it was essential to get a sense of the overall backpressure of the system. Getting a sense of the pressure was also essential for the design of the various microfluidic components, as they need to work at those pressure values. Also, since various oils were evaluated with varying levels of viscosity it was essential to get a sense of the pressure to determine the suitability of the oil to be used. The usefulness of the pressure sensor system was not limited to the design and development phase however. Since it was being designed as an automated system, having a feedback of the pressure of the system was essential to identify any leaks in the system so that corrective action could be taken.

In this system most of the fluid path was through long capillary tubing, so the pressure drop across that length of tubing gives us an estimate of the overall pressure in the system. To estimate the pressure of the system a T-connector was connected in line with the fluid path that interfaced with a Honeywell 26PC Series pressure sensor

(26PCFFA6G) as illustrated in Figure 7.8. This pressure sensor provides a differential voltage that is proportional to the deflection due to pressure on a membrane inside it. The sensitivity of this sensor was 1 mV/psi. Detection of sub-1mV changes electrically could be a challenge; consequently a circuit was designed with an operational amplifier from Texas Instruments (TI), INA141 with a fixed gain of 10 or 100. Like most operational amplifiers, the INA141 requires a dual voltage supply. Additionally, the 26PCFFA6G sensor requires a voltage between 10 – 16 Volts. For this circuit, a V-Infinity VASD1-S5-D15, was selected to supply +15 Volts and -15 Volts off of 5 Volts. To select a gain of 100, pins 1 and 8 of the INA141 was shorted. The capacitors were connected between the power and ground to reduce noise to the amplifier.

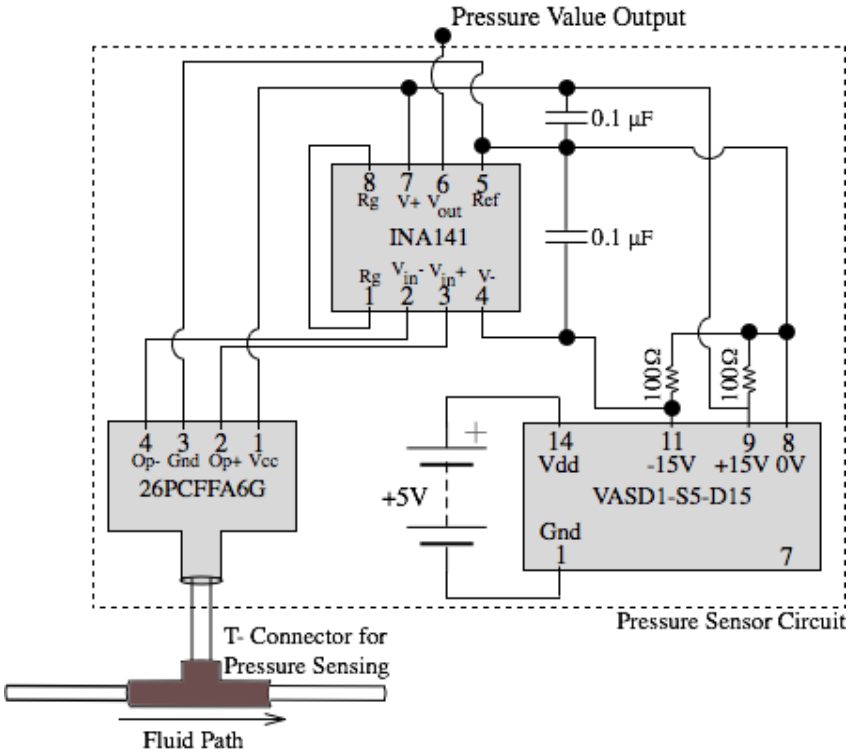

Figure 7.8: Schematic of the Fluid Pressure Measurement Scheme and the Circuitry

7.3 Results and Discussion

Emulsion generation was performed first in the laminate microfluidic chip by the introduction of water and oil in the T-junction through a syringe pump. In order to test

the mixing of the contents of the two branches leading up to the T-junction, water mixed with blue and red dyes were introduced through each channel so that they come together before generating the emulsions. The ratio of the flow rates of the two channels were kept constant at 1:1 in order to achieve a 1:1 mixture of the contents of the two channels in the generated emulsion. The flow rate of the continuous phase (oil) was kept higher than the dispersed phase (water) for the generation of stable emulsions. At a 1:1 flow rate, the fluids flowing through each of the channels were found to be equally distributed flowing out of the T-channel and into the emulsion as seen in Figure 7.9. Additionally, because of the laminar flow nature it was clearly seen that they don't quite mix before the generation of the emulsion. Once inside the emulsion, the two fluids mixed really rapidly and took on a uniform color. All the designs illustrated in Figure 7.3 were evaluated and it was found that the design in which the two fluids came together and went through a narrow nozzle to the junction performed optimally.

Although, a 1:1 distribution in the two channels was observed, the mechanism was found to be unstable as any difference in the fluid resistance in two channels led to non-uniformity in the ratios of the two fluids coming together. Any bump or vibration in the system also led to non-uniformity of the mixing ratios. This was deemed unacceptable since the goal was to design a robust system capable of autonomous operation in the ocean inside a moving submersible. The next part of the work involved characterizing the flow parameters to obtain emulsions of the right volume consistently.

Although the polymeric laminates were a quick and easy way to test out different designs, they were not quite robust and long lasting. Within a few hours of use, the chips clogged up gradually and eventually led to complete blockage of the channels. This was believed to be due to the exposed adhesive of the ACA layer that led to coagulation of the heavy surfactant molecules around the channel walls. Furthermore, it was not feasible to

have any surface coating on the inside of these chips. Consequently, all the subsequent tests were performed with glass-PDMS hybrid chips.

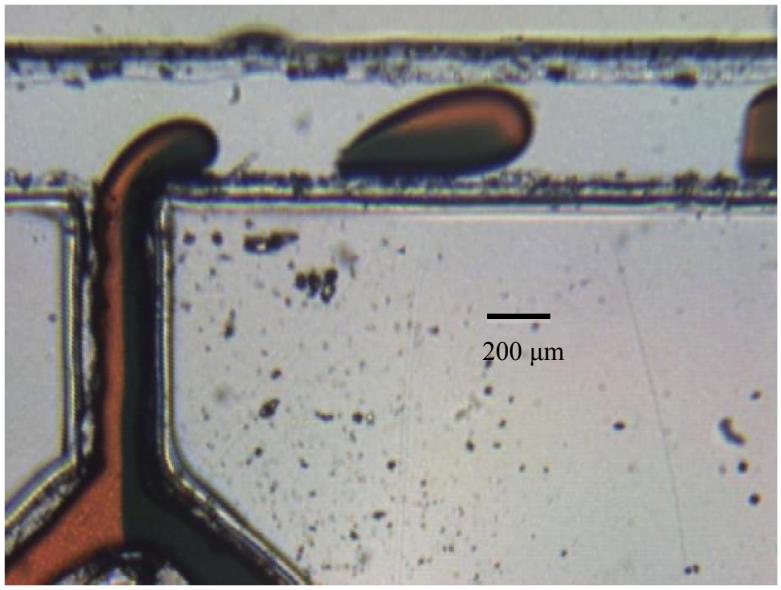

Figure 7.9: Two-phase Multi-fluid Emulsion Generation

The flow rates of the continuous phase and the total dispersed phase were varied to obtain emulsions to characterize the importance of the fluid flow rates and also to get an estimate of the emulsion volumes. When the flow rate of the continuous phase was lower than the dispersed phase, instead of emulsion generation, the dispersed phase did not pinch-off at the T-junction and instead co-flowed with the continuous phase, which was consistent with what has been reported in literature. The volumes of the generated emulsions were studied as a function of the ratio of the continuous phase and the dispersed phase flow rates. For a certain flow rate of the continuous phase, as the flow rate of the dispersed phase was increased, the volumes of the generated emulsions kept on increasing; as did the emulsion generation rate. As the dispersed phase flow rate approached the continuous phase flow rate however, the emulsion generation started to become unstable. There are two factors that played a part in this. Firstly, as the dispersed phase flow rate increased, the shearing effect of the continuous phase progressively got

reduced which led to larger emulsions getting generated until emulsions no longer got generated and the two fluids started co-flowing instead as illustrated in Figure 7.10.

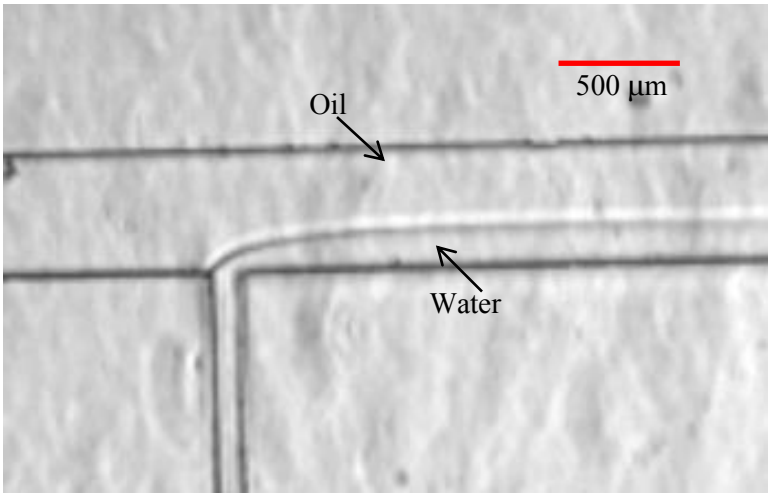

Figure 7.10: Co-flowing Fluids when Flow Rate of Dispersed Phase Greater than Continuous Phase

Secondly, with the increase in the dispersed phase flow, the emulsions were generated at a much higher rate. With the increase in the emulsion generation rate, they formed really close to each other. The surfactant in the solution that is critical in stabilizing the droplets takes a few milliseconds to migrate fully to the interface of the emulsion. Emulsions that come in contact before this can happen thus has a higher chance of coalescence which leads to instability in the process as reported by Baret *et. al.* [117]. Tables 7.3 - 7.5 summarizes the emulsion volumes as a function of different flow rates. As can be seen from those results, the volume of the droplet increased as the dispersed phase flow rate was increased. With any flow rates of the dispersed phase the ones presented in the tables, the generation becomes unstable eventually leading to co-flowing streams.

Table 7.3: Variation of Emulsion Volumes at Different Dispersed Phase Flow Rates with Continuous Phase at 200 µL/min

Dispersed Phase Flow Rate (µL/hour)	Droplet Volume (nL)
20	35.69
40	40.08
80	45.33
100	49.45
150	49.83

Table 7.4: Variation of Emulsion Volumes at Different Dispersed Phase Flow Rates with Continuous Phase at 400 µL/min

Dispersed Phase Flow Rate (µL/hour)	Droplet Volume (nL)
40	34.98
80	36.41
100	43.46
150	44.21
180	47.20
200	46.08
250	48.70

Table 7.5: Variation of Emulsion Volumes at Different Dispersed Phase Flow Rates with Continuous Phase at 800 µL/min

Dispersed Phase Flow Rate (µL/hour)	Droplet Volume (nL)
20	34.27
100	41.14
200	43.37
400	45.21

All the above experiments were conducted using a single T-junction. The performance of the microfluidic system with multiple T-junctions was evaluated next with just two T-junctions. Although emulsions were generated from both the channels independently as well as simultaneously, a lot of variability was seen in the generated emulsions, especially during simultaneous generation. Any time a droplet was generated in one of the junctions it was found to have an affect on the other channel. As has been explained before, the presence of emulsions increases the pressure in the fluid path. Consequently, what was believed to be happening was that when a new droplet was generated it raised the pressure in the system causing the fluid in the other channel to recoil. Simultaneous generation also led to scenarios where after an emulsion was generated from the first channel as it passes the second channel if it was about to generate an emulsion at that point, it led to a coalescence event. Although care was taken to tune the flow rates to ensure that doesn't happen, because of the instability in the system driven by the emulsion generation event, it couldn't be optimized. Figure 7.11 illustrates through a series of screenshots showing the generation of a droplet in the downstream channel and its eventual coalescence with the upstream droplet.

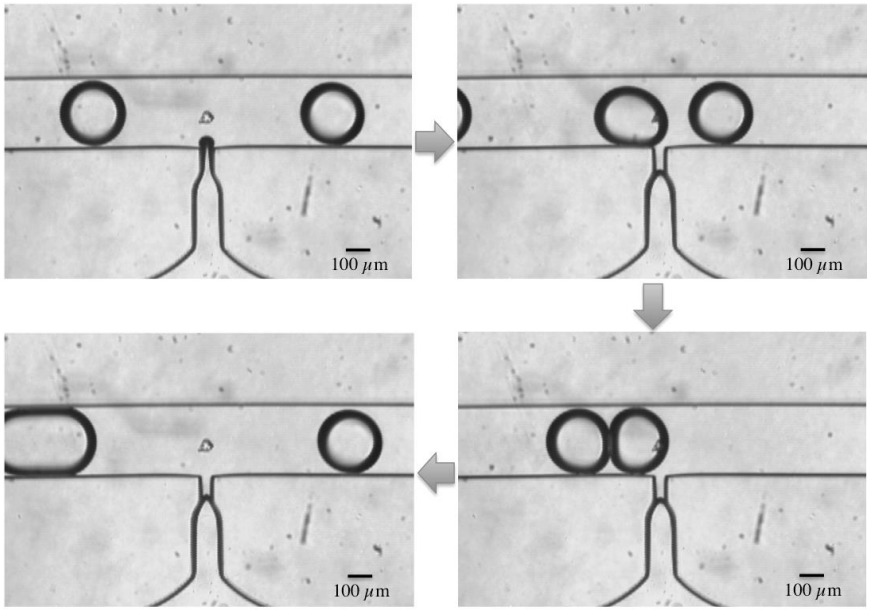

Figure 7.11: Coalescence of Droplets in Case of Simultaneous Droplet Generation from Multiple T-junctions

Even for scenarios in which only one of the junctions were allowed to generate emulsions, as the generated passed through the second junction it would draw out satellite droplets from it over time without any active pumping on the second channel as illustrated by the series of screenshots in Figure 7.12. This effect would be even more pronounced when there would be multiple parallel channels. The use of valves at the junction would no doubt mitigate some of these problems, but that introduces complexities in the design as well as increases the dead volume and the potential for cross-contamination.

Both silicone oil (AR-20) and fluorinated oils *viz.* HFE-7500, FC-40, BioRad Droplet Generation Oil (BioRad, CA USA) were evaluated in this work along mixed with surfactants. Using AR-20 oil, uniform and consistent droplet generation was achieved with both 0.1% and 0.05% concentration of Span® 80 surfactant. However, when the droplets came in contact, coalescence events were observed quite frequently.

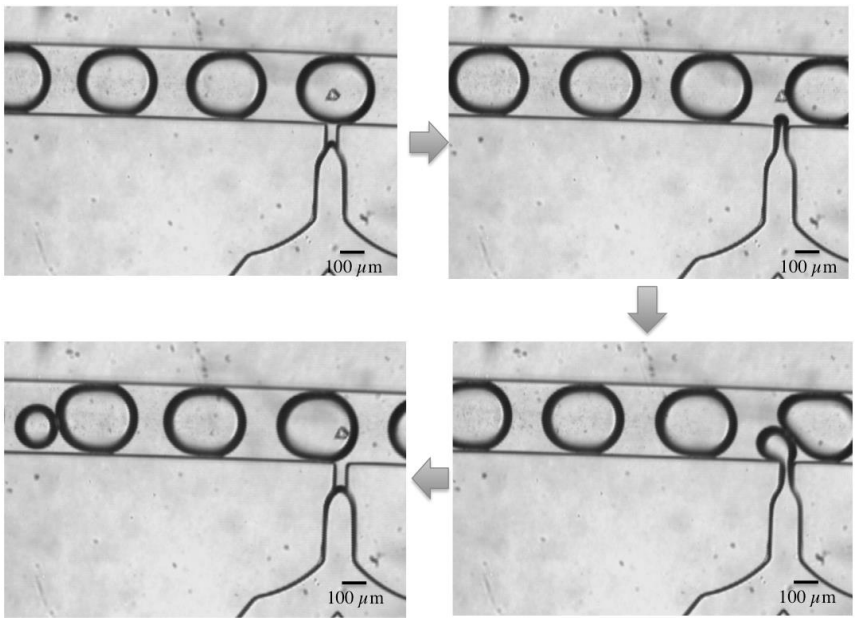

Figure 7.12: Generation of Satellite Droplets from Downstream T-junction without Active Pumping

For the fluorinated oils, FluorN-14600 was added as a surfactant in different ratios to test the stability of the emulsion generation. Surfactants reduce the interfacial tension of the two-phase fluid system thereby aiding in the generation of emulsions and preventing coalescence. However an optimum ratio of surfactant needs to be realized since if the interfacial tension is reduced too much, it might not generate the emulsions at all. While pure HFE-7500 is reported to have an interfacial tension <50 mN/m with water [118], FC-40 has been reported to have an interfacial tension of 54 mN/m with water [119]. This was observed in case of HFE-7500, since it already had a lower interfacial tension with water compared to FC-40 and it has also been reported that the addition of surfactants to HFE-7500 lowers its interfacial tension with water to a much lower value (~1-5 mN/m [120]) than that with FC-40 and water (~20 mN/m [121]) with Krytox® based surfactants. Consequently, while a 0.1% FluorN-14600 surfactant concentration was found to be adequate for HFE-7500, a surfactant concentration of 0.5% was adequate for FC-40. In order to determine the biocompatibility of the FluorN-

14600 surfactant it was added to PCR reagents by itself as well as mixed with FC-40 and HFE-7500 oil and tested in a Applied Biosystems® StepOne™ PCR benchtop instrument and no adverse effects were observed.

The addition of BSA to the reagents during the PCR process did not yield expected results. BSA is supposed to adhere to the walls of the tubing preferentially over the reagent molecules thereby limiting their absorption. However, what was seen was that the continuous oil phase turned cloudy whenever BSA was added to the reagent phase. It was presumably because of the diffusion of the BSA into the oil phase. Consequently, future experiments were performed without the addition of BSA to the dispersed phase.

Because of the higher viscosity of the silicone oil, the overall pressure of the system with the silicone oil was much higher than the fluorinated oils. The pressure was empirically determined using the setup illustrated in Figure 7.8. It was observed that the pressure in the system gradually increased as more and more emulsion got generated and filled the line which was in tune with the mathematical explanation provided by Baroud *et. al.* [61]. Additionally it was found that the pressure when AR-20 was used as the carrier fluid was about 20 times than the pressure of the system when HFE-7500 was used as the carrier fluid.

Stability of the droplet generation was greatly enhanced by the surface treatment of the glass-PDMS hybrid chips. Various chemicals were used to treat the surface in order to have a long-term surface modification of the microfluidic chip. When the chips were used untreated after taking them out of the oven, they performed fine, as determined by the stability of the emulsion generation. This was because of the naturally hydrophobic nature of the PDMS. However, it was seen that after a few days, the PDMS and glass surfaces gradually became prone to wetting. Aquapel and Picoglide™ coatings

performed well during experiments, however, they were not quite stable over long periods of time as was necessary for reusability. Sigmacote™ didn't make any difference in the surface properties when used with the fluorinated oils. The best results with fluorinated oil however was obtained by treating the chips with (Tridecafluoro-1,1,2,2-Tetrahydrooctyl)-1-Triclorosilane and a HFE-7100 (3M, MN USA) using a protocol adapted from [105]. The protocol followed for the surface coating the glass-PDMS hybrid chips is outlined as follows.

- Heat the device in the oven for 15 minutes at 65°C
- Treat the channels with a 2% by weight mixture of (Tridecafluoro-1,1,2,2-Tetrahydrooctyl)-1-Triclorosilane and HFE-7100
- Flush with FC-40 Oil
- Heat in the oven for 60 minutes at 65°C
- Repeat the treatment of the channels with a 2% by weight mixture of (Tridecafluoro-1,1,2,2-Tetrahydrooctyl)-1-Triclorosilane and HFE-7100
- Flush with FC40 Oil
- Heat in the oven for 30 minutes at 65°C

Initially, the fluidic system was tested with glass capillary tubing wrapped around the thermocycler in order to reduce the capacitive effect in the fluid path. However, the glass capillaries were determined to have a couple of issues. Being hydrophilic, it was found to be prone to contamination from the biological reagents as they stuck to the sidewalls leading to cross-contamination as well as loss of reagents. Furthermore, glass capillary tubing has limited bend radius, which limits the size of the thermocycler than can be designed. The 250-µm ID glass capillary from Polymicro Technologies had a minimum bend radius of 20 mm, while the 450-µm ID glass capillary had a minimum bend radius of 40 mm. The larger ID tubing was necessary to reduce the fluid pressure in

the system but leads to a larger thermocycler, leading to greater power consumption. With water flowing through 10 meters of the 250-µm glass capillary at 50 µL/min, the pressure calculated using Equation 4.8 comes to around 11 psi, while with the 450-µm ID glass capillary it was only about 1 psi. This huge reduction was because of the dependence on the radius of the tubing diameter on the 4^{th} order. The system with the lower pressure was obviously preferred because of the ease of designing components for a lower pressure but was not feasible using the glass capillary tubing. The flexible FEP tubing on the other hand provided a much better alternative owing to its hydrophobic and fluorophilic properties, which worked great with the fluorinated oils. Additionally, the glass capillary tubing had a coating of polyimide to enable them to be bent, however this caused a problem with the optical detection scheme because of it non-transparency and autofluorescence. FEP on the other hand was optically transparent and was tested to have very low levels of autofluorescence.

7.4 CONCLUSIONS

The process for fabricating 200-µm features using KMPR® on silicon have been successfully optimized and reported here. This developed process can be useful for not only molding straight-walled PDMS structures using the KMPR® master, but the thick KMPR® layer can also be used as a masking material for deep etching of materials like glass or silicon.

Based on the extensive analysis and characterization of the fluidic components and materials, fluorinated oil was determined to be the optimum continuous phase fluid for this system. HFE-7500 was found to have too low of a viscosity which caused it to flow past the emulsion droplets causing the emulsions to get stuck in certain sections of the tubing. FC-40 and the BioRad Droplet Generattion Oil were found to perform comparably although it was determined that the choice of the droplet volume and the

tubing be chosen in such a way that the emulsions flowing through the tubing are plugs rather than droplets. It was observed that in case of droplets, the lower viscosity fluorinated oils would go past the droplets but not in case of plugs. The optimum surface modification technique and the tubing material were also identified after analyzing a number of different options.

CHAPTER 8

DESIGN AND DEVELOPMENT OF THE THERMOCYCLER

8.1 INTRODUCTION

One of the critical process parameters for a successful PCR was maintaining the reagents at a specific temperature for specific times. Various optimization assays are normally run to tune the optimum temperature and time for achieving successful PCR runs with different primers and reagents. For this work, the cylindrical thermocycler design was chosen as the thermocycling technique because of its advantages over planar designs in terms of better power efficiency and lower fluid pressures.

8.2 MATERIALS AND METHODS

8.2.1 Thermocycler Design

The design of the PCR thermocyler was undertaken based on the biological requirements of the PCR protocol. Taq DNA polymerase was used for this work with a two-temperature PCR protocol at 95 ^{o}C for denaturation and 60 ^{o}C for annealing and extension. Based on biological experiments it was the optimum residence time of the DNA reagents in hot zone was determined to be 15 seconds and in the cold zone to be 45 seconds for a 1-minute PCR cycle for a total of 40 cycles. The thermocycler design was consequently undertaken using these values as the design parameters.

The first iteration of the thermocycle was designed using Aluminum as the core material with two disjointed blocks of aluminum forming a cylindrical structure being held together using a ring made out of Acrylic as illustrated in Figure 8.1.

The heater was designed to be 1.25 inches tall with the OD of the aluminum blocks being 2 inches with the ID being 1 inch making the thickness of the material to be 1 inch. Nichrome wire was used as resistive heaters to heat up the blocks with temperature feedback obtained using thermocouples. Only one heater was used for each

of the 95 ºC and the 60 ºC sections. Since the Nichrome heaters were inserted into an Aluminum body, which is conductive electrically, they were encased in ceramic tubes. The direction of the fluid flow was anti-clockwise with respect to the schematic illustrated in Figure 8.1. In case of the 60 ºC section the heater was thus placed at the end of the fluid path in that zone. The leading edge of the fluid in that section was theorized to still hold the heat off of the 95 ºC side. Additionally, since the aluminum block was chosen to be quite thick it was expected that the heater would equilibrate at the set temperature. The temperatures were controlled using a closed loop control using a CN8200 series temperature controller from Omega Engineering. The thermocycler was wrapped with glass capillary tubing with an ID of 250 µm and an OD of 360 µm.

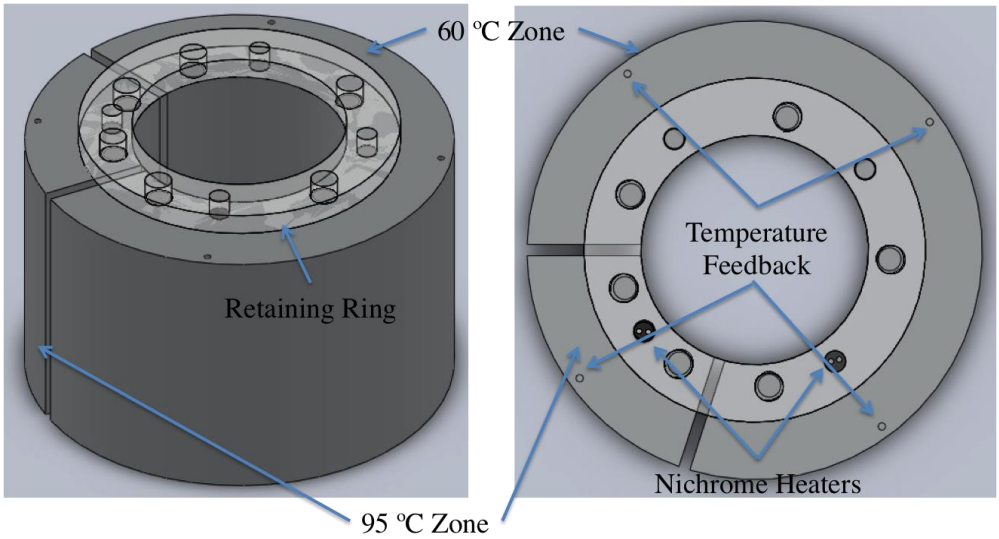

Figure 8.1: Schematic of the First Thermocycler Design

In order to have a thermocycler with less material mass and to ensure better uniformity of the heating profile the next iteration of the thermocycler was designed with thinner aluminum blocks and flexible resistive heaters. Flexible Kapton® heaters (Omega Engineering, CT USA) were sandwiched between two curved aluminum plates with the 95 ºC side separated from the 60 ºC side forming a cylinder as shown in Figure 8.2. Two types of heaters were initially evaluated, one that works off a lower voltage (28 V) but

draws a higher current (KHLV series), and another kind that works off a higher voltage (115 V) and draws lower current (KH series). Because the goal of the this design was to make it work off of a battery voltage in between 10 – 18 V, and since stepping up to voltages of 1115 V from the battery voltage are not quite efficient, the KHLV series was chosen for this work. These heaters are available in various watt densities based on their resistances. For this work, the 5 W/in^2 and 10 W/in^2 heaters (at 28 V) were evaluated. The size of the heaters was chosen to match the inner surface area of the aluminum blocks.

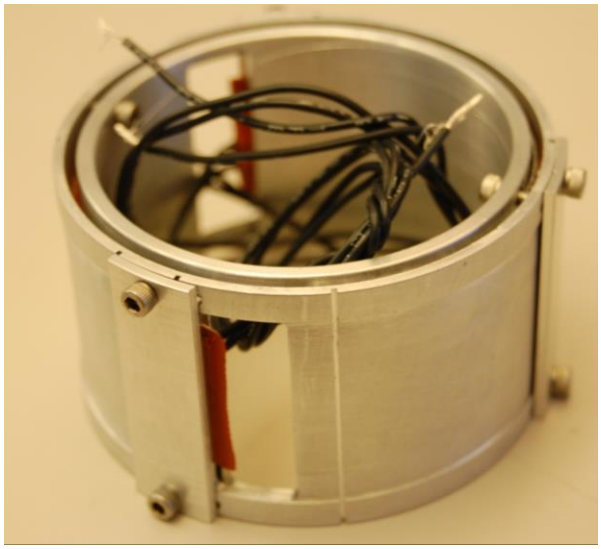

Figure 8.2: The PCR Thermocycler with Flexible Heaters

The final iteration of the thermocycler that was used in this work incorporated flexible heaters with an adhesive backing with which they were attached to the backside of the aluminum blocks, further reducing the thermal mass of the heater. The final heater used in this work was machined out of aluminum as two-parts that are held together using two rings made out of Delrin® at the top and bottom as illustrated in Figure 8.3. The overall heater had an ID of 2.75 inches and an OD of 3 inches with a height of 2 inches. The spacing between the two aluminum blocks of the two temperature zones was fixed to be 0.5 inch to allow for the optical interrogation on one side and to

allow for heat dissipation on the other side as the fluid moves from the hot zone to the cold zone. With this design the arc length of the fluid path in the 60 ºC zone was 5 inches and 3 inches in the 95 ºC zone. As illustrated Figure 8.3, grooves were machined on the surface of the aluminum to embed thermocouples for temperature feedback.

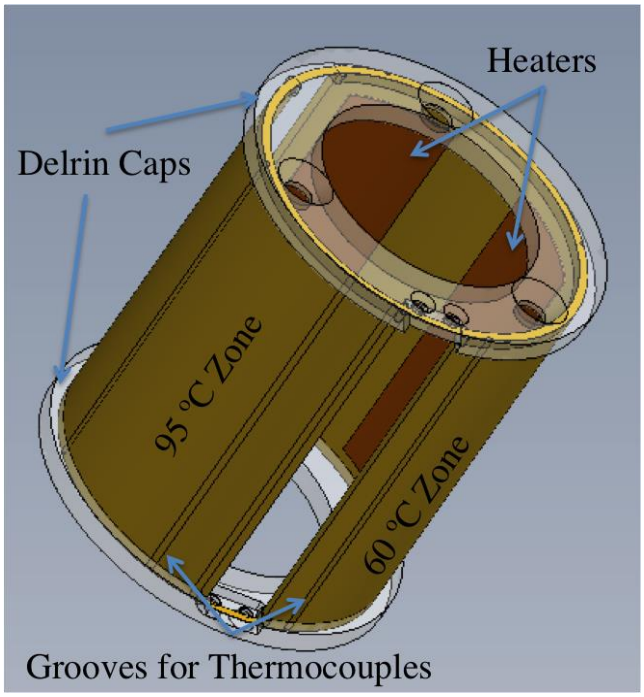

Figure 8.3: Schematic of the Final Heater Design

8.2.2 Electronic Control Circuitry

The CN8200 series temperature controller used in the first thermocycler design performed according to specifications. However, it was quite bulky and consumed a lot of power. Consequently, for portable applications it was not an ideal solution. For this purpose it was imperative to design and develop a temperature controller that would both fit the requirements and consume minimal power. In designing the controller, there are three distinct components that were accounted for. The temperature readout, a microcontroller based control circuitry, and relay-based gating mechanism for on-off control driven by the microcontroller as illustrated in Figure 8.4.

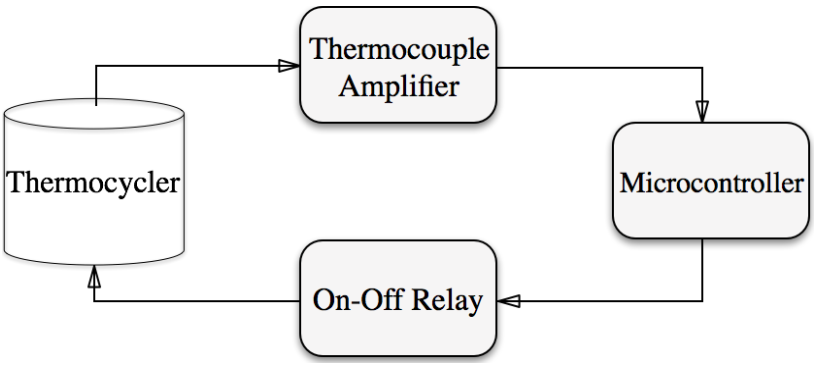

Figure 8.4: Overview of the Heater Control Circuit Components

As illustrated in the figure above, thermocouples were used to sense the temperature from the thermocycler. A thermocouple is essentially two dissimilar metals in contact that generates voltage with changes in temperature. Normally, the two dissimilar metals are fused at a point to provide a stable noise free voltage proportional to the temperature at the junction. A thermocouple is not an absolute measurement tool; it provides the difference of temperatures between two points. The difference in voltage due to temperature is actually a function of the difference in temperature at the junction (which is where the measurement is performed) and a reference junction, ideally held at 0° C or at a known reference temperature, to provide a change in voltage as illustrated in Figure 8.5.

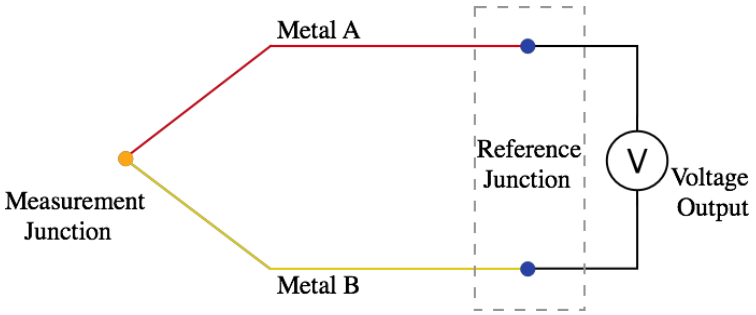

Figure 8.5: Generic Thermocouple Temperature Measurement Setup

However, in a field environment, maintaining 0° C or a known reference temperature is not feasible. Consequently, a technique called "cold junction compensation" is utilized. A thermally sensitive apparatus is used to measure the

temperature at the terminal where the thermocouple interfaces with the circuit, which acts as the reference junction temperature. This is then utilized in the determining the proper voltage to temperature change relation at the measurement junction. Various combinations of Metal A and Metal B are used in the construction of thermocouples with different combinations providing different ranges of voltages for changes in temperature. Normally, the voltage differences obtained because of temperature changes from a thermocouple are normally in the order of a few μV per ^{o}C change in temperature as determined by the Seebeck coefficient, which is quite challenging to detect electrically. Consequently this signal requires to be amplified to levels that can be usefully utilized in a circuit. For this work, K-type thermocouple was chosen owing to them being the most widely available and used of the different thermocouple types. Furthermore, it provides a constant Seebeck coefficient of around 41 μV/^{o}C sensitivity over 0 ^{o}C to 1000 ^{o}C. In case of K-type thermocouple the two metals are actually alloys; chromel (90% nickel and 10% chromium), which is the positive terminal identified by the yellow wire and alumel (95% nickel, 2% manganese, 2% aluminum and 1% silicon), which is the negative terminal identified by the red wire.

A few considerations and design principles were employed in the design of the thermocouple readout circuit. A low pass circuit is recommended in between the thermocouple and the amplifier eliminate radio-frequency interference (RFI) signals owing to the long leads of the thermocouple wires which can act as antennas. The filter was designed to have a low corner frequency such that it still allows fluctuations in the input signal to pass through while blocking the higher frequency noise signals. A general schematic of an RFI filter is shown in Figure 8.6 with the differential input being fed into an instrumentation amplifier. The RC time constants in the two differential input lines needs to be closely matched to ensure no common mode (CM) signals at the input gets

converted to differential mode (DM) signals at the amplifier input. However, precise matching of R1 and R2 and also C1 and C2 is hard to achieve and thus C3 is added to suppress spurious CM-to-DM signal conversion. The value of C3 is normally chosen to be quite high with it generally being at least ten times the value of C1 or C2.

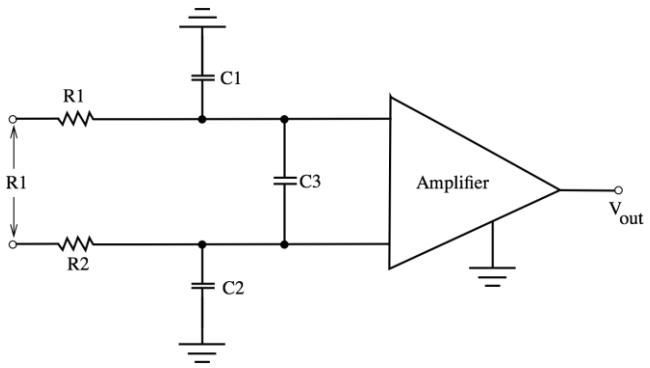

Figure 8.6: General Schematic of a Low Pass CM/DM RFI Filter

The CM filtering is provided by R1-C1 and R2-C2, while the DM filtering is provided by (R1 + R2) and C3 in parallel with the series connection of C1 and C2. From the circuit, the time constants of the differential mode (τ_{DM}) and the common mode (τ_{CM}) are given by Equations 8.1 and 8.2 which leads to the DM and CM filter bandwidths (BW_{DM} and BW_{CM} respectively) using the relationship $1/2\pi RC$.

$$\tau_{DM} = (R1 + R2)\left[\frac{C1.C2}{C1 + C2} + C3\right] \quad \text{Eqn. 8.1}$$

$$\tau_{CM} = R1.C1 = R2.C2 \quad \text{Eqn. 8.2}$$

For R1 = R2 = R and C1 = C2 = C, the bandwidth of the filter circuit thus reduces to

$$BW_{DM} = \frac{1}{2\pi.R(2.C3 + C)} \quad \text{Eqn. 8.3}$$

$$BW_{CM} = \frac{1}{2\pi.R.C} \quad \text{Eqn. 8.4}$$

The values of R1 = R2 = R are chosen to be low so that any input offset currents of the amplifier would not generate voltages comparable to the voltages generated by the

thermocouple thereby introducing noise. Also, it is recommended that the negative terminal of the thermocouple be grounded through a very high value resistor to set the common mode input.

For this work, AD8497 integrated circuit (IC) K-type thermocouple amplifier with in-built cold junction compensation (Analog Devices, MA USA) was used as the interface for the thermocouples. The AD8497 ICs provided a 5 mV/°C signal directly from the thermocouple. The schematic of the circuit using the AD8497 IC is illustrated in Figure 8.7 with a BW_{DM} of 344.5 Hz and a BW_{CM} of ~7 KHz as obtained using Equation 8.3 and Equation 8.4 respectively.

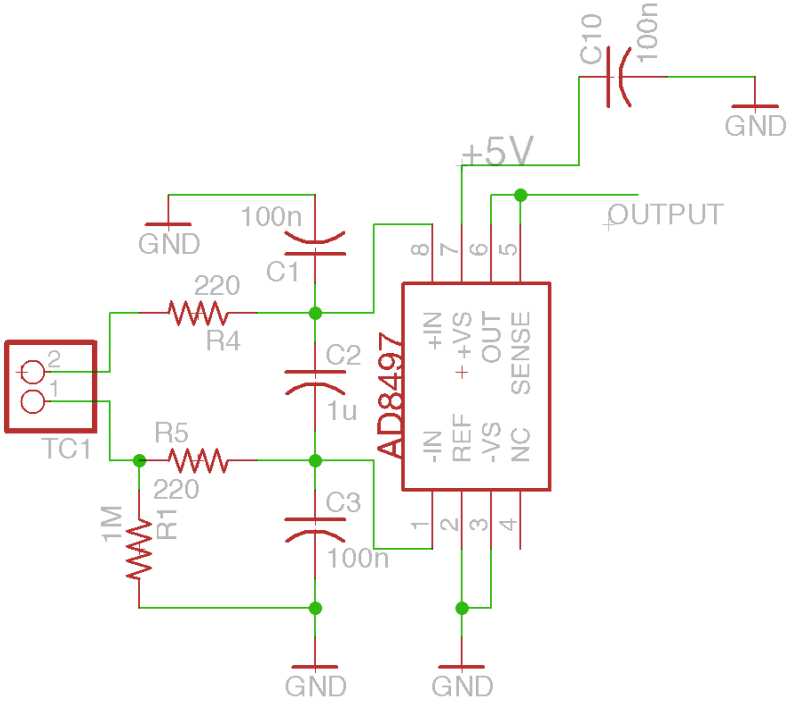

Figure 8.7: Schematic of the Thermocouple Readout Circuit

The voltage obtained at the output of the AD8497 was then read into a microcontroller to compare the temperature with a set value of the temperature. For this work, a low power, low cost microcontroller board, Arduino Uno, was identified as the microcontroller of choice. It is an open source platform with a simple programming

environment using the C++ language. Further it is easily extensible with numerous hardware modules and a wealth of available open source software libraries. Although initial designs were implemented using the Arduino board, once the system was validated, the microcontroller was implemented using just the ATMEGA328 microcontroller chips from Atmel with an application specific design to further reduce the power and size footprint. The temperature control algorithm in this work was thus incorporated on the Arduino platform using the Arduino IDE, which could also be directly ported onto the custom design with the ATMEGA328 chip.

The design of the controller using the scheme illustrated in Figure 8.4 was undertaken as follows. The output of the AD8497 was read using the analog input pin of the Arduino board. The microcontroller has an in-built 10-bit Analog to Digital Converter (ADC) that automatically converts the analog voltage (varying between 0 – 5 V) into digital signal with 1024 levels. This value was used to determine the actual temperature reading (T_{meas}) using the 5 mV/°C slope of the AD8497 IC using Equation 8.5.

$$T_{meas} = \frac{V_{Out} - V_{Ref}}{5} \circ C$$
$$\Rightarrow T_{meas} = \frac{V_{Out}}{5} \circ C, \quad for V_{Ref} = 0 \qquad \text{Eqn. 8.5}$$

Once the actual temperature was determined it was compared with the set temperature for that channel and based on the difference, a pulse-width modulated (PWM) signal was generated which was a function of the difference between the actual temperature and the set temperature. By switching on and off rapidly the control signal between a supply and the load the average value of the voltage or current can be controlled as a function of the actual and set points. The ratio of the on time relative to the period of the signal was defined as the duty-cycle, with a low duty cycle signifying

lower average power supplied to the load from the source and vice versa. The process of pulse width modulation was essentially a process of modulating this duty cycle as a function of the control signal. PWM signals are really well suited for digital control systems because of their on-off nature, by which they can set the required duty-cycle quite easily. This can thus be used as an effective variable power delivery system to a load without the power losses associated with resistive means.

The Arduino PWM output values has a range of 0 – 255 which relates to 0% and 100% duty cycle respectively; 0% signifying no signal and 100% signifying full on. The switch that the PWM signal operates is normally a relay. It is an electronic switching circuit that can be controlled using a microcontroller. In cases where the load requires a higher power, it might lead to overload or fault conditions on the microcontroller. The relay provides isolation between the low power microcontroller signals and the higher power load signals while providing the switching functionality at the same time. The most basic implementation of a relay uses an electromagnet to operate a mechanical switch. However, these are limited in reliability by the number of switching cycles that they can go through. For a control circuit as was implemented here, a mechanical relay thus is not an optimum choice. Furthermore, they are generally quite bulky and consume a lot of power that is necessary to energize the electromagnet. Solid state relays (SSR) on the other hand has no moving parts while providing the same functionality in a much smaller package and with much lower power draw. In general, SSRs make use of a Light Emitting Diode (LED) which when turned on lights up a photosensitive diode. The diode current generated because of this action then turns on a metal–oxide–semiconductor field-effect transistor (MOSFET) to switch on the load. Because of the lack of physical connection between the control and the load side, they are rated for very high isolation

voltages in a small package. The lack of moving parts also makes them quite reliable over long periods of time.

For this work, G3VM-61HR (Omron Electronics), solid state MOSFET relay with the capability to handle high currents (up to 2.3 A), was identified as the optimum solution. Because of the presence of the LED on the control side, the LED forward voltage (V_F) and the optimum LED forward current (I_F) were factored in while designing the circuit. In order to limit the LED current; a resistor needs to be connected in series (R_S), the value of which can be estimated from Equation 8.6.

$$R_s = \frac{V_{cc} - V_F}{I_F} \qquad \text{Eqn. 8.6}$$

Thus for V_{cc} of 5 V, and using the recommended values of V_F = 1.33 V and I_F = 7.5 mA from the datasheet, the value of R_S can be calculated from Equation 8.6 to be 489.3 Ω. Thus, the closest available standard resister value of 487 Ω was chosen for the circuit as illustrated in the schematic in Figure 8.8. The output of the relay was connected to the heater terminals. G3VM-61HR is a normally closed (NC) type relay and so the heater circuit is completed only when a high signal is provided at the input terminals to the relay.

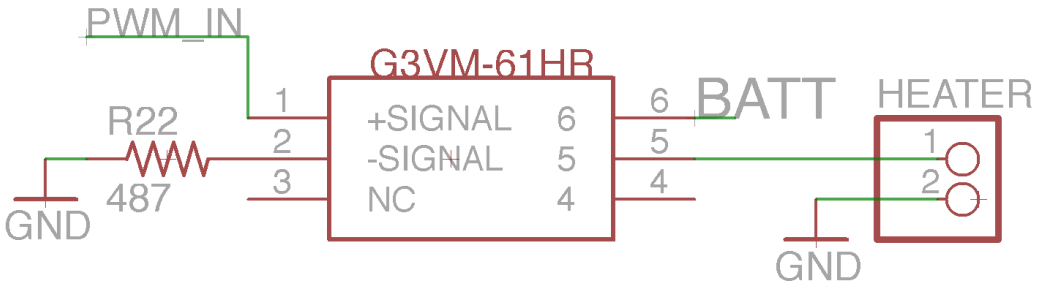

Figure 8.8: Schematic of the Relay Circuit

In its very simple form, a control circuit ensures that the relay is turned on when the temperature of the system is lower than the set temperature and is closed when the temperature is higher. However, this causes issues in terms of overshooting of the set

temperature. Consequently, selection of a control algorithm that can effectively utilize the 255 levels of the PWM signal was critical. Proportional Integral Derivative or PID controllers are known to be really effective in case of thermal systems. The PID controller attempts to regulate the PWM signal by taking into account the past, current and predicted future errors. Mathematically, the constants of the three elements, proportional constant (K_P), integral constant (K_I) and derivative constant (K_D) in conjunction with the error *E(t)* at time *t*, provides the correction factor *C(t)* to the system at time *t* according to Equation 8.7.

$$C(t) = K_P * E(t) + K_I \int_0^t E(t)dt + K_D \frac{dE(t)}{dt} \qquad \text{Eqn. 8.7}$$

The proportional control takes into account the current error and responds accordingly to the amount of the error. If used alone, proportional control tends to overshoot the set point and leads to oscillations in the system. A higher value of K_P leads to a faster rise time but also leads to more pronounced oscillations and overshoot. However, with proper tuning along with the other control parameters it can provide fast rise times with minimal overshoot and oscillations.

The component responsible for reducing the overshoot of the system is the derivative control. It provides a damping affect to the system in the event of rapid transient changes of temperature of the system. It takes into account the slope of the error, which acts as a predictor of the future value of the error, and thus helps in minimizing the effects of transient changes. However, in case of noisy environments, the derivative control sometimes leads to large fluctuations in the output and thus the value of the derivative constant was kept really small in the program.

The integral control is responsible for attaining an average error of zero. It is responsible for the minimizing the steady state error conditions. It sums up all the past errors and tries to maintain an overall error of zero.

In this work, the PID control was implemented using an open source PID library available for the Arduino platform albeit with some modifications. In order to achieve a rapid rise time of the temperatures, the PID control was suspended until the temperature of the system reaches within 5 ºC of the set temperature at which point the PID control was activated. During the rapid rise phase, the PWM was driven at 100% duty cycle to achieve a faster temperature rise.

Once the system was validated using the Arduino board, the circuit was designed using the ATMEGA328 microcontroller chip. The circuit was initially designed as two modules, the first module containing the ATMEGA328 breakout circuit and the second module containing the heater control circuit. Eventually, these two modules was integrated on a single PCB. Figure 8.9 shows the schematic of the ATMEGA328 breakout circuit adapted from the open source SMDuino layout [122]. Figure 8.10 shows the schematic of the heater control circuitry.

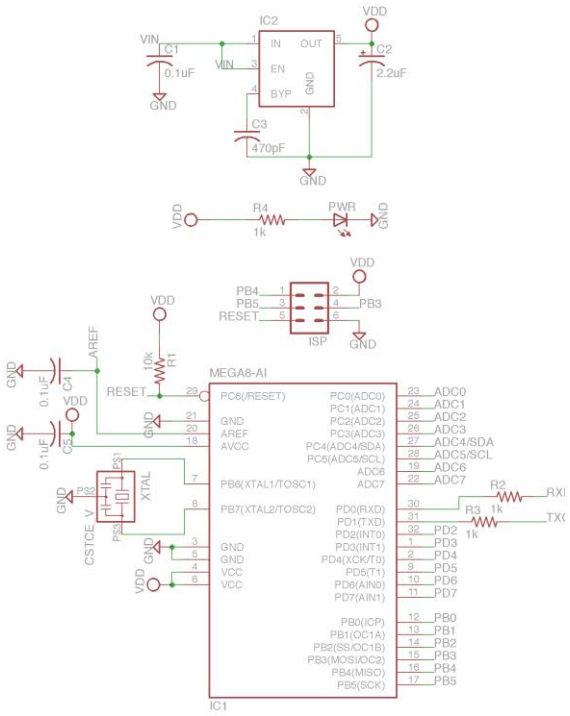

Figure 8.9: ATMEGA328 Breakout Circuit Schematic

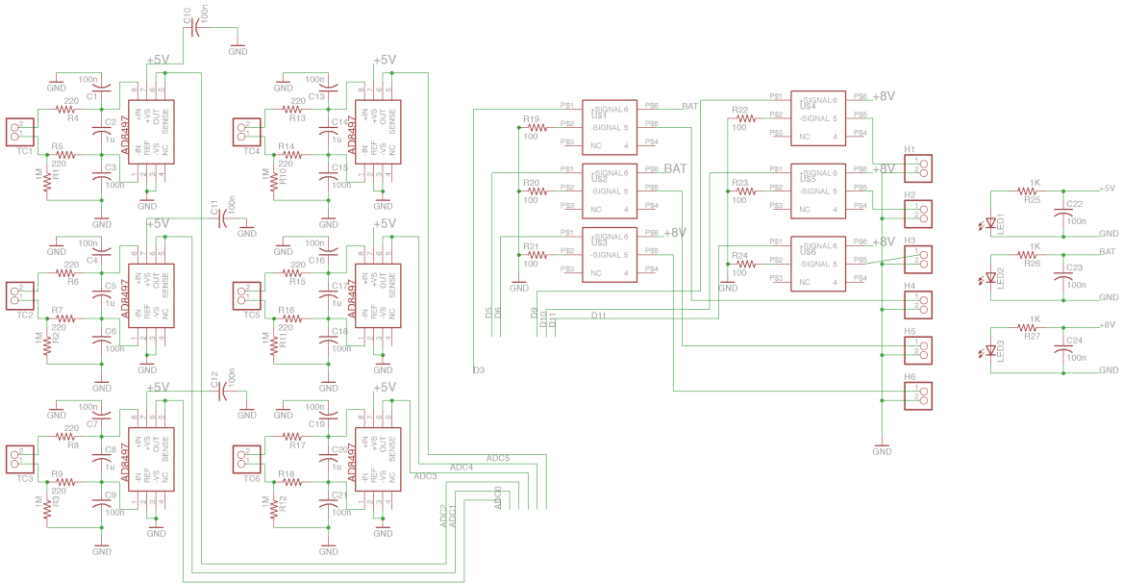

Figure 8.10: Schematic of the Heater Control Circuit

8.3 Results and Discussion

The first iteration of the heaters using the Nichrome heaters were used to perform an initial analysis of the feasibility of the cylindrical thermocycler design. Temperature measurements were taken both underneath (touching the metal) and on the outside of the capillary tubing to get a sense of the thermal gradient over the diameter of the tubing. A difference of about 2.5 ºC was observed between the inside and outside the tubing in case of the 60º C zone and about 7.5 ºC in case of the 95º C zone without any fluid flow. With fluid flow the difference was found to be even greater. Non-uniformities in the temperature profile was observed even on the surface of the two heating zones with a variation of about 4º C observed in case of the 60 ºC zone and a variation of about 8º C observed in case of the 95º C zone. These observations could be attributed to two causes. Firstly, a lot of the non-uniformity specially the variation between the inside and the outside surface of the tubing could be attributed to a lack of proper insulation. And secondly, the use of the Nichrome heating wires in only a specific point of the entire

heater was not able to maintain a steady temperature over the entire metal block especially when the liquid was flowing.

A series of COMSOL® simulations were performed to determine the importance of the either insulation or dual side heating to mitigate this huge temperature gradient. Although the best results were obtained with heating from both sides, acceptable results were obtained with insulation as well. Figure 8.11 shows a simulation of the transition from the 60° C side to the 95° C side. As is clearly seen, without insulation, the entire tubing doesn't reach the set temperature at all, but does when properly insulated. Similar results can be seen in case of transition from the 95° C side to 60° C side. It was decided to proceed with adequate insulation, as dual side heating would have required a much higher power budget.

Another aspect that was looked into was the time it took for the fluid to attain the temperature change as it transitioned from one zone to the next. From the COMSOL® simulations (Figure 8.11) as well as infrared imaging as illustrated in Figure 8.12, it was found that the transition time for the fluid to attain a the higher or lower temperature was pretty small. This can be attributed to the fact that the tubing and the heaters are all maintained at a specific temperature and the fluid was the only component traversing through the temperature zones. Consequently, the heat exchange was found to take place pretty rapidly.

Based on the results of the COMSOL® simulations, the cylindrical heater used in this work was thus enclosed in 0.5 inch thick low-density foam on the outside as well as inside for insulation to reduce power consumption.

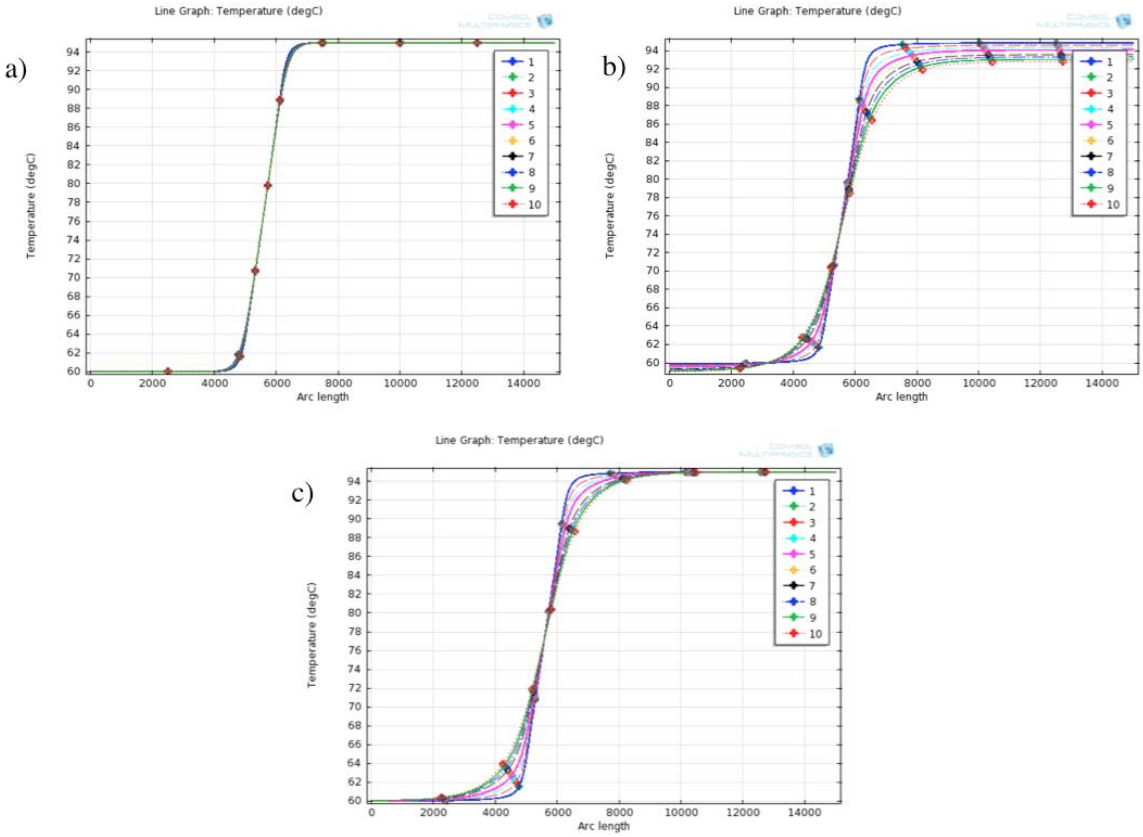

Figure 8.11: Temperature Profile of Capillary Cross-section from 60° C to 95° C Transition when a) Heated from Both Sides b) Heated from One Side with Other Side Exposed to Ambient, and c) Heated from One Side with the Other Side Insulated

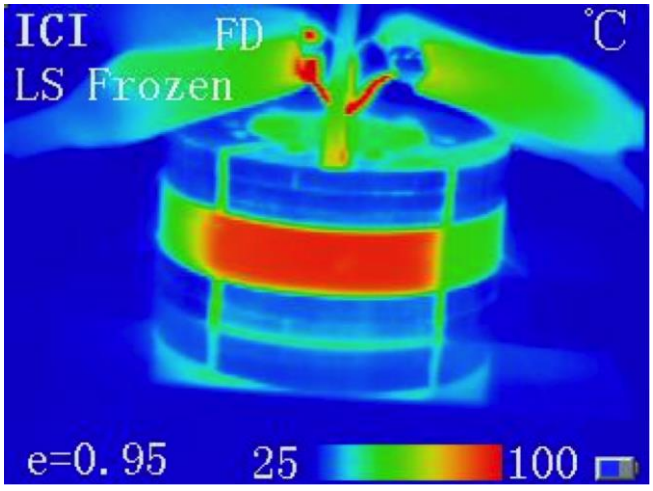

Figure 8.12: Infrared Image of Fluid Flowing Across the Different Temperature Zones of the Thermocycler Showing Minimal Thermal Carryover

One of the primary considerations of this work was to explore avenues to reduce the overall power consumption and to ensure that the power draw of the system is within the specified design constraints. Since the heaters are the most significant source of power draw, care was taken so as to minimize the total draw as well as limit the total current draw of the system. In order for that, the flexible Kapton® heaters were analyzed to determine the optimum voltage at which they can be driven so that the current draw was within acceptable values. Since the voltage values that the system needs to operated with could be anywhere between 10 – 18 V, the KHLV heaters were evaluated at three voltage levels, 8 V, 12 V and 18V with the results shown in Table 8.1 for the two types of heaters. The size of the heater based on the design of the thermocycler was chosen as 1 inches by 3 inches although the active areas of the heater didn't scale proportionately.

Table 8.1: Characteristics of the KHLV Heaters

Heater Power Density	Voltage (V)	Resistance (Ω)	Current Draw (mA)	Power (W)
10 W/in²	18	27.3	660	11.88
	12		440	5.28
	8		290	2.32
5 W/in²	18	50	360	6.48
	12		240	2.88
	8		160	1.28

The heater was designed to take 8 of the 1-inch by 3 inches heaters. From the results shown in Table 8.1, it is clear that using only the 5 W/in² heaters at 12 V, the total peak current draw can be kept under 2 A, however it takes up all of the current budget for the system. The 5 W/in² heaters even at 12 V were also found to be lacking in maintaining the set temperature as the liquid was flowing through the thermocycler. The 95 °C zone took a really long time it achieving the set temperature at 8V from room

temperature. Consequently, a design effort was undertaken to accommodate all the heaters with as low of a current draw as possible with a reasonable warm up time. 8 V was chosen as the voltage to all of the heaters because in order to account for the input voltage swing from 10 – 18 V, stepping down to 8 V was the most efficient in terms of power conversion. Anything lower than 8 V was found to be inadequate for the heaters. However, the 5 W/in² at 8 V was found to be inadequate as the first 95 ºC heater when the 60 ºC comes in and needs to be rapidly heated up to the denaturation temperature and thus requires the most power during the PCR operation. Consequently, this heater was chosen with a power density of 10 W/in² and connected directly to the battery to minimize power loss due to voltage conversion. Furthermore, the cylindrical heater was segmented into 4 heat zones as illustrated in Figure 8.13.

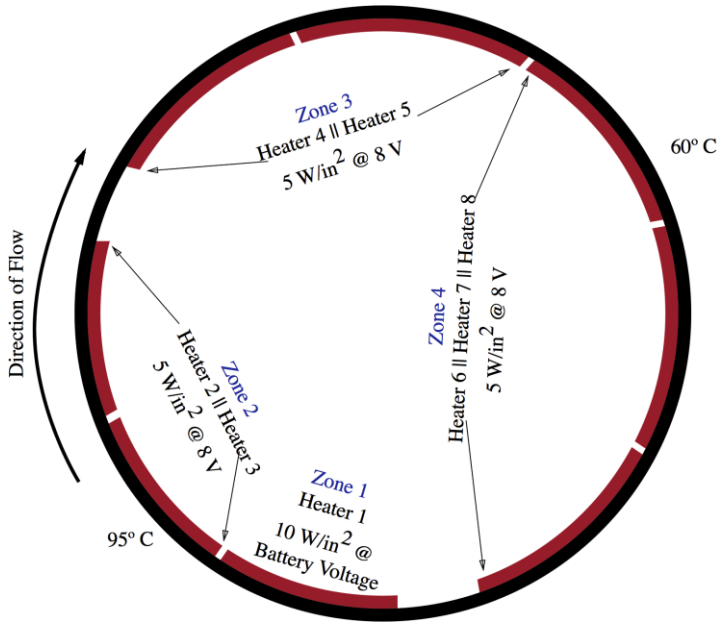

Figure 8.13: Layout of the Heating Zones and the Heaters of the Thermocycler

The first heating zone of the 95º C side, which requires the most power in order to heat up the incoming liquid from 60 ºC, and the second heating zone of the hot side to maintain the temperature at 95º C. The third heating zone, which was the first zone of the 60º C side, that would require minimal power during the PCR run as the 95 ºC fluid

comes in through this zone and dissipates heat as it cools down to 60° C; and the fourth heating zone to maintain the fluid temperature at 60 °C. The heaters in the 2nd, 3rd, and 4th zones were also connected in parallel so that they can cover the entire heating zone but also at the same time their total power draw could be limited. With this configuration, the current and power maximum power draw for the entire thermocycler when all of them are full on are summarized in Table 8.2.

Thus, even at 18 V, the peak current draw is still lower than 2 A, and at 18 V the heater attains its set temperature fairly quickly (<10 mins) after which the peak power draw falls considerably. At 12 volts, the hot zones were found to take about 20 minutes to come up to temperature, while the entire thermocycler comes up to temperature in about 30 minutes. After that, in order to maintain the temperature with liquid flowing at the PCR experiment rate of 47 μL/min, with proper insulation, it was found that it required just about 5 W.

Table 8.2: Peak Current and Power Draw of the Real-time Thermocycler

Heating Zone	Current	Power
Zone 1	0.66 A @ 18 V 0.37 A @ 10 V	11.88 W @ 18 V 3.67 W @ 10 V
Zone 2	0.32 A	2.56 W
Zone 3	0.48 A	3.84 W
Zone 4	0.32 A	2.56 W
Total	1.78 A Max / 1.49 A Min	20.84 W Max / 12.63 W Min

In order to step down the voltage to a constant 8 V from the battery voltage of 10 – 18 V, a high efficiency step down integrated switching buck regulator (PTN78060W from TI Instruments) was used that had a voltage conversion efficiency > 90%.

The use of the Arduino based PID code as discussed earlier was found to be very effective in monitoring and controlling the temperature profile of the thermocycler. The PWM frequency of the ATMEGA328 microcontroller was set to 30 Hz to allow for the heaters enough time to properly respond to the changes in control. Slight modification of the temperature calculation equation (Equation 8.5) was necessitated due to non-linearity of the AD8497 output and was accounted for in the code.

8.4 CONCLUSIONS

The design and development of the PCR thermocycler module and its associated control circuitry had to undergo quite a bit of design iterations. Issues with regards to power and thermal uniformity of the thermocycler were dealt with in the final design that was optimized to address all of those issues. Being able to attain a 5 W continuous power draw during the operation of the PCR experiment allows this thermocycler module design to be used for portable PCR application. Considering the input voltage at 18 V, the total thermocycler takes less than 25 Watt-hours for a 30-minute warm-up and a 1-hour PCR run which is quite feasible for field operations off of a battery.

Because of the continuous nature of this design it provides a high-throughput platform than can in theory be run continuously with new reagents being loaded successively using the fluid manifold described in the previous chapter. Additionally, different reagent volumes can be quite easily accommodated as long as they don't occupy more than the volume of a single wrap of the tubing over the 95 ^{o}C zone. For this design thus the maximum volume of a single reaction chamber that can be accommodated would be about 15 μL with the lower limit being around 65 nL, which was the smallest volume that would cover the entire diameter of the tubing.

CHAPTER 9

DESIGN AND DEVELOPMENT OF THE OPTICAL MODULE

9.1 INTRODUCTION

Cylindrical PCR thermocyclers for DNA amplification have been reported before [96], [123], [124]. However, these devices have primarily been used for the amplification of gene products and in case of detection after amplification they have been done using gel electrophoresis techniques after collecting the amplified product. Real time detection of the PCR products, as they are amplifying to provide a true real-time PCR data that can be used or quantification have so far not been quite explored. In this work, in order to achieve quantitative PCR, the design and development of an optical detection mechanism based on fluorescence signals was undertaken.

9.2 MATERIALS AND METHODS

One of the challenges in the design of a real time detection mechanism for a continuous flow system as is explained here is the distribution and collection of excitation and fluorescence signals from each of the PCR cycles. Various approaches were evaluated in order to achieve a uniform illumination of the individual wraps of tubing carrying the PCR products around the thermocycler. Since the entire thermocycler was wrapped in insulating material the design effort also involved figuring out the optimal coupling mechanism of the optical excitation and detection with the thermocycler.

The fluorescent dye for the Taq polymerase used in this work was Fluorescein amidite (FAM) that is commercially available as 6-FAM™. It is one of the most commonly used dyes used in molecular biology for attachment to oligonucleotides. For optimum fluorescence it is used in solutions with a pH range of 7.5 – 8.5. In pH conditions lower than 7, this dye becomes protonated thereby leading to decreased fluorescence activity. This dye is excited at around 475 nm (excitation wavelength), with

an emission spectra of around 540 nm (emission wavelength). The optical setup in this work was thus designed to work with those wavelengths.

Lasers have the ability to provide light sources with specific wavelengths with a narrow bandwidth spread thereby eliminating the need for filters. However, they are not always the best solution when designing low power systems. Consequently, for this work a broadband LED source was identified as the light source. A 470-nm mounted high-power LED (M470L2, Thorlabs, USA) was selected as the light source with 950 mW of typical output optical power. The LED has a forward voltage of 3.5 V with a peak current draw of 1.6 A, and mounted on a heat sink for optimum performance. The nominal wavelength of the LED as specified by the manufacturer is 470 nm with a bandwidth of around 450 – 475 nm at 50% normalized intensity. In this work, the LED was driven using a T-Cube LED driver (LEDD1B, Thorlabs, USA) that can provide a maximum of 1.2 A of drive current for the LED.

In order to clean up the light source a single-band 475/50 nm BrightLine® band pass excitation filter (FF02-475/50-25, Semrock USA) was used at the output of the LED. This filter has a center wavelength of 475 nm with a bandwidth of 50 nm with a transmission efficiency > 95% in the pass band. This interference or dichroic filter was used to allow only the excitation wavelengths for 6-FAM™ while blocking out all the other wavelengths from the broad spread of wavelength from the LED source.

Similarly, on the detector side, a similar filter was used to collect only the emission wavelength while rejecting all the other wavelengths. A single-band 540/50 nm BrightLine® band pass interference excitation filter (FF01-540/50, Semrock USA) was used for this purpose. This filter has a center wavelength of 540 nm with a bandwidth of 50 nm with a transmission efficiency > 98% in the pass band.

In order to provide excitation illumination to the individual wraps of the PCR tubing, optical fibers were determined to be the optimum solution for this system. The use of optical fibers enables the focusing of the excitation light right on the tubing face. This also eliminates noise from background light sources, as the optical fiber can be close coupled to the FEP tubing wrapped around the thermocycler. The emission from the 6-FAM™ dye can also be collected using optical fibers in the same way from a narrow conical region. The numerical aperture (NA) of the optical fiber determines the acceptance angle of the light incident on the fiber. Since optical fibers have a finite NA, they can thus accept light only from a certain area. This helps in gathering only the intended signal from a close-coupled system. The NA of an optical fiber is dependent on the refractive index difference between the core and the cladding of the fiber. For this work, high-OH silica optical fibers (Polymicro Technologies, USA) with a 400-µm core diameter and 0.22 NA was used. A 0.22 NA optical fiber has an equivalent acceptance angle of 25°. The high-OH optical fiber was chosen as it has the best performance in the ultra-violet/visible wavelength range owing to their low absorption in this range.

Identification of the optimal coupling scheme between the excitation and collection optical fibers and the FEP tubing was performed as part of this work. The challenges that were worked out involved achieving a scheme with high signal levels and signal-to-noise ratio with the least amount of cross talk. An initial scheme was evaluated in which the excitation and emission fibers were coupled head-on on either side of the FEP tubing. However, although this provided to high signal levels, the signal-to-noise levels obtained were very poor. This was because of the bleeding of the excitation light onto the detector through the filters. An alternate scheme in which the excitation and emission fibers were coupled at an angle of 30° to the normal was found to provide high signals levels with a high signal-to-noise ratio. In order to couple the fibers onto multiple

wraps of tubing around the thermocycler, an aluminum housing was designed to accommodate the close coupling of the three as illustrated in Figure 9.1. Each of the optical fibers was inserted into the respective openings. To further increase the optical coupling, optical gel was used at the tip of each of the optical fibers as they were inserted into the optical manifold. This helped reduce variations in the optical coupling efficiencies and increase overall signal-to-noise ratios.

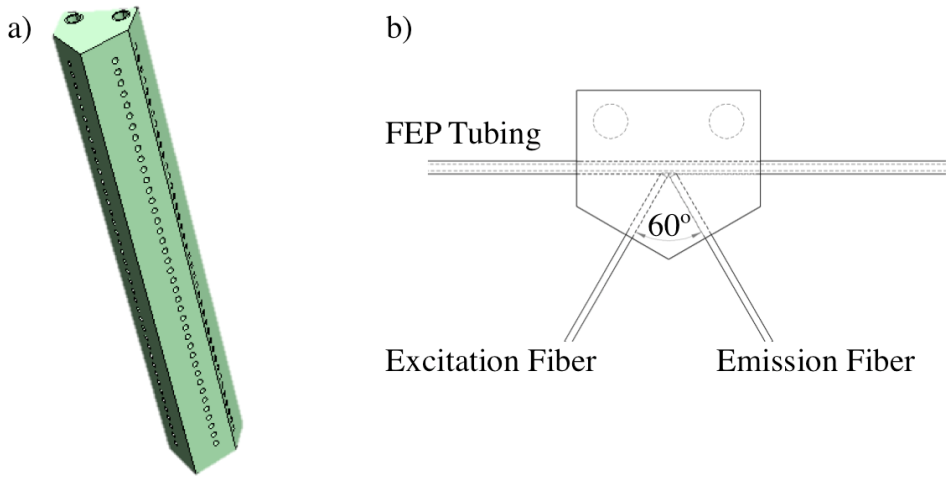

Figure 9.1: Schematic of the a) Complete Optical Manifold and b) a Cross-section Showing the Relative Alignments of the Optical Fibers and the FEP Tubing

In order to launch the excitation light from the LED onto each of the optical fibers uniformly an optical fiber launch was used in this work. An optical fiber launch was custom fabricated by Polymicro Technologies in a closed pack fashion in order to attain maximum filling of the fiber bundle face with the excitation light. The optical fiber bundle was assembled in a 3/16th inch ID and 0.5 inch OD aluminum housing with a strain relief. Each of the 37 optical fibers had a core diameter of 400 µm and a length of 0.5 meters with 0.5 inches of the polyimide coating stripped from both ends. The number of fibers was chosen to be 37 as this provided a closed pack structure inside the fiber launch. In order to further focus the light onto the face of the fiber bindle, a 1-inch aspheric condenser lens (ACL 250, Thorlabs, USA) was used. The optical intensity at the

output of each excitation fiber was measured using an optical power meter kit (PM130D, Thorlabs, USA) to determine their uniformity.

The fluorescence emission from the reporter dyes in the PCR was collected by the emission fibers. The light coming out of the fibers at the detector would normally diverge. Consequently, in order to enhance the signal, the output of each fiber was collimated using 3 mm ball lenses as illustrated in Figure 9.2a. The emission signal was passed through the green interference filter mentioned earlier followed by a glass absorption filter (FSQOG515, Newport, USA). The absorption filter acts as a long pass filter that allows light with wavelength greater than 515 nm to pass through while blocking lower wavelength lights. This filter was used to further improve the signal-to-noise ratio by cutting out the overlapping portion of the excitation light that might be collected by the emission fiber.

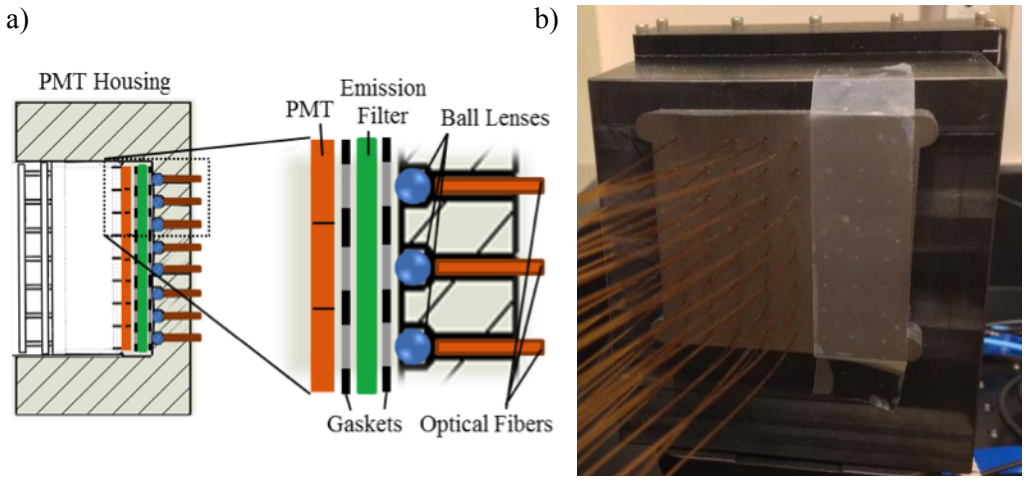

Figure 9.2: a) Schematic of the Detection Block Showing Optical Fibers Interfacing with the PMT Face and b) The PMT Housing Shown with the Fibers

The emission fiber was then coupled with a 64-channel multi-anode PMT in a 8 x 8 configuration (H8500, Hamamatsu Photonics, USA) for the emission signal detection. This 64-channel PMT had a common glass plate at the detector face; as a result rubber gaskets were fabricated to limit the cross-talk between adjacent channels.

Figure 9.2b shows the custom housing that was designed to house the PMT and the filters with the optical fibers.

The 64-channel PMT was interfaced with an interface board (SIB064A, Vertilon, USA) that contained the readout circuitry and the amplifiers necessary to read the signals from the PMT. The interface board was connected to a computer using a PhotonIQ IQSP482 DAQ system (Vertilon, USA) for data acquisition. The data acquisition system had graphical user interface (GUI) that enabled control over the PMT and allowed us control over various parameters like the voltage gain setting of the PMT, the capture rate, integration time and background subtraction. Because of the variability of the PMT fabrication process, the PMT came with a data sheet containing the recommended gain settings for each of the 64 channels to obtain uniform signal outputs that were manually entered through the GUI interface. The data acquisition system was also responsible for providing power to the PMT module and was rated for operation at 5 V with a maximum current draw of 2 A. Because 37 optical fibers were used for detection, only 37 of the PMT channels were used for detecting the fluorescence intensities from 37 of the PCR cycles.

For this work, the PMT was operated at a high voltage gain setting of 400 V and an integration time of 2.5 milliseconds. The fluorescence signals were collected at frequencies of 30 – 120 Hz depending on the size of the emulsions with higher frequencies used for smaller emulsion sizes. In order to reduce the power consumption of the LED, instead of running it constantly it was pulsed synchronously with the capture rate through TTL control signals from the Vertilon DAQ board to the LED power driver. The control signal was synchronized such that the LED turned on slightly before the PMT data capture, equal to the LED turn on time, so that the light source reaches its full intensity by the time of the data capture.

To evaluate the optical properties of the system a solution with constant fluorescence intensity was run through the thermocycler at temperature and the data captured and analyzed using the parameters given above. Since the fluorescence intensity is a function of temperature, the thermocycler was maintained at the PCR temperatures during this test. A standard solution of 200 nanomolar (nM) concentration of Fluorescein in 0.1 M pH 8.0 Tris HCL was used for this analysis. For the data analysis, a suite of MATLAB® scripts were written that analyzed the data obtained from the Vertilon board and provided the collated signal intensities from each of the channels. The scripts were coded with automated peak detection algorithms and droplet tracking based on sequential order to calculate and plot the total intensity. The algorithm was designed to be robust enough to account for emulsion breakup and coalescence as well as air bubbles. The size of the emulsions generated was tuned as well so that they are at least the size of the tubing so that the sequence of the emulsions are maintained throughout the tubing without overtaking. Figure 9.3a and 9.3b shows a schematic and picture of the final assembly of the cylindrical thermocycler respectively.

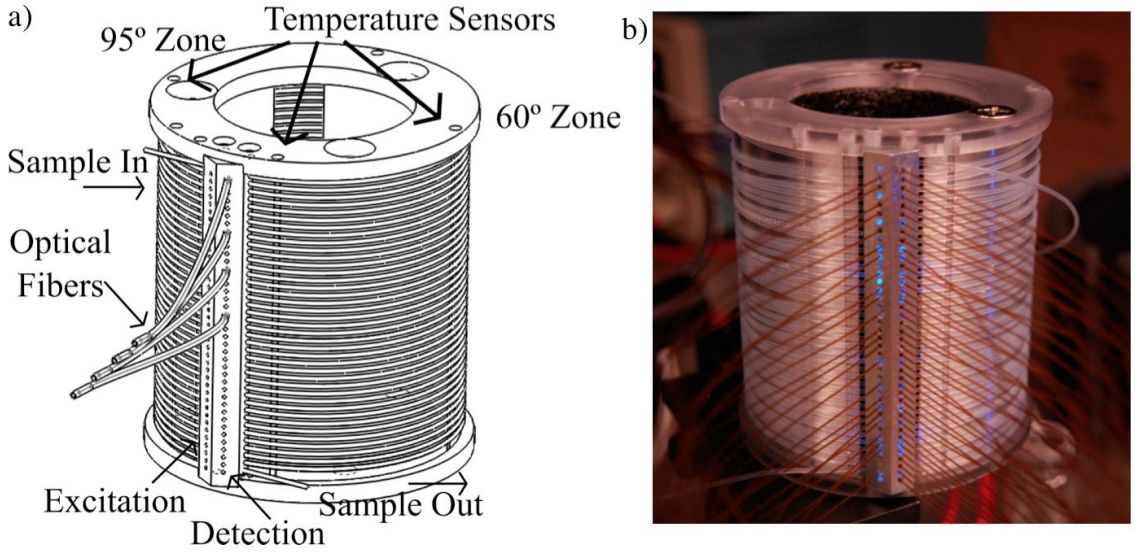

Figure 9.3: a) Schematic of the Complete Thermocycler Showing the Optical Manifold, and b) A Picture of the Developed Thermocycler

9.3 RESULTS AND DISCUSSION

The optical intensities of the light coming out of each of the fibers were measured using the optical power meter setup for a wavelength of 475 nm. The maximum intensity recorded was 800 μW, while the minimum recorded intensity was 540 μW. The coefficient of variation (CV) of the intensities across the 37 fibers was calculated to be about 11%.

The optical setup was evaluated in ambient light as well as in a dark room, and although the background noise level in case of bright environment was slightly higher, it was within acceptable limits. Furthermore, the background subtraction and the normalization process that was followed ensured that the system could function in bright environments. However, because the background subtraction algorithm only considered the ambient levels at the start of the experiment, a change in the ambient lighting conditions led to weird noise patterns. So, for this work all the experiments were performed under steady and controlled ambient lighting conditions.

A higher data capture rate provided us with more data points. But the reconstruction of the signal from the data captured at 30 Hz and 120 Hz was found to be quite similar. The higher capture rate increased the size of the dataset which led to longer processing times. Consequently, for this work, a capture rate of 30 Hz was deemed to be adequate.

Because the number of cycles designed for this PCR instrument was 40, but only had 37 available optical excitation sources, only 37 of the PCR cycles were recorded. The first channel was recorded to determine the start of the experiment, after that the next three channels were skipped because no amplification was expected to happen in those cycles. The rest of the excitation sources were coupled to the tubes corresponding to cycles 5 – 40.

Although care was taken to achieve uniformity of the excitation light across all the optical fibers, non-uniformities in the excitation light at the output of the fibers were nonetheless observed. Furthermore, the coupling efficiencies inside the optical manifold were also not uniform both on the excitation side and the detection side. In order to reduce the variability thus the fluorescein solution was flowed through the thermocycler and its intensities recorded. The concentration of 200 nM was chosen as it was found to be of around the same intensity as an amplified PCR product with the reagents used in this work. The raw signal output for the 200 nM fluorescein solution is shown in Figure 9.4. As is clearly evident from the figure, even though all the signal levels are supposed to be the same, a lot of variability was observed which can be attributed to non-uniformity of coupling efficiencies and the PMT response and variation in the incident excitation through the optical fiber.

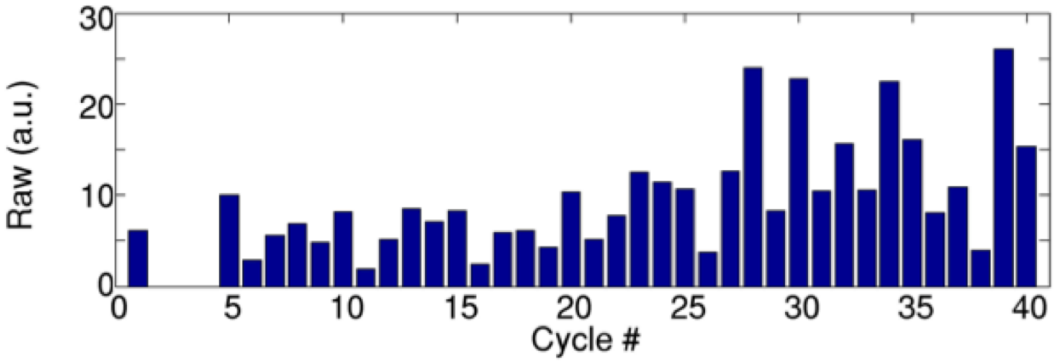

Figure 9.4: Raw Signal Output Levels of 200 nM Fluorescein Solution

9.4 CONCLUSIONS

The design and development of the optical detection scheme was thus presented in this chapter. The challenges associated with real time data collection from a continuous flow PCR system was addressed and the solutions provided. The integration of the optical manifold with the thermocycler design was a novel design effort that not only helped in achieving real time PCR, but also provides a framework for robust

operation that can be used for field operations. Using the synchronization from the Vertilon board to pulse the LED, the power consumption of the LED was maintained at <1 W while the Vertilon board drew a maximum of 10 W of power.

Although in this work, the Vertilon board was used as an interface with the data collection performed using a computer, further reduction in both size and power could be easily achieved. Vertilon also provides an OEM board that can be interfaced with an embedded microcontroller based system for the recording and analysis of the captured data. Furthermore, the design presented here makes use of a 64-channel PMT, although only 37 of those channels are used. It was determined that few more channels for data collection could be skipped bringing the number to 32 without much loss in functionality. A 32-channel PMT can then be used which would greatly reduce the power requirement and the data analysis necessary thereby making this system a viable device for portable applications. Although the use of long lengths of optical fibers can make the system sensitive to hard bumps and vibrations, with proper embedding of the fibers between the light source and the thermocycler can make them more robust. Additionally, a baseline run with a known fluorescence sample to determine the baseline response levels like what is shown in Figure 9.4 before any experimental run can be used to normalize the experimental data against any coupling variation or lighting variation to provide useful PCR results.

CHAPTER 10

EVALUATION OF THE REAL-TIME PCR INSTRUMENT

10.1 INTRODUCTION

The design and development of the essential blocks as specified in the system architecture illustrated in Figure 6.2 was explained in the previous chapters. The integration of these three blocks however was necessary for the development of a complete portable and deployable instrument.

This chapter thus deals with the integration of all the functional modules as well as the evaluation of the developed instrument with actual environmental samples. The efficiency of the instrument was evaluated and the results compared against standard bench-top instruments.

10.2 MATERIALS AND METHODS

Although an overview of the system architecture was provided in Figure 6.2, a more detailed illustration of the instrument is provided in Figure 10.1 showing all the components in the device.

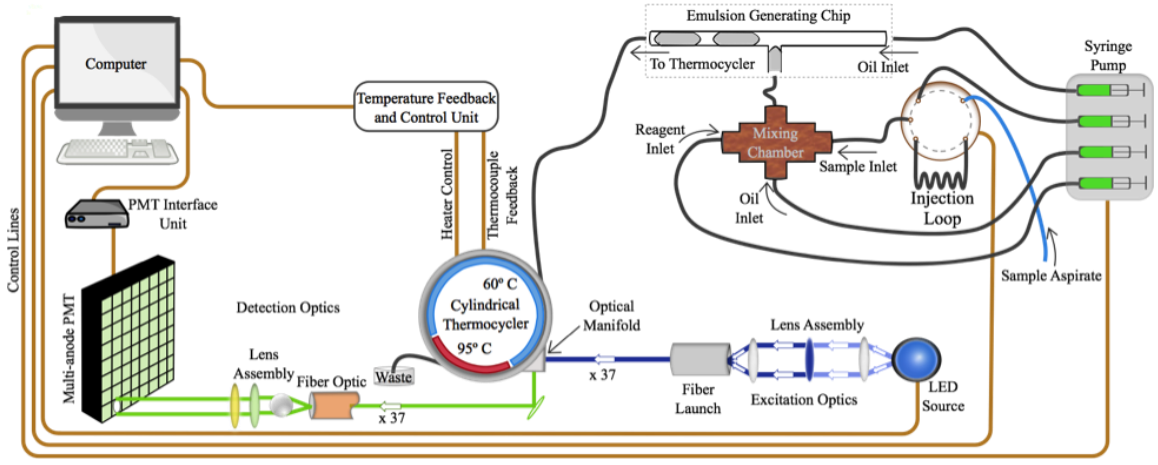

Figure 10.1: System Level Schematic of the qPCR Instrument

All the components of this system was controlled using a central computer / laptop to synchronize their operations as well as to provide flexibility of operation. The

process running an experiment starts with the warm up of the heaters. Once the heaters attain the set temperatures, the DNA sample would be aspirated and mixed with the reagents before generating emulsion droplets via the emulsion generating chip. For this work however, in order to focus on the individual system components of the actual PCR device, the DNA solution was premixed with the reagents and loaded onto the emulsion generating chip to generate W/O emulsions with the help of a bank of syringe pumps (neMESYS, cetoni GmbH, Germany). Flow profiles on multiple syringes can be controlled quite easily with the accompanying GUI software for this syringe pump. The PCR reagents were pushed through at a rate of 47 μL/min for a 1-minute PCR cycle. The ATMEGA328 based temperature controller maintains the thermal profile of the thermocycler. The Vertilon interface board was used to synchronize the LED light source and the PMT capture to record the intensities continuously from the 37 channels as has been explained in the previous chapter.

The evaluation of the instrument was performed primarily with a couple of environmental genes *viz.* cbbL (a photosynthetic gene) and SAR11 (associated with marine carbon cycle). Custom Taqman® hydrolysis probes (5' FAM and 3' MGB/NFQ) and primers (Applied Biosystems, USA) for these genes were obtained along with environmental samples derived from seawater provided by MBARI. All reactions were run at final concentration of 1x Taqman Universal PCR Mastermix with AmpliTaq® gold, a hot start polymerase (Applied Biosystems, USA), 0.175 μM/μL of recombinant Taq DNA polymerase (Fermentas, Canada), and 900 nM each forward and reverse primer and 250 nM hydrolysis probe. Addition of the recombinant Taq DNA polymerase allowed cycling without an initial hot start lag time.

Various starting concentrations of DNA were evaluated using this instrument. Each of the reagents were divided up into two parts with one part being run though the

developed instrument and the other part run in an Applied Biosystems® StepOne™ PCR bench-top instrument. No template controls (NTCs) having primer probes and enzymes were run in between experiments to verify no cross-contamination occurred in between runs. Since the NTCs have all the ingredients for a PCR experiment except for the DNA, any carryover DNA it picks up from the system would be amplified and show in the results showing cross-contamination. A dilution series experiment was also run with various concentration of the cbbL gene from 10^1 copies to 10^7 copies per 10 µL to qualify the efficiency, sensitivity, and dynamic range of the instrument. For these experiments 10 µL reaction volumes were loaded onto the instrument for analysis.

The recorded intensity measurements were then analyzed using custom MATLAB® scripts. Because of the continuous nature of this instrument, a robust MATLAB® script was developed that can analyze simultaneous data from all the 37 channels as well as track the droplet order from one cycle to the next. The sizes of the droplets/plugs were chosen so that they were larger than the dimensions of the tubing, thereby ensuring the preservation of the droplet sequence across all cycles. To account for the possibility of coalescence and/or breakup of the fluid plugs propagating through the tubing, the detection algorithm was designed to collate the data and distinguish between different reaction numbers and volumes. After extracting the recorded average peak intensities they were normalized and the relative fluorescence intensity plotted as a function of PCR cycle. An algorithm was also developed for the automated detection of the C_t values for each of the runs.

10.3 Results and Discussion

During the initial evaluation of the instrument, the temperatures of the hot zone and the cool zone was set at 95° C and 60 °C respectively. With these temperature values however, expected PCR results were not obtained. It was determined that because of the

fluid flow and the insulation, in some cases it was causing the temperature of the fluid to not cool down enough in the cool zone and was causing the fluid to heat up over 95 ^{o}C in the hot zone. In order to account for this, the temperatures of the four zones were compensated so that the fluid can maintain a constant temperature profile. Consequently, the temperatures of the four zones were set as 95 ^{o}C, 94 ^{o}C, 56 ^{o}C and 58 ^{o}C respectively. This immensely improved the PCR results and thus was maintained for all the subsequent experiments.

Since a single wrap around the heater was calculated to be 47 μL, the total volume for the entire thermocycler was thus 1.9 mL. Taking into account additional lengths of tubing at the inlet and outlet, for a single PCR run, about 2.2 mL of oil was consumed per run. But because of the continuous flow nature of this instrument, multiple reactions could be run at the same time reducing the amount of carrier fluid required per sample.

As the fluid flowed through the 40 wraps of the PCR thermocycler, the intensity values were obtained in real time and plotted over time as illustrated in Figure 10.2. As can be seen from this figure the fluorescence intensity increases gradually as the PCR reagents progresses through the 40 cycles. In order to account for breakup and coalescence of droplets, the data was analyzed and only the top 95th percentile of the intensity values were considered in determining the overall intensity for a particular reaction from a particular channel. Additionally, droplets of a certain width were only accounted in the algorithm in order to reduce the possibility of skewed results due to satellite droplets and debris. Since by design droplet sequences were preserved across subsequent channels droplet tracking was performed through and the detection algorithm designed to collate the data and distinguish between different reaction numbers and volumes. This approach was determined to be robust enough to account for

air bubbles, as they are of a lower intensity than the fluorescence intensities of the reaction volumes and were thus ignored in the analysis.

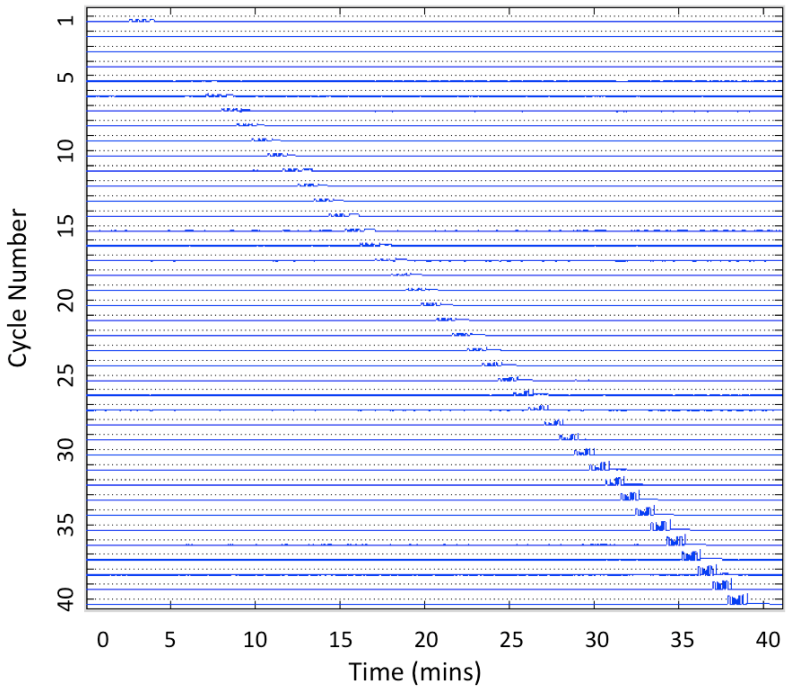

Figure 10.2: Plot of Intensity Signals of 37 PCR Channels Over Time

Once the data from the entire PCR run was obtained, the data was normalized with respect to the 200 nM fluorescein solution since the intensity response from the 37 PMT channels were not uniform as was evident in Figure 9.4. Figure 10.3a shows the raw fluorescence intensity values plotted against each cycle number for a SAR11 sample with a starting DNA concentration of 10^5 copies per 10 µL. After normalizing the data from Figure 10.3a against that from Figure 9.4, the normalized PCR curve as shown in Figure 10.3b was obtained. The contour of the bar graph illustrated in Figure 10.3b looks like a familiar PCR amplification curve. The intensity value obtained in cycle 5 was lower than that obtained in cycle 1 and was found to be uniformly lower in all other runs as well. Consequently, it was determined to be an aberration and ignored for calculating background baseline intensity values.

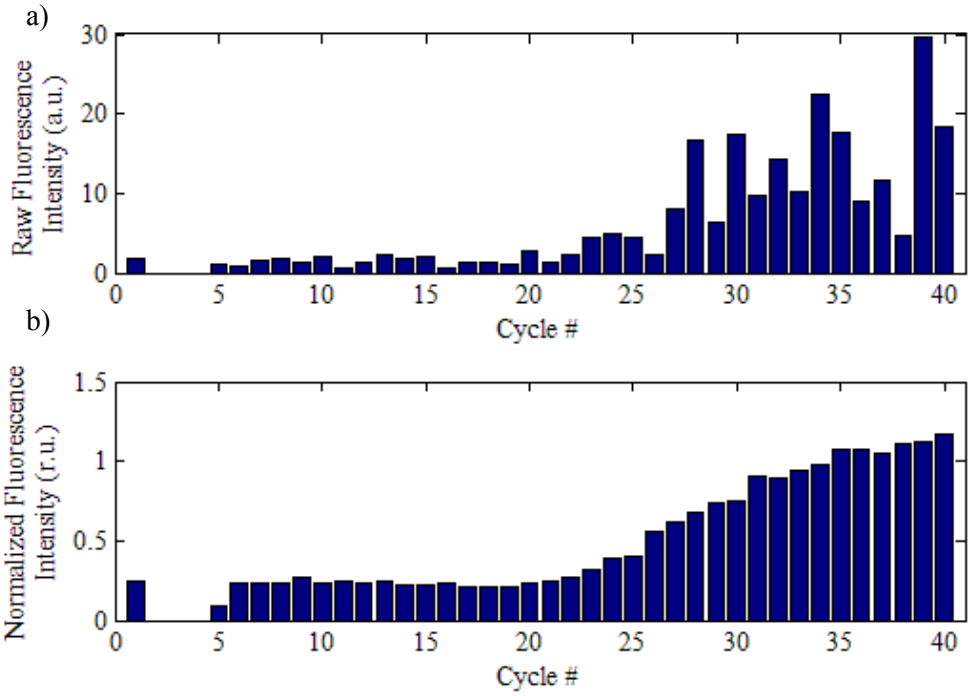

Figure 10.3: PCR Amplification Curve for 10^5 copies/10 µL Concentration of SAR11 Gene a) Raw Intensities b) Normalized Intensities

As has been explained before, the C_t of a real-time PCR experiment is the cycle number when the fluorescent signal from the reaction crosses a set threshold value. In case of many commercial real-time PCR instruments the threshold is set to be about 10 times the background signal level. However, every instrument is unique and the setting of the threshold value is something that can be of an arbitrary nature to some extent, as long as the adopted algorithm is uniformly applied for all the runs.

In this work, initially, the approach that was followed was setting the threshold to be just above the highest intensity value of the first few non-amplified cycles in any run. Then a slope was drawn through the at least the first three cycles which crosses that set threshold. The intersection of these two lines was then considered at the C_t value for that PCR run as illustrated in Figure 10.4. One of the problems for this approach was that, in case of noisy signals, if the signals levels from one of the initial cycles show up as a high

value, it artificially raised the threshold value thereby reporting higher C_t values than one would expect. Similarly, the slope of the exponential amplification can also be skewed in case of noisy signals thereby reporting erroneous C_t values. Additionally, although this method was a good way of visually determining the C_t value, it was difficult to implement this algorithm consistently in an automated manner.

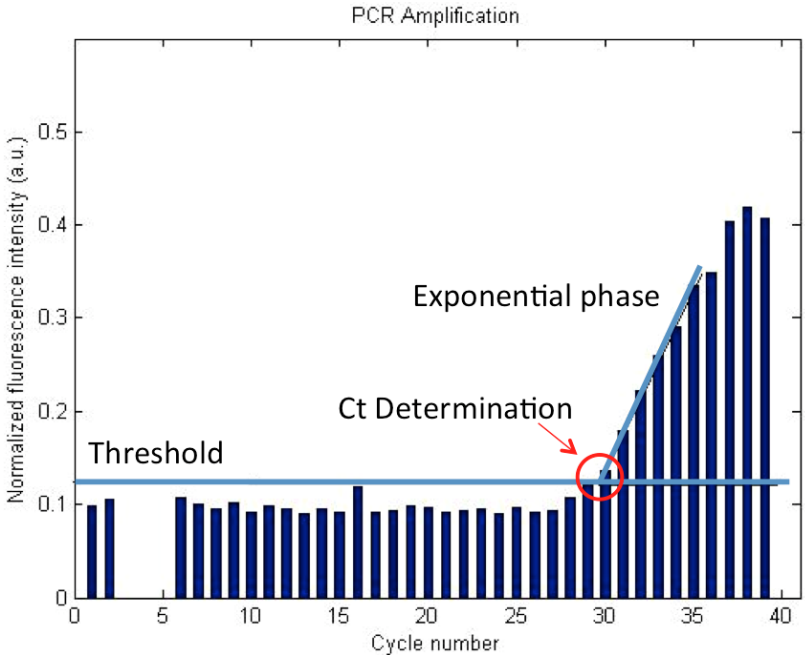

Figure 10.4: C_t Determination of 10^3 copies/10 µl of SAR11 Gene

Consequently, an alternate approach in which the average of the first 10 data points were used to set the baseline was used. The threshold value was set to be 2 times the value of this background fluorescent intensity value. In order to further reduce noise signals, a moving point average with a window of three data points was used to smooth out the entire dataset. The cycle number where the PCR curve crossed this threshold was then logged as the C_t value for that run as illustrated in Figure 10.5. This algorithm was thus incorporated in the MATLAB® script to obtain a uniform C_t value for all the runs. In order to calculate the baseline average, the signals from channels 2, 3 and 4 were not considered since they were not recorded. Additionally, since channel 5 was determined

to be aberrant, the value from that channel was also not considered for the calculation of the background signal level.

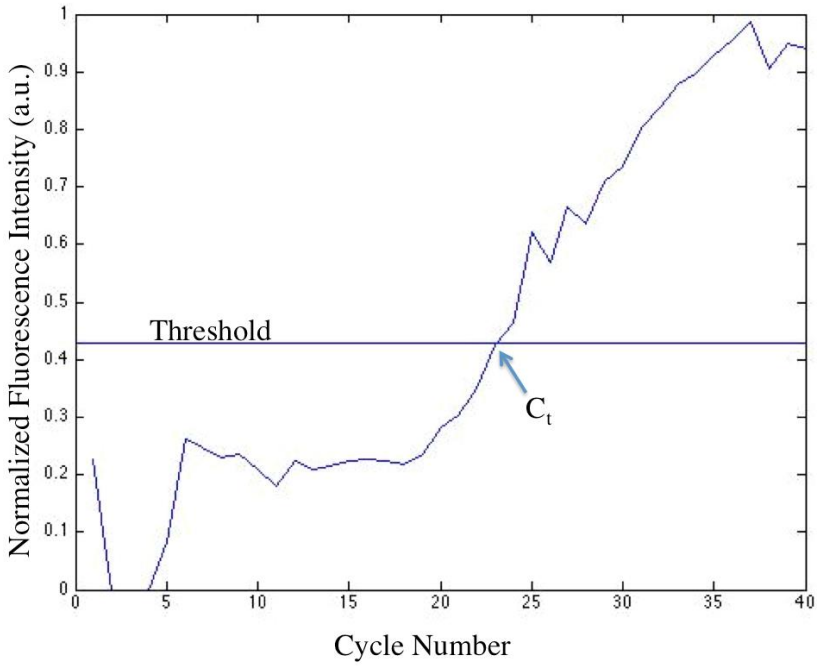

Figure 10.5: Alternate C_t Determination of 10^8 copies/10 µl of Thermus Gene

Serial dilution runs were three times through the developed instrument with randomized order. Additionally, NTC samples were run randomly at different times to verify that no cross-contamination was taking place. C_t values were determined from the algorithm explained before and compared with the C_t values obtained from a commercial instrument. The C_t values obtained from this instrument were found to differ from the corresponding C_t values from the commercial instrument by about 4, with the commercial C_t values being lower. However, this 4 C_t shift was found to be constant for all the PCR runs and was accepted as an offset for this instrument. In fact, no two real-time PCR instrument provides the same C_t values as well, because of variations in the instrument and C_t calculation algorithms. Table 10.1 shows a summary of the three dilution series runs with the SAR11 gene. As can be seen from data, the results are quite repeatable with a very low standard deviation between the three runs. In case of

10 copies/10 µl, the second run didn't provide any detectable C_t value which is not out of the ordinary for such low concentrations. Except for that concentration the standard deviation for all the other runs were less than 0.4. Even a standard deviation of 1.33 is not bad by any means for an instrument like this when considering the variability in the reagents while dealing with such low copy numbers.

Table 10.1: Summary of PCR Dilution Series Runs in Triplicate using SAR11 Gene

Copy Numbers	Run 1	Run 2	Run 3	Standard Deviation	Mean
10^1 / 10 µl	39.68	-[a]	37.8	1.33	38.74
10^2 / 10 µl	35.85	36.04	35.3	0.38	35.73
10^3 / 10 µl	32.78	33.12	32.6	0.26	32.83
10^4 / 10 µl	28.96	29.00	28.76	0.13	28.91
10^5 / 10 µl	25.99	25.49	25.7	0.25	25.73
10^5 / 10 µl	23.61	23.35	23.18	0.22	23.38
10^7 / 10 µl	19.95	20.42	20.51	0.30	20.29

[a] Fluorescence intensity did not cross detection threshold

The serial dilution real-time PCR curves are shown in Figure 10.6 with the $10e^0$ line corresponding to NTC. The mean C_t values from the dilution series run were used in determining the efficiency of the system from the standard curve as shown in Figure 10.7. The mean PCR efficiency was calculated to be about 109.5% with a R^2 value of 0.997238. The R^2 value signifies the goodness of the fit and higher the value, better the curve-fit as is evident in this case.

The instrument was also validated with DNA concentrations up to 10^{10} copies/10 µl. The instrument was thus successfully tested with a dynamic range of 10 copies all the way up to 10^{10} copies/10 µl and with consistent PCR results. Although

the qualification of the instrument was done with the SAR11 gene, similar results could be expected for other genes as well.

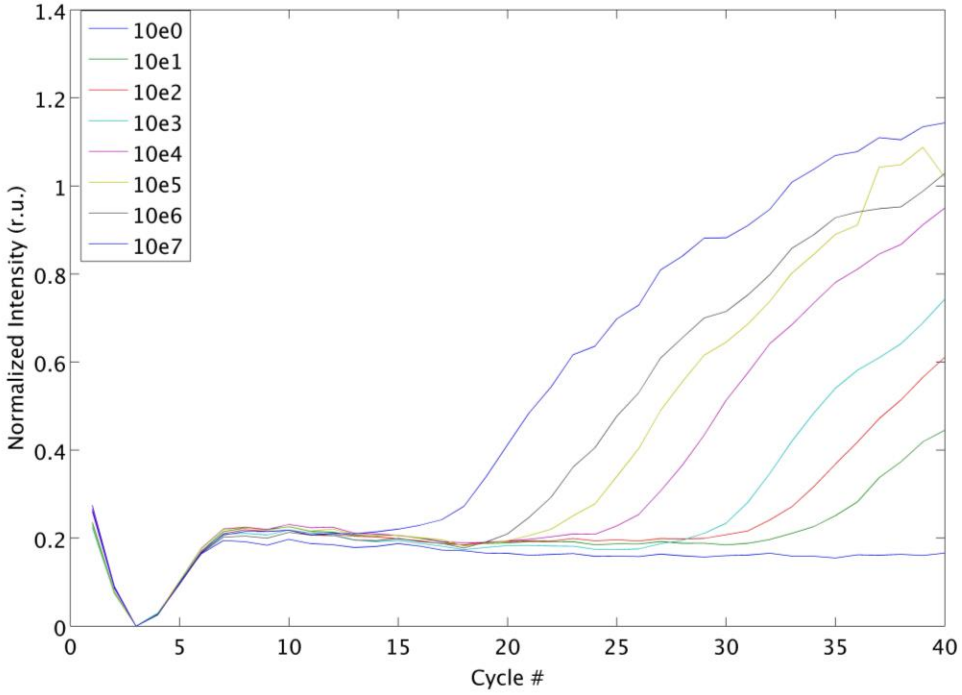

Figure 10.6: Real-time PCR Amplification Curves of Serial Dilution of SAR11 Gene

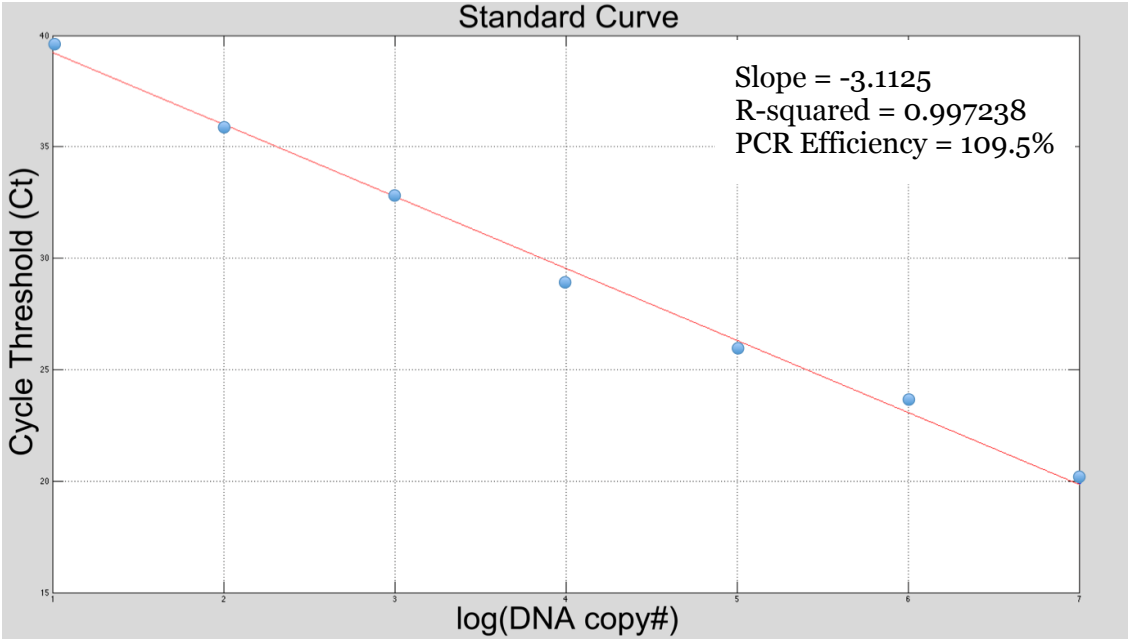

Figure 10.7: Standard Curve of Dilution Series Runs

The true flexibility of this instrument becomes evident when multiple samples are sequentially run through. This instrument was evaluated with up to 5 different concentration loaded one after the other and run through the system. The results showed minimal cross contamination between the reagent plugs while in the thermocycler. The MATLAB® script algorithms were robust enough to distinguish between different reagent concentrations and produce the results. Figure 10.8 shows a three PCR cycles with three different reagent concentrations and an air bubble as well, which was successfully distinguished in the algorithm. From the left the first plug is of concentration 10^4, 10^2 and 10^5 copies per 10 µL of SAR11 gene followed by a plug of air. The way the analysis algorithms have been developed, the satellite droplets were not considered for analysis and neither was the air plug.

Figure 10.8: Normalized PCR Data Showing Simultaneous Reactions through the PCR Instrument

10.4 CONCLUSIONS

The continuous flow PCR instrument developed here has a great potential to be developed as a platform for performing high-throughput, autonomous real-time PCR experiments in the field. It can readily be modified based on the requirements for different sets of primers or fluorescent dyes. Simply increasing the number of tubing wraps can increase the number of PCR cycles. Similarly, changing the excitation and

emission filter provides the flexibility of using other types of fluorescent dyes apart from 6-FAM™. The set temperature points can also be easily changed based on primer probe requirements.

The focus of this design effort was towards a low power instrument that can be easily carried to a field, eliminating the need for transporting samples to full-scale laboratories. A single experiment can be performed in less than two hours with less than 60 watt-hours of power although because of the continuous flow nature of the instrument multiple experiments can be run simultaneous thereby reducing the time per experiment. Any standard laptop can be used for data analysis for prompt results although it is possible to perform all the control and data analysis using an embedded system as well further reducing the footprint and power requirement.

CHAPTER 11

DEVELOPMENT OF THE DIGITAL PCR SYSTEM

11.1 INTRODUCTION

The real-time qPCR instrument developed as part of this work has been evaluated and validated for use as a portable instrument, which has a great potential for field-based applications. However, the power and size of the instrument was something that was over the size and power constraints of the 3G ESP platform.

Consequently, an alternate approach was required for the purpose of developing an instrument for the 3G ESP platform. In order to satisfy the design constraints of the 3G ESP platform, the total power required needs to be reduced. Additionally, the size of the instrument was more than the volume that can fit inside the platform. Another aspect of the design of the real-time system was the use of 74 optical fibers. Although they are great for efficient optical coupling for both excitation and detection, they are not quite amenable to bumpy environments. In the high seas the *Tethys* LRAUV platform is expected to be jostled around by the waves as well as potentially be bumped by marine animals. The use of long optical fibers in this kind of scenario does not lead to a robust instrument. Another aspect of the real-time qPCR instrument that was not amenable for low power, mobile and remote operations is the amount of data analysis required to analyze 37 channels continuously to generate the result. Running full scale MATLAB® scripts requires high power embedded processors and memory that are not feasible for this platform.

One of the PCR techniques that have been discussed before is the droplet digital PCR technique. This emulsion-based technique can provide quantitative DNA analysis by analyzing the fluorescence intensity just at the end of the entire PCR experiment of however many cycles. This instantly reduces the number of detectors and excitation

source to just one. It also simplifies the detection algorithm as it would necessitate a simple counting algorithm that just counts the number of 1's and 0's streaming through at the end of the reaction. Digital PCR provides absolute quantification as opposed to real time qPCR that needs a standard for absolute quantification.

Consequently, a redesign effort was undertaken to modify the system to be able to perform digital PCR analysis.

11.2 Modification of the Fluidic System

11.2.1 Design of Fluid Injector

The real-time instrumentation as reported in the previous chapters required an array of valves for the automated handling of the fluids inside the instrument. The power and size constraints of the target platform necessitated a redesign of the fluidic system so that the use of external valves could be limited. Additionally, because of the emulsion technique being used here, the use of external valves led to problems with the stability of the emulsions through the valves. For efficient and low-power analyte introduction or metering in emulsion systems on-chip inline valves are preferred. Various techniques for valve-less microfluidic systems have been reported using electroosmosis [125], [126], passive capillary forces [127], *etc*. However, this necessitates sophisticated design and fabrication processes for the chip. Also, on-chip valves still require the need for external positive or negative pressure sources or computerized high voltage sources.

Consequently, for fluid injection and metering, a low power valve-less system was designed that was compatible with emulsion systems. This design essentially was based on the principle of a rotating central cylinder with openings only at certain locations that line up the desired input and output paths. In order to be compatible with the fluorinated oils being used in this work, the device was mostly made out of Teflon with it being the only wetted material as well. The central cylinder was sandwiched between two

discs, also made out of Teflon that contained the opening for the inlet and outlet. The two discs were pressed against the face of the cylinder to form a fluid tight seal. Since Teflon is a softer material, in order to properly distribute the pressure over the entire cylinder and to facilitate the use of Nanoport™ connectors, the sandwiched cylinder and the disks were bolted down using Aluminum plates. To ensure a proper fluidic seal, the moving Teflon surfaces responsible for the sealing were polished to get a flat and smooth surface. The bolts were tightened such that the fluid seals were adequate, while at the same time only requiring a reasonable amount of torque to rotate the sandwiched cylinder. An illustration of the injector fluid with its internal components is shown in Figure 11.1a.

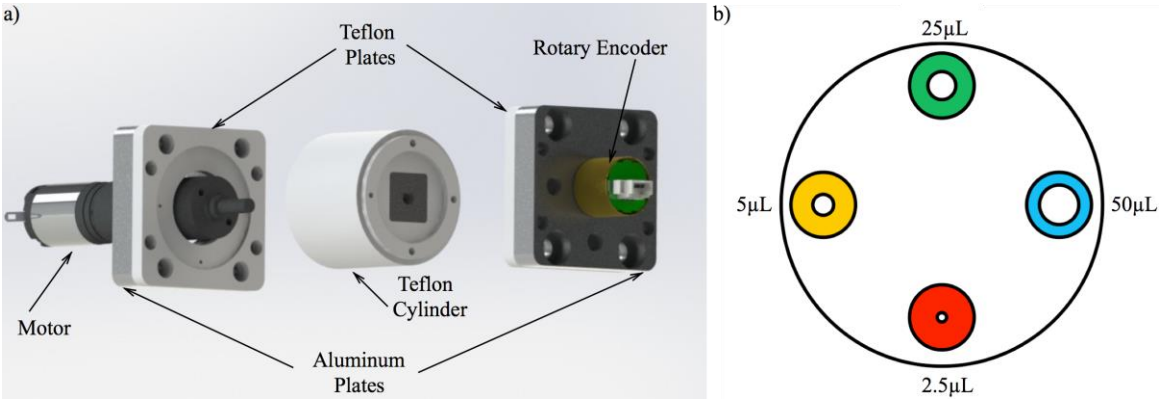

Figure 11.1 : Schematic of the a) Components of the Fluid Injector and b)Cross-section of the Teflon Cylinder

Multiple variations of the injector loop were developed depending on the application based on the same underlying architecture as detailed above. The architecture explained can be used as a fluid injector with precise metering as illustrated in Figure 11.1b. As illustrated, capillary tubing with specific diameters were inserted in different positions of the cylinder. Each of those can then be used for metering precise volumes to be injected through the outlet port for subsequent downstream processing. At first the volume required for injection was fed through the inlet port and the cylinder

rotated to line up with the corresponding capillary. Once the fluid was detected on the other side of the injector, the cylinder was rotated to the outlet position and then pushed out using the working fluid. In this manner, precise air bubble free volumes of the analyte can be injected without the need for external valves in a repeatable and consistent fashion. Figure 11.1b illustrates four different fluid volumes of 2.5 μL, 5 μL, 25 μL and 50 μL, although different number of ports and different volumes can easily be accommodated as well.

In order to cross-connect the inlet and outlet ports, the central cylinder was rotated using a Maxon RE13 DC Motor (Part No. 118459, Maxon Motor Ag, Switzerland) with a planetary gearhead with a gear ratio of 664:1 (Part No. 352394, Maxon Motor Ag, Switzerland). A high gear ratio was chosen as it can provide a high torque with a low power draw. The choice of the gear ratio was dictated by the size of the injector as the surface area subjected to friction determined the torque necessary to overcome the static and dynamic friction during movement. To determine the position of angular position of the rotating cylinder, a miniature rotary absolute magnetic shaft encoder (MA3, US Digital, WA, USA) was connected on the opposite side of the motor. The motor was driven to specific angular positions by incorporating the feedback from the absolute encoder. The control was achieved using an Arduino microcontroller as illustrated in Figure 11.2. A quadruple high current half-H bridge driver (L293, Texas Instruments, TX USA) was used to provide the higher bi-directional drive currents necessary for the motor to enable bi-directional rotation.

Another variation of the injector loop was implemented in which different analytes could be brought in from different inlet ports and then mixed in a chamber inside the central cylinder as illustrated in Figure 11.3b. Initially the chamber was filled with the fluorinated oil. Once the analyte comes in through the inlet port it floats up

because of its lower density while the excess fluorinated oil was drained through the bypass port located at the bottom of the injector. As the cylinder rotates to a different inlet port, it shears off the liquid in the previous port and it floats up. This way multiple analytes could be introduced inside the inner chamber for collection for later injection or coalescence. In case of emulsions stabilized with the addition of surfactants electrocoalescence was necessitated that was accomplished by having two high voltage electrodes incorporated in the injector design.

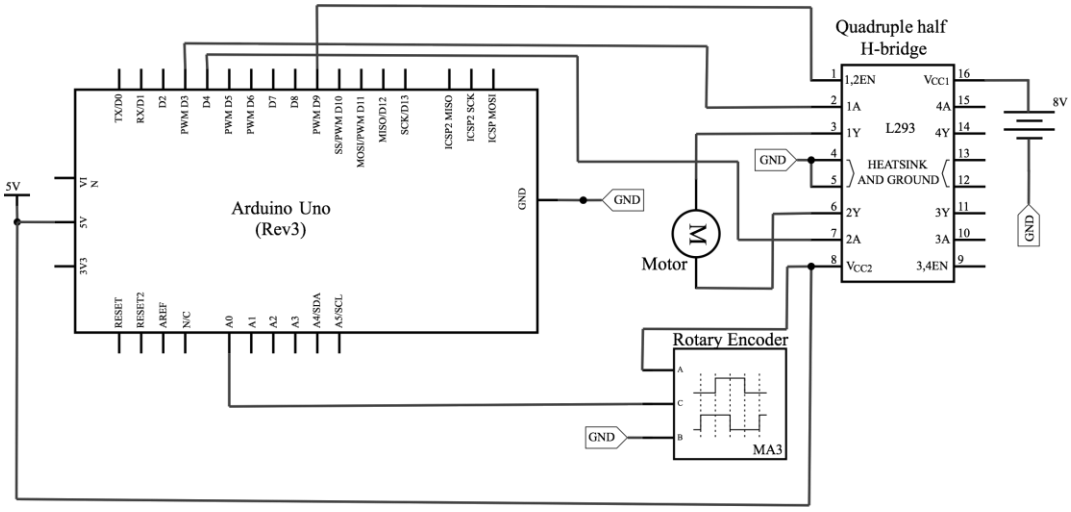

Figure 11.2 : Electronic Control Circuitry for the Fluid Injector

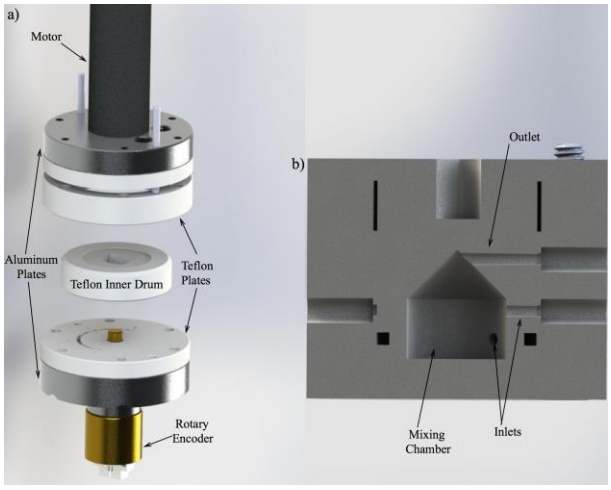

Figure 11.3 : Schematic of the a)Fluidic Mixer and b) Cross-section of the Mixing Chamber

A versatile design was thus developed here for the purposes of fluid handling and injection without making use of bulky valves that is suitable for emulsion systems as well. This allowed reduction in the overall design both in terms of power and space.

11.2.2 Design of Droplet Generator

In order to perform dPCR though, much smaller reaction volumes with a very high level of uniformity were required. This was found to be hard to achieve using the T-junction droplet generation owing to surface wetting of the PCR reagents during droplet generation. As a result the flow-focusing droplet generation technique was evaluated and the droplet generation was found to be much more stable and uniform with much smaller droplet volumes quite easily feasible. Although this process of droplet generation was not quite amenable to parallel generation of droplets simultaneously, but for the purposes of this work, it was determined that achieving uniform droplet generation was more important.

The flow focusing design that was used for this work is illustrated in Figure 11.4. The oil flow was branched out into two paths from the single inlet to equalize the fluidic resistance of the two paths, which was a critical aspect for the generation of stable droplets from the junction. Two basic designs of the flow focusing junctions were evaluated as illustrated in Figure 11.4 (1) and (2). A variety of dimensions were evaluated to identify the optimum dimensions for the generation of stable droplets of the desired volume. The chips were still treated with a mixture of (Tridecafluoro-1,1,2,2-Tetrahydrooctyl)-1-Triclorosilane and HFE-7100 using the protocol discussed earlier.

For droplet generation, primarily the BioRad Droplet Generator Oil was used in this work as it provided a stable and uniform stream of droplets that hardly showed any coalescence even after 45 cycles.

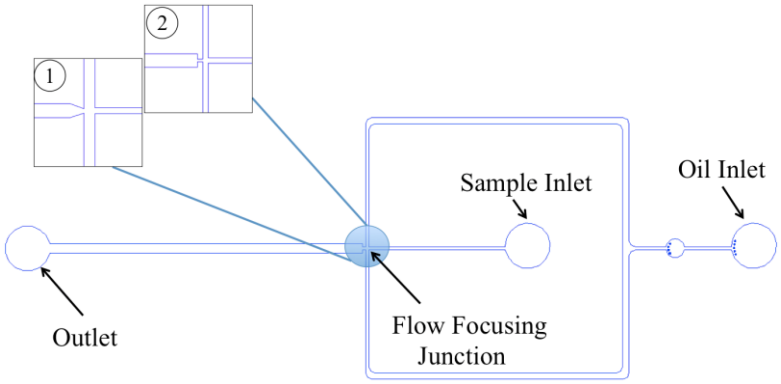

Figure 11.4 : Schematic of the Flow Focusing Droplet Generator Design

11.3 Modification of the Thermocycler

For the dPCR system, the volume of the droplets was much smaller than the real time system. Consequently, smaller ID tubing could be used for the thermocycler, which enables the use of a smaller thermocycler that can further reduce the power requirement. Because of the need for smaller droplets, the diameter of the tubing around the thermocycler was shrunk to have an ID of around 250 µm and OD of around 300 µm. This reduced the total liquid volume required for the experiment as well as the size of the thermocycler. Also, since real time monitoring was not necessary anymore, the entire thermocycler was wrapped in insulating foam. The combination of having a smaller thermocycler and better insulation reduced the power draw of the system considerably.

A custom designed and machined thermocycler, similar to what has been explained previously in Chapter 8 albeit with a smaller OD of 2.5 inches and a height of 2 inches. With this design, the fluid capacity of a single wrap of the tubing around the thermocycler was calculated to be about 10 µL. The heater control circuit developed before was similarly used for maintaining the thermal profile of the four zones as illustrated in Figure 11.5. In this design, flexible 5 Watts/in^2 power density Kapton® heaters were affixed to the backside of the aluminum segments corresponding to the 60 ^{0}C side. In case of the 95 ^{0}C side however, 10 Watts/in^2 heaters were attached as they

needed a higher power to maintain the higher temperature. All of the heaters were 2 inch by 2 inch in dimension except for the heater attached to first 95 °C zone which was 1 inch by 2 inches. Because of similar reasoning as before, the first 95 °C zone was connected to the raw battery voltage instead of stepping the voltage down to 8 V.

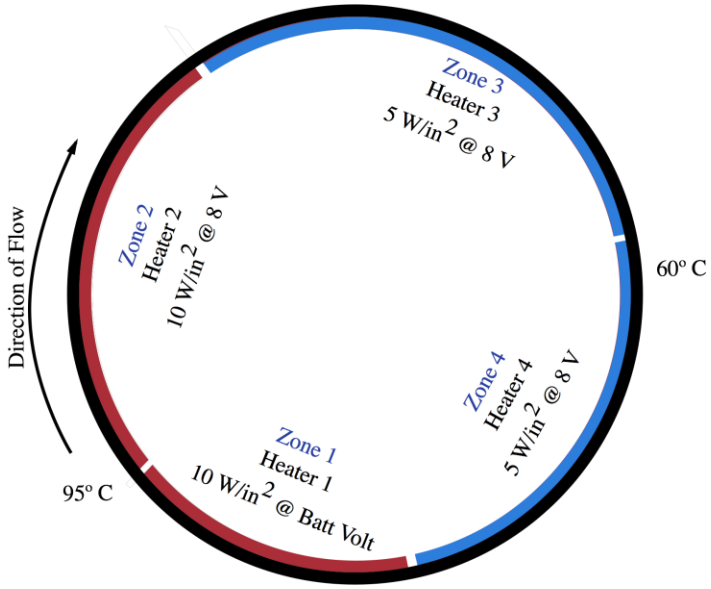

Figure 11.5 : Schematic of the Thermocycler Heating Zones for Digital PCR

11.4 Modification of the Optical System

In case of dPCR, as explained before, each of the droplets is considered a separate PCR reaction. Furthermore, it relies on end point detection of those droplets to distinguish between droplets that have amplified DNA in them (positives) and droplets that do not (negatives). The number of positive and negative droplets can then be used to estimate the absolute starting concentration of the sample. There's no need for monitoring the amplification of the individual reaction chambers from one cycle to the other. Thus, for this method, the detection can be performed at the very end of the PCR experiment. Consequently, a single excitation and detection channel was sufficient for the quantification of the starting concentration of the DNA.

This greatly simplifies the optical system design, as a single PMT could be used for the detection. For this work, the optical system was designed with a dichroic mirror as illustrated in Figure 11.6. A broadband LED (Luxeon ® LXML-PB01-0040, Quadica Developments Inc., Canada) mounted on a 25 mm round CoolBase LED assembly (Quadica Developments Inc., Canada) was used as the light source to excite the droplet containing the PCR products. The light coming out of the LED was cleaned up using the band pass excitation filter as before to obtain excitation around a center wavelength of 475 nm. The dichroic mirror reflects the blue excitation light while allowing the emission wavelength of around 540 nm to pass through onto the PMT detector (H10722-20, Hamamatsu Photonics, USA) through a 150 µm pinhole (P150S, Thorlabs, USA). The pinhole helps in efficiently rejecting out of focus light. 4 mm focal length aspheric lenses (C610TME-A, Thorlabs, USA) were used to focus the light properly onto the channel. On the detection side, a 20 mm focal length aspheric condenser lens (ACL2550, Thorlabs, USA) was used to focus the emission light on the pinhole giving a magnification of 5X at the PMT face for the emission path. In order to obtain the most efficient coupling, the fluid channel was incorporated in the optical detection system. This helped further reduce accidental misalignment of the optics with respect to the fluid channel.

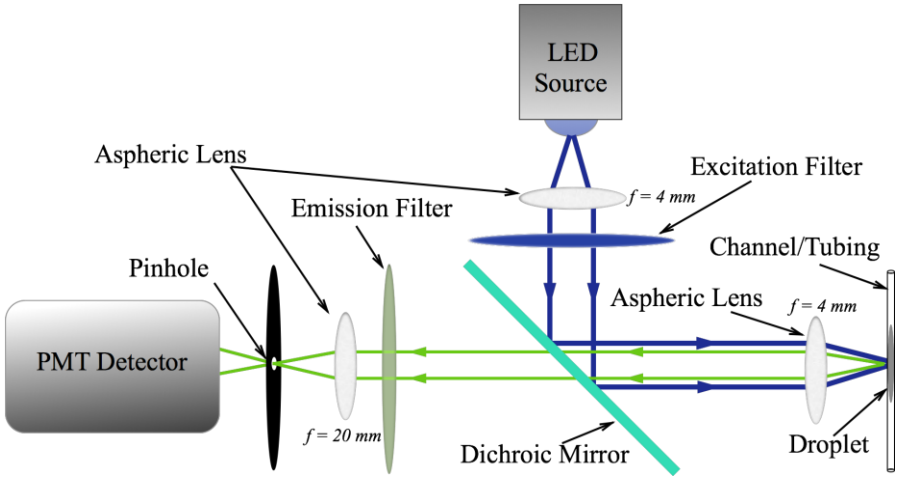

Figure 11.6 : Schematic of the Optical Detector Setup for the Digital PCR Instrument

Two schemes were evaluated as part of this work for detecting the fluorescence intensity of the droplets. In one case, the droplets were detected while they were still in the FEP tubing, and in the other case, the droplets were introduced onto a planar chip for the detection. In the former case, the tubing was stretched at the point of detection, so that the droplets get a higher transit time in front of the detection optics, thereby enabling easier detection. In the latter case, the droplets were introduced onto a planar chip similar to what has been illustrated in Figure 11.4 through the "outlet" side. In this orientation, the droplet was detected while it transits through the narrow channel. The oil flow was maintained at a very low flow rate such that it doesn't lead to droplet formation, but instead induces greater separation between adjoining droplets. The basic premise of both of these approaches relies on achieving separation between the successive droplets while at the same time increasing the transit time of the droplets in front of the detector.

The schematic illustrated in Figure 11.6 was implemented using an electronic control scheme with an Arduino based ATMEGA328 microcontroller as part of this work. A PWM based control was used to drive the LED at a lower duty cycle and synced with the PMT to record the signal only at a specific sampling frequency similar to what was employed in case of the real-time instrument using the Vertilon board. The entire control was implemented using the ATMEGA328 microcontroller using the schematic illustrated in Figure 11.7. The LED was driven using a BuckPuck LED driver (3021-D-I-350, LEDdynamics, Inc., VT USA) to provide constant current. The -5 V required by the PMT module was supplied using a charge-pump voltage inverter IC, MAX660 (Maxim Integrated, CA USA). The PMT module used in this work provided a 1 V reference voltage that could be used to set the gain of the PMT using a resistor divider network. Sets of jumpers were incorporated in the circuit to provide flexibility to choose different

gain values for the PMT. As per the specifications of the PMT, a gain value between 0.5 V to 1.1 V could be used. The circuit was set up for four possible gain values as follows, 0.5 V, 0.6 V, 0.65V and 0.7 V as it was determined that they would be enough for getting adequate signal from the PMT. Higher gain values were avoided to reduce the noise from the PMT module.

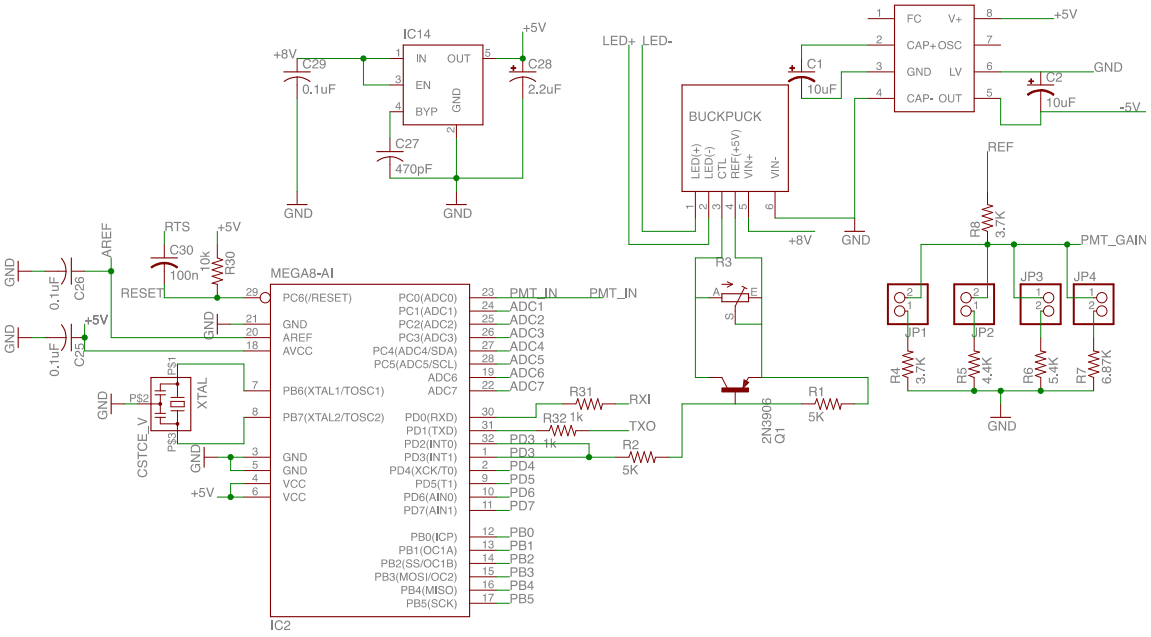

Figure 11.7 : Circuit Schematic of the Optical Detector System for the Digital PCR System

The data was collected using the ATMEGA328 microcontroller and the determination of positive and negative droplets were done on board the microcontroller. To determine the signal levels of the two types of droplets, extensive analysis was performed to fix the threshold values of the signals that could be expected for each of the droplet types.

11.5 Results And Discussions

The fluid injector was evaluated to determine the level of fluid sealing that could be achieved when none of the fluid paths are open. The inner Teflon cylinder was rotated so that none of the ports line up and the inlet path pressured until leakage was observed. It

was determined that the amount by which the Teflon surfaces were polished had a direct bearing on the pressure the fluid injector could withstand before leaking. Consequently, the Teflon surfaces were polished using a fine grit sandpaper to obtain a uniform polish on both the sealing surfaces. It was observed that the fluid injector could withstand pressures of up to 40 psi before it started to leak with a very smooth polish.

Additionally, the amount of tightening of the bolts had a direct bearing on the leak pressure. However, the bolts couldn't be tightened too much as it would cause the motor to be unable to rotate the inner cylinder. Also, if the bolts were not uniformly tightened, it caused the motor to have to deal with non-uniform torque. The bolts were thus tightened uniformly to obtain a uniform torque of 150 milliNewton-meter (mN-m). One interesting phenomenon observed was that the breaking torque to start the movement of the Teflon cylinder after sitting in one position for a while was a little higher than the continuous torque required to rotate the cylinder. This could be attributed to the higher static friction of the surface over its dynamic friction. The breaking torque was observed to be around 200 mN-m.

In terms of the operation of the fluid injector, precise volumes of the desired fluid could be injected into the fluidic path repeatedly and consistently without any problem. The microcontroller based control algorithm could achieve the target angular position with an accuracy of $\pm 0.5^{0}$. The entire control circuit and the driver for the fluid injector drew a power of less than 1 Watt.

For the generation of droplets, the flow-focusing design was evaluated and was found to perform much better than the T-junction design. The PDMS mold was fabricated from a master that was fabricated using KMPR® on Silicon using the same process as discussed earlier. The design illustrated in Figure 11.4 (2) was found to provide a better uniformity in the formation of droplets as illustrated in Figure 8. The

volumes of the droplets generated for this work were about 0.5 nL, which would produce thousands of droplets from a total starting reaction volume of 5 µL. The droplets formed were monodispered and quite stable and no coalescence was observed.

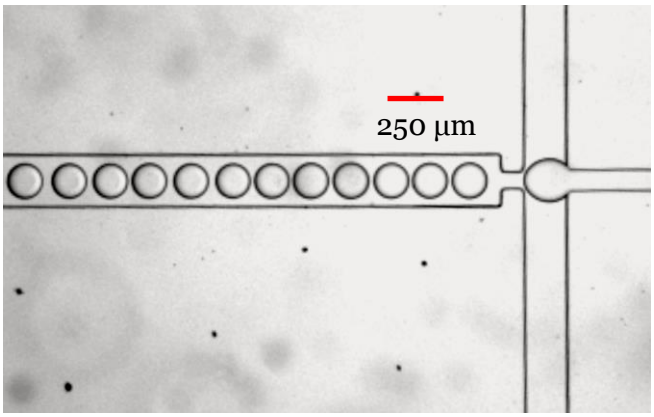

Figure 11.8 : Generation of Droplets from a Flow Focusing Junction

Droplet stability through the entire experiment until the end of the 45 cycles was really critical for the success of the dPCR system. Consequently, various formulations of the droplet generator oil and PCR Mastermix were evaluated. The best results in terms of droplet stability were observed when using the Biorad Droplet Generator Oil in conjunction with the Biorad Mastermix (ddPCR™ Supermix for Probes, BioRad, CA USA). The droplets were quite stable in the tubing and did not appear to coalesce even when they came in contact with each other as illustrated in Figure 11.9.

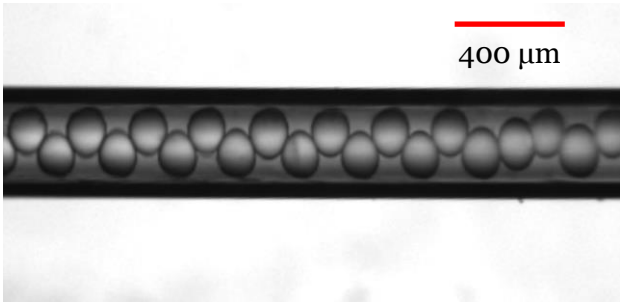

Figure 11.9 : Droplets inside FEP Tubing

Three types of heaters were used in this thermoccycler as mentioned before. For the two 60 ºC zones, 2 inch by 2 inch 5-W/in² heaters were used with the resistance of

each determined to be 40.2 Ω. For the 95 ºC zones, 10-W/in² heaters were used; for the first zone, a 1 inch by 2 inch heater was used whose resistance was determined to be 38 Ω while for the second zone a 2 inch by 2 inch heater was used whose resistance was determined to be 19.1 Ω.

The total power draw of the thermocycler in the configuration illustrated in Figure 11.5 was also determined to ensure that the current and power requirement of the thermocycler were within the specifications. The data in Table 11.1 illustrates the peak power requirement of the thermocycler during the warm-up phase, which were found to be within specifications. As can be seen from the table, the peak power draw of the thermocycler during warm up when the battery voltage was at 18 V was 14.68 W at 1.26 A and when the battery voltage was at 10 V, the power draw was 9 W at 1.06 A. Furthermore, this was the power draw during the warm up phase which lasted for around 10 minutes before the PID control reduced the duty cycle of the PWM driving the heaters thereby reducing the total power draw as the temperature comes up to their set points. During the experimental run with a flow of 10 μL/min, in order to hold the temperature, the thermocycler drew less than 3 W of continuous power.

Table 11.1 : Peak Current and Power Draw of the Real-time Thermocycler

Heating Zone	Current	Power
Zone 1	0.46 A @ 18 V 0.26 A @ 10 V	8.28 W @ 18 V 2.60 W @ 10 V
Zone 2	0.40 A	3.20 W
Zone 3	0.20 A	1.60 W
Zone 4	0.20 A	1.60 W
Total	1.26 A Max / 1.06 A Min	14.68 W Max / 9.00 W Min

The thermocycler was evaluated by monitoring the thermal stability of the temperature zones and its power consumption. The temperature profile was found to be quite a stable for both the temperature zones. However, because of the insulation all around the thermocycler without any break, it was found that the first 60°C zone couldn't vent off heat properly with fluid flow and ended up with a much higher temperature as the experiment progressed. Consequently, a slit was opened in the insulation in that zone to allow the heat to be vented that worked great in maintaining the temperature profile.

Fluorescence intensity of the droplets at the end of the PCR run were detected using a narrowed down section of the tubing as well as by introducing it into a chip as mentioned before. It was found to be very difficult to align the narrowed down tubing with the optics, furthermore it was hard to get proper separation between successive droplets. Consequently, the peaks of the positive and negative droplets couldn't be properly distinguished for counting them. Reintroduction of the droplets into the droplet separation chip along with the separator oil allowed much better distinction between successive droplets. For all subsequent experiments this latter approach was followed as illustrated in the setup shown in Figure 10.

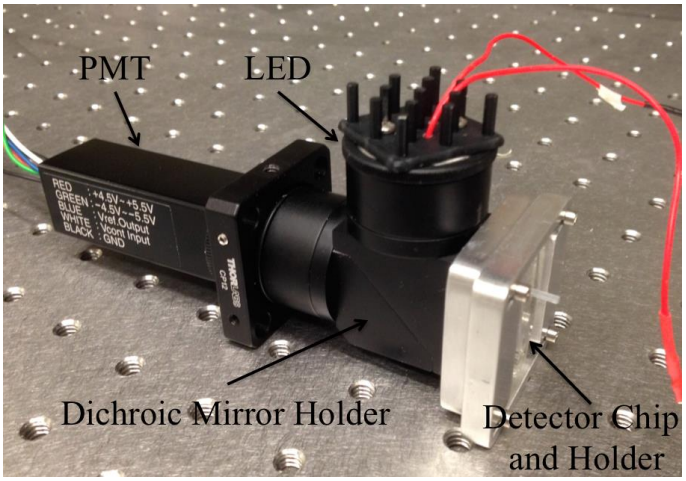

Figure 11.10 : The Optical Detector System

An algorithm was developed for peak detection that could distinguish and count the number of positive and negative droplets. Two data points were read successively and averaged to provide a single data point. The data was looked at both without smoothing and with smoothing by using the exponential smoothing technique. However it was determined that the smoothing process introduced artifacts, like lowering the peaks of some of the droplets, and because of that the raw data was used for the analysis.

The data capture rate was determined as a function of the transit time of the droplet through the channel in front of the detector. The width of the channel where the detection took place was around 100 μm with a height of about 45 μm. The spot size of the emission collected by the PMT was estimated to be around 30 μm and the fluid flow rate was around 10 μL/min. With these parameters, the residence time of each droplet with a volume of 0.5 nL was calculated to be about 3.8 ms as illustrated in Equation 11.1. This translated to a frequency of occurrence of about 260 Hz.

$$\frac{\frac{DropletVolume}{Channel\ Cross-sectional\ Area} + Detector\ Field\ of\ View}{\frac{Volumetric\ Flow\ Rate}{Channel\ Cross-sectional\ Area}}$$

$$\Rightarrow \frac{\frac{0.5nL}{45\mu m * 100\mu m} + 30\mu m}{\frac{10\mu L/min}{45\mu m * 100\mu m}}$$

$$\Rightarrow 3.81\ ms \qquad \text{Eqn. 11.1}$$

Based on the data sampling rates possible on the Arduino platform, a capture rate of about 1 KHz was selected, which was about 4 times the signal frequency and was deemed to be adequate. However, since the LED was being pulsed in this system to reduce the power consumption, the PMT capture was synced with the LED flashing at 1 KHz using hardware interrupt on the ATMEGA328 microcontroller. A duty cycle of 50% was determined to be enough for data capture during the LED on-time and data analysis during the LED off-time. A considerable amount of work was performed in

order to properly align the detector chip with the LED and PMT according to the schematic illustrated in Figure 11.6 to obtain the best signal to noise ratio..

In order to qualify the optical detector setup, pre-amplified DNA was run through the detector chip to determine the signal levels for the positive droplets. Similarly, unamplified DNA was used to determine the signal levels for the negative droplets. Using the SAR11 gene, the signal from positive droplets were determined to be 4 V, while that from negative droplets were determined to be 0.5 V as illustrated in Fugure 11.11. These threshold values were then incorporated in the droplet detection program.

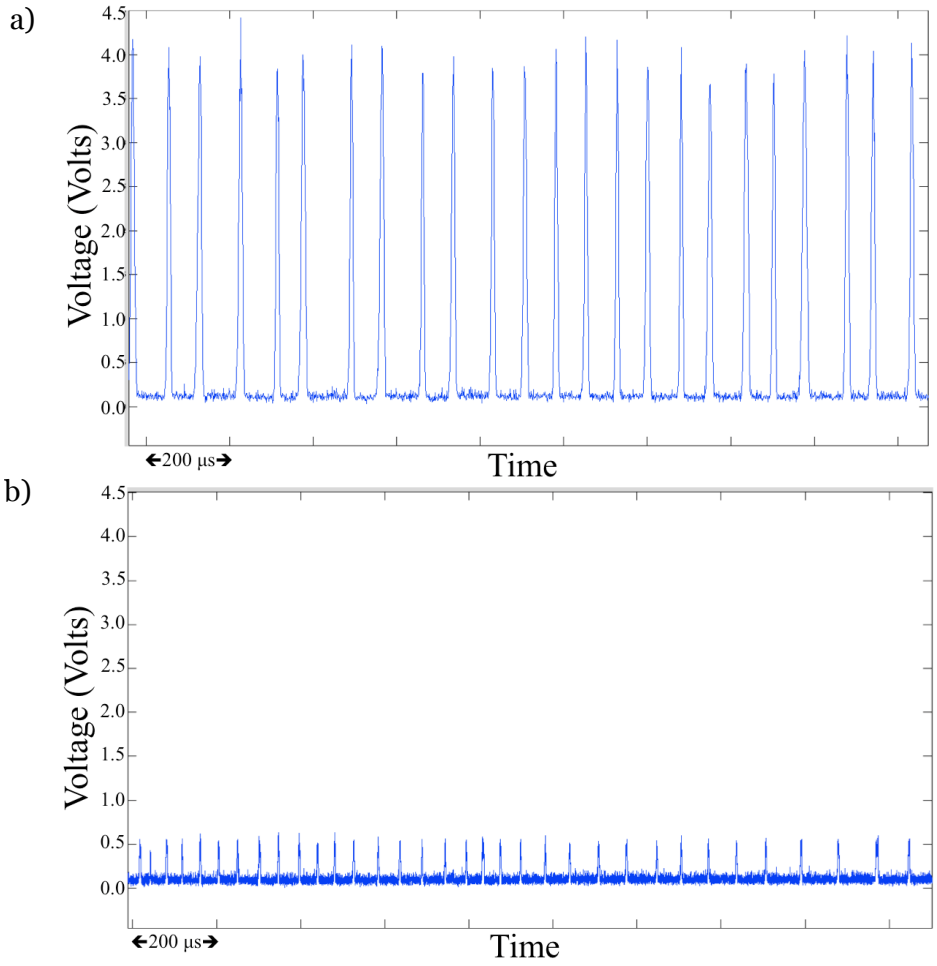

Figure 11.11 : Signal Levels of a) Positive Digital Droplets, and b) Negative Digital Droplets

11.6 CONCULSIONS

The digital PCR instrument framework presented in this chapter addresses the issues with the real-time PCR instrument developed earlier. This platform now has the potential to be developed into an instrument that can be envisioned to be on the LRAUV platform. The biggest improvement over the real time system was achieved by moving to a single excitation and detector channel. This enabled not only in the reduction of power required for the optical detection scheme, but in its size as well. The entire optical detection and analysis was now implemented using less than 1 W. The lack of optical fibers enabled a much more robust implementation of a portable system. The system was evaluated with both amplified and non-amplified DNA samples and in order to fine-tune the optical detection system.

The fluid injection system developed in this work provides a great opportunity for automated fluid exchange without the need for bulky valves. The new design of the thermocycler also provided a savings of more than 5 W during the warm up phase. The entire system could now be operated within the specifications of 20 W and 2 A as outlined in the requirements of the LRAUV platform. It still retained all the flexibility offered by the real-time system because of the similarity in the design but with a much smaller size and power footprint.

CHAPTER 12

CONCLUSIONS

The main objective of this work was to develop instrumentation for the analysis of nucleic acids for a portable platform. For the development the instrumentation, the constraints and specifications laid down by the requirements of the MBARI 3G ESP platform was used as a guideline. Two different types of instrumentation were developed as part of this work. A continuous flow real-time instrument amenable for low-power, *in-situ* field operations was developed initially which was validated against commercial real-time PCR instruments. Although the developed instrumentation had a great potential as a field deployable PCR instrument, further development work was undertaken as part of this work in order to meet and exceed the power and size specifications laid down in the guidelines for the 3G ESP platform. Consequently, the framework for a digital PCR instrument was developed which could be used as a portable, fully automated instrument while meeting all the specifications of the original guideline.

As part of this dissertation, a background on the necessity of the monitoring of marine environments was provided along with the current state of the instrumentation used for that purpose. This dissertation also provides a theoretical background of the PCR technology and specifically emulsion based and emulsion based dPCR that have been the primary PCR technology used in this work. In Chapter 4, the role of microfluidics in biological analyses and the use of emulsions in microfluidic systems were discussed. The basic microfabrication techniques essential for the fabrication of the microfluidic devices were discussed in Chapter 5 along with the concept of soft lithography that was used to fabricate the fluidic chips in this work.

In Chapter 6, the groundwork of this dissertation was established. Various portable PCR platforms were surveyed and the viability of the various approaches were evaluated with respect to the requirements and specifications of the 3G ESP platform. Extensive analysis of the possible approaches for a portable nucleic acid detection system was performed and the emulsion based, continuous flow system with a cylindrical thermocycler and a PMT based fluorescence detector was identified as the optimum solution for this application. Three sub-modules of the overall instrument were identified with each of the next three chapters focusing on the design and development of the individual modules.

In Chapter 7, the development of the fluidic handling system was reported. The development of the fluidic system encompassed the development of the protocol for the fabrication of the glass-PDMS hybrid chips from KMPR® on Silicon masters. As part of this work the protocol for the fabrication of up to 200 μm thick KMPR® patterns on Silicon was developed. The identification of proper materials for the fluidic system was also undertaken to have a system that was conducive for an emulsion based system with minimal cross-contamination.

The development of the continuous flow cylindrical thermocycler was reported in Chapter 8. This effort entailed the design and fabrication of a cylindrical thermocycler with multiple fixed temperature zones with a PID based microcontroller controlled control routine. A continuous power draw of less than 5 W during the operation of the instrument was achieved which was great for portable applications.

In Chapter 9, an optical detection system using a 64-channel PMT capable of performing real-time monitoring of the fluorescence intensities at the end of each cycle was developed. This provided with a platform for a continuous flow real-time PCR instrument that can be used for *in-situ* applications with a low power budget (< 11 W).

In Chapter 10, the real-time system as envisioned was evaluated with DNA samples to qualify the instrument. A robust MATLAB® based algorithm was developed to determine the C_t values of the samples that could also keep track of emulsion plugs from one cycle to the next. This enabled high-throughput operation of the instrument with multiple reactions occupying the thermocycler at the same time. A dilution series experiment was performed and the efficiency of the instrument from the average of three runs was calculated as 109%. The results were also compared to a commercial instrument and shown to be comparable albeit with a constant 4 C_t shift, that could be attributed to differences in the C_t calculation algorithm and differences in optics and thermal profile.

Although the real-time platform developed here had great potential as a low-power, high-throughput, and portable instrument in its own right, its size and power requirements were over the specifications of the 3G ESP platform. Consequently, an alternate approach was required for the purpose of developing an instrument for the 3G ESP platform in order to satisfy the design constraints of the 3G ESP platform.

In Chapter 11 a framework for a digital PCR instrument was developed that was based on the idea of a single channel excitation and detection only at the end of the PCR experiment. This approach helped in reducing the overall power and size footprint of the device within the specifications, which could eventually lead it to be included in the 3G ESP platform. Novel innovations in fluid handling and the optical detection mechanism were also developed as part of this effort that has been reported in this chapter. Signal levels for amplified and non-amplified DNA products were determined experimentally to tune the detection optics thereby opening up the platform for actual PCR detection off of the redesigned thermocycler in future.

The focus of this work was to develop the systems as a prototype to validate some of the design innovations presented here and to evaluate the complete system. As a result this system was operated in a semi-automated fashion. But simple systems integration effort has the potential to easily modify this system for fully autonomous operation.

Future work on this effort would require the integration of the sub-modules as a standalone device with a parent microcontroller in charge of syncing their functions. Although this work was performed with the requirements of the 3G ESP platform as a guideline, because of the modular nature of the instrument it could quite easily be used as a backend analytical module for any application requiring nucleic acids analysis, including but not limited to point of care diagnostics, and other environmental monitoring applications. The systems were designed as a modular unit and thus could be coupled with any type of front-end sampler that can provide nucleic acid samples. Other areas where this type of instrumentation could become useful are in the area of portable diagnostics for developing countries that lack the infrastructure for full-scale laboratories.

REFERENCES

[1] H. B. Glasgow, J. M. Burkholder, R. E. Reed, A. J. Lewitus, and J. E. Kleinman, "Real-time remote monitoring of water quality: a review of current applications, and advancements in sensor, telemetry, and computing technologies," *J. Exp. Mar. Bio. Ecol.*, vol. 300, no. 1–2, pp. 409–448, Mar. 2004.

[2] M. D. Smith, C. A. Roheim, L. B. Crowder, B. S. Halpern, M. Turnipseed, J. L. Anderson, F. Asche, L. Bourillón, A. G. Guttormsen, A. Khan, L. A. Liguori, A. McNevin, M. I. O'Connor, D. Squires, P. Tyedmers, C. Brownstein, K. Carden, D. H. Klinger, R. Sagarin, and K. A. Selkoe, "Sustainability and Global Seafood," *Science (80-.).*, vol. 327, no. 5967, pp. 784–786, Feb. 2010.

[3] S. Kröger and R. J. Law, "Biosensors for marine applications: We all need the sea, but does the sea need biosensors?," *Biosens. Bioelectron.*, vol. 20, no. 10, pp. 1903–1913, Apr. 2005.

[4] J. P. Zehr and W. D. Hiorns, "Molecular Approaches to Studies of the Activities of Marine Organisms," K. E. C. Professor, Ed. Springer Netherlands, 1998, pp. 91–111.

[5] J. P. Zehr, I. Hewson, and P. Moisander, "Molecular biology techniques and applications for ocean sensing," *Ocean Sci.*, vol. 5, pp. 101–113, May 2009.

[6] T. Fukuba, T. Yamamoto, T. Naganuma, and T. Fujii, "Microfabricated flow-through device for DNA amplification—towards in situ gene analysis," *Chem. Eng. J.*, vol. 101, no. 1–3, pp. 151–156, Aug. 2004.

[7] T. T. Cynthia J. Bruckner-Lea, "Renewable microcolumns for automated DNA purification and flow-through amplification: from sediment samples through polymerase chain reaction," *Anal. Chim. Acta*, no. 1, pp. 129–140.

[8] M. J. LaGier, J. W. Fell, and K. D. Goodwin, "Electrochemical detection of harmful algae and other microbial contaminants in coastal waters using hand-held biosensors," *Mar. Pollut. Bull.*, vol. 54, no. 6, pp. 757–770, Jun. 2007.

[9] B. J. Hindson, S. B. Brown, G. D. Marshall, M. T. McBride, A. J. Makarewicz, D. M. Gutierrez, D. K. Wolcott, T. R. Metz, R. S. Madabhushi, J. M. Dzenitis, and B. W. J. Colston, "Development of an automated sample preparation module for environmental monitoring of biowarfare agents," *Anal. Chem.*, vol. 76, no. 13, pp. 3492–3497, Jul. 2004.

[10] C. Scholin, "What are 'ecogenomic sensors?' A review and thoughts for the future," *Ocean Sci.*, vol. 6, no. 1, pp. 51–60, Jan. 2010.

[11] C. Scholin, C. Preston, A. Harris, J. Birch, R. Marin, S. Jensen, B. Roman, C. Everlove, A. Makarewicz, V. Riot, D. Hadley, W. Benett, and J. Dzenitis, "Development of Ecogenomic Sensors for Remote Detection of Marine Microbes, Their Genes and Gene Products," *AGU Fall Meet. Abstr.*, vol. -1, p. 0357, Dec. 2008.

[12] C. Scholin, G. Massion, E. Mellinger, M. Brown, D. Wright, and D. Cline, "The development and application of molecular probes and novel instrumentation for detection of harmful algae," 1998, vol. 1, pp. 367–370.

[13] C. Scholin, E. Massion, and D. Wright, "Aquatic autosampler device," 6,187,5302001.

[14] J. Paul, "In situ instrumentation," 2007.

[15] C. Scholin, G. Doucette, S. Jensen, B. Roman, D. Pargett, R. M. Iii, C. Preston, W. Jones, J. Feldman, C. Everlove, A. Harris, N. Alvarado, E. Massion, J. Birch, D. Greenfield, R. Vrijenhoek, C. Mikulski, and K. Jones, "Remote Detection of Marine Microbes, Small Invertebrates, Harmful Algae, and Biotoxins using the Environmental Sample Processor (ESP)," *Oceanography*, vol. v.22(2), Jun. 2009.

[16] B. Roman, C. Scholin, S. Jensen, R. Marin, E. Massion, and J. Feldman, "The 2nd Generatilon Environmental Sample Processor:- Evolution of a Robot'ic Underwater Biochemilcal Laboratory," in *Proceedings of OCEANS 2005 MTS/IEEE*, 2005, pp. 1–9.

[17] C. Scholin, R. Marin III, E. Massion, S. Jensen, D. Cline, B. Roman, and G. Doucette, "Remote detection of HAB species using the environmental sample processor (ESP): Progress and future directions," 2002, pp. 21–25.

[18] S. K. Goffredi, W. J. Jones, C. A. Scholin, R. M. Iii, and R. C. Vrijenhoek, "Molecular Detection of Marine Invertebrate Larvae," *Mar. Biotechnol.*, vol. 8, no. 2, pp. 149–160, Apr. 2006.

[19] "Environmental Sample Processor Home." [Online]. Available: http://www.mbari.org/esp/.

[20] C. M. Preston, A. Harris, J. P. Ryan, B. Roman, R. Marin, S. Jensen, C. Everlove, J. Birch, J. M. Dzenitis, D. Pargett, M. Adachi, K. Turk, J. P. Zehr, and C. A. Scholin, "Underwater Application of Quantitative PCR on an Ocean Mooring," *PLoS One*, vol. 6, no. 8, p. e22522, Aug. 2011.

[21] P. Belgrader, C. J. Elkin, S. B. Brown, S. N. Nasarabadi, R. G. Langlois, F. P. Milanovich, B. W. Colston, and G. D. Marshall, "A Reusable Flow-Through Polymerase Chain Reaction Instrument for the Continuous Monitoring of Infectious Biological Agents," *Anal. Chem.*, vol. 75, no. 14, pp. 3446–3450, Jul. 2003.

[22] J. B. J. Harvey, J. P. Ryan, R. Marin III, C. M. Preston, N. Alvarado, C. A. Scholin, and R. C. Vrijenhoek, "Robotic sampling, in situ monitoring and molecular detection of marine zooplankton," *J. Exp. Mar. Bio. Ecol.*, vol. 413, pp. 60–70, Feb. 2012.

[23] MBARI, "Long-range autonomous underwater vehicle Tethys." [Online]. Available: http://www.mbari.org/auv/LRAUV.htm.

[24] R. Dahm, "Discovering DNA: Friedrich Miescher and the early years of nucleic acid research," *Hum. Genet.*, vol. 122, no. 6, pp. 565–581, Jan. 2008.

[25] K. B. Mullis, "The unusual origin of the polymerase chain reaction," *Sci. Am.*, vol. 262, no. 4, pp. 56–61, 64–65, Apr. 1990.

[26] R. Higuchi, C. Fockler, G. Dollinger, and R. Watson, "Kinetic PCR Analysis: Real-time Monitoring of DNA Amplification Reactions," *Nat. Biotechnol.*, vol. 11, no. 9, pp. 1026–1030, Sep. 1993.

[27] R. G. Rutledge, "Mathematics of quantitative kinetic PCR and the application of standard curves," *Nucleic Acids Res.*, vol. 31, no. 16, p. 93e–93, Aug. 2003.

[28] S. L. Anna, N. Bontoux, and H. a. Stone, "Formation of dispersions using 'flow focusing' in microchannels," *Appl. Phys. Lett.*, vol. 82, no. 3, p. 364, 2003.

[29] F. Leal-Calderon and P. Poulin, "Progress in understanding emulsion metastability and surface forces," *Curr. Opin. Colloid Interface Sci.*, vol. 4, no. 3, pp. 223–230, Jun. 1999.

[30] H. N. Joensson and H. Andersson Svahn, “Droplet microfluidics--a tool for single-cell analysis.,” *Angew. Chem. Int. Ed. Engl.*, vol. 51, no. 49, pp. 12176–92, Dec. 2012.

[31] J. Lederberg, “A simple method for isolating individual microbes,” *J. Bacteriol.*, vol. 68, no. 2, pp. 258–259, 1954.

[32] Q. Ge, P. Yu, Y. Bai, and Z. Lu, “An emulsion system based on a chip polymerase chain reaction.,” *Molecules*, vol. 13, no. 12, pp. 3057–68, Jan. 2008.

[33] K. Shao, W. Ding, F. Wang, H. Li, D. Ma, and H. Wang, “Emulsion PCR: a high efficient way of PCR amplification of random DNA libraries in aptamer selection.,” *PLoS One*, vol. 6, no. 9, p. e24910, Jan. 2011.

[34] A. B. Theberge, F. Courtois, Y. Schaerli, M. Fischlechner, C. Abell, F. Hollfelder, and W. T. S. Huck, “Microdroplets in microfluidics: an evolving platform for discoveries in chemistry and biology.,” *Angew. Chem. Int. Ed. Engl.*, vol. 49, no. 34, pp. 5846–68, Aug. 2010.

[35] B. Vogelstein and K. W. Kinzler, “Digital PCR.,” *Proc. Natl. Acad. Sci. U. S. A.*, vol. 96, no. 16, pp. 9236–41, Aug. 1999.

[36] S. Dube, J. Qin, and R. Ramakrishnan, “Mathematical analysis of copy number variation in a DNA sample using digital PCR on a nanofluidic device.,” *PLoS One*, vol. 3, no. 8, p. e2876, Jan. 2008.

[37] D. Mark, S. Haeberle, G. Roth, F. von Stetten, and R. Zengerle, “Microfluidic lab-on-a-chip platforms: requirements, characteristics and applications.,” *Chem. Soc. Rev.*, vol. 39, no. 3, pp. 1153–82, Mar. 2010.

[38] G. M. Whitesides, “The origins and the future of microfluidics.,” *Nature*, vol. 442, no. 7101, pp. 368–73, Jul. 2006.

[39] L. Y. Yeo, H.-C. Chang, P. P. Y. Chan, and J. R. Friend, “Microfluidic devices for bioapplications.,” *Small*, vol. 7, no. 1, pp. 12–48, Jan. 2011.

[40] K. Kolari, “Fabrication of silicon and glass devices for microfluidic bioanalytical applications,” Helsinki University of Technology, 2008.

[41] D. J. Beebe, G. A. Mensing, and G. M. Walker, “Physics and Applications of Microfluidics in Biology,” *Annu. Rev. Biomed. Eng.*, vol. 4, no. 1, pp. 261–286, 2002.

[42] S. C. Jakeway, A. J. de Mello, and E. L. Russell, “Miniaturized total analysis systems for biological analysis,” *Fresenius. J. Anal. Chem.*, vol. 366, no. 6–7, pp. 525–539, Mar. 2000.

[43] T. Chován and A. Guttman, “Microfabricated devices in biotechnology and biochemical processing,” *Trends Biotechnol.*, vol. 20, no. 3, pp. 116–122, Mar. 2002.

[44] S. K. Sia and L. J. Kricka, “Microfluidics and point-of-care testing,” *Lab Chip*, vol. 8, no. 12, p. 1982, 2008.

[45] C. Zhang, J. Xu, W. Ma, and W. Zheng, “PCR microfluidic devices for DNA amplification.,” *Biotechnol. Adv.*, vol. 24, no. 3, pp. 243–84, 2006.

[46] C. Zhang and D. Xing, “Miniaturized PCR chips for nucleic acid amplification and analysis: latest advances and future trends.,” *Nucleic Acids Res.*, vol. 35, no. 13, pp. 4223–37, Jan. 2007.

[47] Y. Zhang and P. Ozdemir, “Microfluidic DNA amplification--a review.,” *Anal. Chim. Acta*, vol. 63, no. 2, pp. 115–25, Apr. 2009.

[48] K. M. Horsman, J. M. Bienvenue, K. R. Blasier, and J. P. Landers, “Forensic DNA Analysis on Microfluidic Devices: A Review,” *J. Forensic Sci.*, vol. 52, no. 4, pp. 784–799, 2007.

[49] S. Neethirajan, I. Kobayashi, M. Nakajima, D. Wu, S. Nandagopal, and F. Lin, “Microfluidics for food, agriculture and biosystems industries.,” *Lab Chip*, vol. 11, no. 9, pp. 1574–86, May 2011.

[50] H. N. Joensson and H. Andersson-Svahn, “Droplet microfluidics—a tool for protein engineering and analysis,” *Lab Chip*, 2011.

[51] G. Velve-Casquillas, M. Le Berre, M. Piel, and P. T. Tran, “Microfluidic tools for cell biological research.,” *Nano Today*, vol. 5, no. 1, pp. 28–47, Feb. 2010.

[52] A. Manz, N. Graber, and H. M. Widmer, “Miniaturized total chemical analysis systems: A novel concept for chemical sensing,” *Sensors Actuators B Chem.*, vol. 1, no. 1–6, pp. 244–248, Jan. 1990.

[53] D. Erickson and D. Li, “Integrated microfluidic devices,” *Anal. Chim. Acta*, vol. 507, no. 1, pp. 11–26, Apr. 2004.

[54] H. Gau, S. Herminghaus, P. Lenz, and R. Lipowsky, “Liquid morphologies on structured surfaces: from microchannels to microchips,” *Science*, vol. 283, no. 5398, pp. 46–9, Jan. 1999.

[55] D. Kataoka and S. Troian, “Patterning liquid flow on the microscopic scale,” *Nature*, vol. 402, no. December, pp. 8–11, 1999.

[56] B. Zhao, J. S. Moore, and D. J. Beebe, “Surface-directed liquid flow inside microchannels.,” *Science*, vol. 291, no. 5506, pp. 1023–6, Feb. 2001.

[57] B. Zhao, J. S. Moore, and D. J. Beebe, “Pressure-Sensitive Microfluidic Gates Fabricated by Patterning Surface Free Energies Inside Microchannels,” no. 17, pp. 1873–1879, 2003.

[58] T. Thorsen, R. Roberts, F. Arnold, and S. Quake, “Dynamic Pattern Formation in a Vesicle-Generating Microfluidic Device,” *Phys. Rev. Lett.*, vol. 86, no. 18, pp. 4163–4166, Apr. 2001.

[59] T. Squires and S. Quake, “Microfluidics: Fluid physics at the nanoliter scale,” *Rev. Mod. Phys.*, vol. 77, no. 3, pp. 977–1026, Oct. 2005.

[60] J.-C. Baret, “Surfactants in droplet-based microfluidics.,” *Lab Chip*, vol. 12, no. 3, pp. 422–33, Feb. 2012.

[61] C. N. Baroud, F. Gallaire, and R. Dangla, “Dynamics of microfluidic droplets.,” *Lab Chip*, vol. 10, no. 16, pp. 2032–45, Aug. 2010.

[62] M. J. Fuerstman, A. Lai, M. E. Thurlow, S. S. Shevkoplyas, H. a Stone, and G. M. Whitesides, “The pressure drop along rectangular microchannels containing bubbles.,” *Lab Chip*, vol. 7, no. 11, pp. 1479–89, Nov. 2007.

[63] H. Song, J. Tice, and R. Ismagilov, “A Microfluidic System for Controlling Reaction Networks in Time,” *Angew. Chemie*, pp. 767–772, 2003.

[64] L. W. Schwartz, H. M. Princen, and A. D. Kiss, “On the motion of bubbles in capillary tubes,” *J. Fluid Mech.*, vol. 172, pp. 259–275, Apr. 1986.

[65] H. Wong, C. J. Radke, and S. Morris, “The motion of long bubbles in polygonal capillaries. Part 2. Drag, fluid pressure and fluid flow,” *J. Fluid Mech.*, vol. 292, no. -1, p. 95, Apr. 2006.

[66] F. Sarrazin, T. Bonometti, L. Prat, C. Gourdon, and J. Magnaudet, “Hydrodynamic structures of droplets engineered in rectangular micro-channels,” *Microfluid. Nanofluidics*, vol. 5, no. 1, pp. 131–137, Oct. 2007.

[67] R. B. Fair, V. Srinivasan, H. Ren, P. Paik, V. K. Pamula, and M. G. Pollack, “Electrowetting-based on-chip sample processing for integrated microfluidics,” in *IEEE International Electron Devices Meeting 2003*, pp. 32.5.1–32.5.4.

[68] S.-Y. Teh, R. Lin, L.-H. Hung, and A. P. Lee, “Droplet microfluidics.,” *Lab Chip*, vol. 8, no. 2, pp. 198–220, Feb. 2008.

[69] C. Cramer, P. Fischer, and E. J. Windhab, “Drop formation in a co-flowing ambient fluid,” *Chem. Eng. Sci.*, vol. 59, no. 15, pp. 3045–3058, Aug. 2004.

[70] R. Dreyfus, P. Tabeling, and H. Willaime, “Ordered and Disordered Patterns in Two-Phase Flows in Microchannels,” *Phys. Rev. Lett.*, vol. 90, no. 14, p. 144505, Apr. 2003.

[71] P. Garstecki, I. Gitlin, W. DiLuzio, G. M. Whitesides, E. Kumacheva, and H. a. Stone, “Formation of monodisperse bubbles in a microfluidic flow-focusing device,” *Appl. Phys. Lett.*, vol. 85, no. 13, p. 2649, 2004.

[72] S. R. Hodges, O. E. Jensen, and J. M. Rallison, “The motion of a viscous drop through a cylindrical tube,” *J. Fluid Mech.*, vol. 501, pp. 279–301, Feb. 2004.

[73] H. Song, M. R. Bringer, J. D. Tice, C. J. Gerdts, and R. F. Ismagilov, “Experimental test of scaling of mixing by chaotic advection in droplets moving through microfluidic channels.,” *Appl. Phys. Lett.*, vol. 83, no. 12, pp. 4664–4666, Dec. 2003.

[74] N. Bremond, A. Thiam, and J. Bibette, “Decompressing Emulsion Droplets Favors Coalescence,” *Phys. Rev. Lett.*, vol. 100, no. 2, pp. 1–4, Jan. 2008.

[75] X. Niu, S. Gulati, J. B. Edel, and A. J. deMello, “Pillar-induced droplet merging in microfluidic circuits.,” *Lab Chip*, vol. 8, no. 11, pp. 1837–41, Nov. 2008.

[76] H. Aryafar and H. P. Kavehpour, “Electrocoalescence: effects of DC electric fields on coalescence of drops at planar interfaces.,” *Langmuir*, vol. 25, no. 21, pp. 12460–5, Nov. 2009.

[77] M. Zagnoni and J. M. Cooper, “On-chip electrocoalescence of microdroplets as a function of voltage, frequency and droplet size.,” *Lab Chip*, vol. 9, no. 18, pp. 2652–8, Sep. 2009.

[78] X. Niu, F. Gielen, A. J. deMello, and J. B. Edel, “Electro-coalescence of digitally controlled droplets.,” *Anal. Chem.*, vol. 81, no. 17, pp. 7321–5, Sep. 2009.

[79] H. Gu, M. H. G. Duits, and F. Mugele, “Droplets formation and merging in two-phase flow microfluidics.,” *Int. J. Mol. Sci.*, vol. 12, no. 4, pp. 2572–97, Jan. 2011.

[80] C. Priest, S. Herminghaus, and R. Seemann, “Controlled electrocoalescence in microfluidics: Targeting a single lamella,” *Appl. Phys. Lett.*, vol. 89, no. 13, p. 134101, 2006.

[81] M. Zagnoni, G. Le Lain, and J. M. Cooper, “Electrocoalescence mechanisms of microdroplets using localized electric fields in microfluidic channels.,” *Langmuir*, vol. 26, no. 18, pp. 14443–9, Sep. 2010.

[82] A. M. Huebner, C. Abell, W. T. S. Huck, C. N. Baroud, and F. Hollfelder, “Monitoring a reaction at submillisecond resolution in picoliter volumes.,” *Anal. Chem.*, vol. 83, no. 4, pp. 1462–8, Feb. 2011.

[83] D. J. Harrison, P. G. Glavina, and A. Manz, “Towards miniaturized electrophoresis and chemical analysis systems on silicon: an alternative to chemical sensors,” *Sensors Actuators B Chem.*, vol. 10, no. 2, pp. 107–116, Jan. 1993.

[84] N. Layadi, J. I. Colonell, and J. T. Lee, “An introduction to plasma etching for VLSI circuit technology,” *Bell Labs Tech. J.*, vol. 4, no. 3, pp. 155–171, Aug. 2002.

[85] P. Jothimuthu, A. Carroll, A. A. S. Bhagat, G. Lin, J. E. Mark, and I. Papautsky, "Photodefinable PDMS thin films for microfabrication applications," *J. Micromechanics Microengineering*, vol. 19, no. 4, p. 045024, Apr. 2009.

[86] K. Tsougeni, A. Tserepi, and E. Gogolides, "Photosensitive poly(dimethylsiloxane) materials for microfluidic applications," *Microelectron. Eng.*, vol. 84, no. 5–8, pp. 1104–1108, May 2007.

[87] J. H. Koschwanez, R. H. Carlson, and D. R. Meldrum, "Thin PDMS films using long spin times or tert-butyl alcohol as a solvent.," *PLoS One*, vol. 4, no. 2, p. e4572, Jan. 2009.

[88] A. Piruska, I. Nikcevic, S. H. Lee, C. Ahn, W. R. Heineman, P. a Limbach, and C. J. Seliskar, "The autofluorescence of plastic materials and chips measured under laser irradiation.," *Lab Chip*, vol. 5, no. 12, pp. 1348–54, Dec. 2005.

[89] R. Mukhopadhyay, "When PDMS isn't the best," *Anal. Chem.*, vol. 79, no. 9, pp. 3248–3253, 2007.

[90] C. Zhang and D. Xing, "Single-molecule DNA amplification and analysis using microfluidics.," *Chem. Rev.*, vol. 110, no. 8, pp. 4910–47, Aug. 2010.

[91] C. Adessi, "Solid phase DNA amplification: characterisation of primer attachment and amplification mechanisms," *Nucleic Acids Res.*, vol. 28, no. 20, p. 87e–87, Oct. 2000.

[92] A. Pemov, H. Modi, D. P. Chandler, and S. Bavykin, "DNA analysis with multiplex microarray-enhanced PCR.," *Nucleic Acids Res.*, vol. 33, no. 2, p. e11, Jan. 2005.

[93] T. H. Fang, N. Ramalingam, D. Xian-Dui, T. S. Ngin, Z. Xianting, A. T. Lai Kuan, E. Y. Peng Huat, and G. Hai-Qing, "Real-time PCR microfluidic devices with concurrent electrochemical detection.," *Biosens. Bioelectron.*, vol. 24, no. 7, pp. 2131–6, Mar. 2009.

[94] M. Pieprzyk and H. High, "Fluidigm Dynamic Arrays provide a platform for single- cell gene expression analysis," *Nat. Methods*, vol. 6, no. 7, pp. iii–iv, 2009.

[95] J. Kim, J. Lee, S. Seong, S. Cha, S. Lee, and T. Park, "Fabrication and characterization of a PDMS–glass hybrid continuous-flow PCR chip," *Biochem. Eng. J.*, vol. 29, no. 1–2, pp. 91–97, Apr. 2006.

[96] N. Park, S. Kim, and J. H. Hahn, “Cylindrical Compact Thermal-Cycling Device for Continuous-Flow Polymerase Chain Reaction,” *Anal. Chem.*, vol. 75, no. 21, pp. 6029–6033, Nov. 2003.

[97] T. Lund-Olesen, M. Dufva, J. A. Dahl, P. Collas, and M. F. Hansen, “Sensitive on-chip quantitative real-time PCR performed on an adaptable and robust platform.,” *Biomed. Microdevices*, vol. 10, no. 6, pp. 769–76, Dec. 2008.

[98] R. M. Lorenz, G. S. Fiorini, G. D. M. Jeffries, D. S. W. Lim, M. He, and D. T. Chiu, “Simultaneous generation of multiple aqueous droplets in a microfluidic device.,” *Anal. Chim. Acta*, vol. 630, no. 2, pp. 124–30, Dec. 2008.

[99] M. S. Munson and P. Yager, “Simple quantitative optical method for monitoring the extent of mixing applied to a novel microfluidic mixer,” *Anal. Chim. Acta*, vol. 507, no. 1, pp. 63–71, Apr. 2004.

[100] C. H. Lee and K. Jiang, “Fabrication of thick electroforming micro mould using a KMPR negative tone photoresist,” *J. Micromechanics Microengineering*, vol. 18, no. 5, p. 055032, May 2008.

[101] T. Ray, H. Zhu, I. Elango, and D. Meldrum, “Characterization of KMPR® 1025 as a masking layer for deep reactive ion etching of fused silica,” in *Micro Electro Mechanical Systems (MEMS), 2011 IEEE 24th International Conference on*, 2011, pp. 213–216.

[102] I. Rodriguez, M. Lesaicherre, Y. Tie, Q. Zou, C. Yu, J. Singh, L. T. Meng, S. Uppili, S. F. Y. Li, P. Gopalakrishnakone, and Z. E. Selvanayagam, “Practical integration of polymerase chain reaction amplification and electrophoretic analysis in microfluidic devices for genetic analysis.,” *Electrophoresis*, vol. 24, no. 1–2, pp. 172–8, Jan. 2003.

[103] P. Mary, L. Dauphinot, N. Bois, M.-C. Potier, V. Studer, and P. Tabeling, “Analysis of gene expression at the single-cell level using microdroplet-based microfluidic technology.,” *Biomicrofluidics*, vol. 5, no. 2, p. 24109, Jun. 2011.

[104] L. S. Roach, H. Song, and R. F. Ismagilov, “Controlling nonspecific protein adsorption in a plug-based microfluidic system by controlling interfacial chemistry using fluorous-phase surfactants.,” *Anal. Chem.*, vol. 77, no. 3, pp. 785–96, Feb. 2005.

[105] A. B. Theberge, E. Mayot, A. El Harrak, F. Kleinschmidt, W. T. S. Huck, and A. D. Griffiths, "Microfluidic platform for combinatorial synthesis in picolitre droplets," *Lab Chip*, 2012.

[106] T. Rane, H. Zec, C. Puleo, and A. Lee, "High-throughput single-cell pathogen detection on a droplet microfluidic platform," in *Micro Electro Mechanical Systems (MEMS), 2011 IEEE 24th International Conference on*, 2011, pp. 881–884.

[107] N. R. Beer, B. J. Hindson, E. K. Wheeler, B. Sara, K. A. Rose, I. M. Kennedy, and B. W. Colston, "On-chip, real-time, single-copy polymerase chain reaction in picoliter droplets," *Anal. Chem.*, vol. 79, no. 22, pp. 8471–8475, 2007.

[108] Y. Schaerli, R. C. Wootton, T. Robinson, V. Stein, C. Dunsby, M. a a Neil, P. M. W. French, A. J. Demello, C. Abell, and F. Hollfelder, "Continuous-flow polymerase chain reaction of single-copy DNA in microfluidic microdroplets.," *Anal. Chem.*, vol. 81, no. 1, pp. 302–6, Jan. 2009.

[109] F. Wang and M. a Burns, "Performance of nanoliter-sized droplet-based microfluidic PCR," *Biomed. Microdevices*, pp. 1071–1080, May 2009.

[110] Z. Hua, J. L. Rouse, A. E. Eckhardt, V. Srinivasan, V. K. Pamula, W. a Schell, J. L. Benton, T. G. Mitchell, and M. G. Pollack, "Multiplexed real-time polymerase chain reaction on a digital microfluidic platform.," *Anal. Chem.*, vol. 82, no. 6, pp. 2310–6, Mar. 2010.

[111] Z. Qi, Y. Ma, L. Deng, H. Wu, G. Zhou, T. Kajiyama, and H. Kambara, "Digital analysis of the expression levels of multiple colorectal cancer-related genes by multiplexed digital-PCR coupled with hydrogel bead-array.," *Analyst*, vol. 136, no. 11, pp. 2252–9, Jun. 2011.

[112] P. Kumaresan, C. J. Yang, S. a Cronier, R. G. Blazej, and R. a Mathies, "High-throughput single copy DNA amplification and cell analysis in engineered nanoliter droplets.," *Anal. Chem.*, vol. 80, no. 10, pp. 3522–9, May 2008.

[113] L. Mazutis, A. F. Araghi, O. J. Miller, J.-C. Baret, L. Frenz, A. Janoshazi, V. Taly, B. J. Miller, J. B. Hutchison, D. Link, A. D. Griffiths, and M. Ryckelynck, "Droplet-based microfluidic systems for high-throughput single DNA molecule isothermal amplification and analysis.," *Anal. Chem.*, vol. 81, no. 12, pp. 4813–21, Jun. 2009.

[114] M. Chabert, K. D. Dorfman, P. de Cremoux, J. Roeraade, and J.-L. Viovy, "Automated microdroplet platform for sample manipulation and polymerase chain reaction.," *Anal. Chem.*, vol. 78, no. 22, pp. 7722–8, Nov. 2006.

[115] D. M. Lemal, "Perspective on fluorocarbon chemistry.," *J. Org. Chem.*, vol. 69, no. 1, pp. 1–11, Jan. 2004.

[116] K. P. Johnston, T. Randolph, F. Bright, and S. Howdle, "Toxicology of a PFPE Surfactant.," *Science*, vol. 272, no. 5269, p. 1726b, Jun. 1996.

[117] J.-C. Baret, F. Kleinschmidt, A. El Harrak, and A. D. Griffiths, "Kinetic aspects of emulsion stabilization by surfactants: a microfluidic analysis.," *Langmuir*, vol. 25, no. 11, pp. 6088–93, Jun. 2009.

[118] Y. Skhiri, P. Gruner, B. Semin, Q. Brosseau, D. Pekin, L. Mazutis, V. Goust, F. Kleinschmidt, A. El Harrak, J. B. Hutchison, E. Mayot, J.-F. Bartolo, A. D. Griffiths, V. Taly, and J.-C. Baret, "Dynamics of molecular transport by surfactants in emulsions," *Soft Matter*, vol. 8, no. 41, p. 10618, 2012.

[119] D. L. Chen, L. Li, S. Reyes, D. N. Adamson, and R. F. Ismagilov, "Using three-phase flow of immiscible liquids to prevent coalescence of droplets in microfluidic channels: criteria to identify the third liquid and validation with protein crystallization.," *Langmuir*, vol. 23, no. 4, pp. 2255–60, Feb. 2007.

[120] A. R. Abate, J. Thiele, and D. a Weitz, "One-step formation of multiple emulsions in microfluidics.," *Lab Chip*, vol. 11, no. 2, pp. 253–8, Jan. 2011.

[121] E. Fradet, C. McDougall, P. Abbyad, R. Dangla, D. McGloin, and C. N. Baroud, "Combining rails and anchors with laser forcing for selective manipulation within 2D droplet arrays.," *Lab Chip*, vol. 11, no. 24, pp. 4228–34, Dec. 2011.

[122] "SMDuino." [Online]. Available: https://code.google.com/p/smduino/.

[123] A. L. Markey, S. Mohr, and P. J. R. Day, "High-throughput droplet PCR.," *Methods*, vol. 50, no. 4, pp. 277–81, Apr. 2010.

[124] K. D. Dorfman, M. Chabert, J.-H. Codarbox, G. Rousseau, P. de Cremoux, and J.-L. Viovy, "Contamination-free continuous flow microfluidic polymerase chain reaction for quantitative and clinical applications.," *Anal. Chem.*, vol. 77, no. 11, pp. 3700–4, Jun. 2005.

[125] V. Linder, E. Verpoorte, W. Thormann, N. F. de Rooij, and H. Sigrist, “Surface biopassivation of replicated poly(dimethylsiloxane) microfluidic channels and application to heterogeneous immunoreaction with on-chip fluorescence detection.,” *Anal. Chem.*, vol. 73, no. 17, pp. 4181–9, Sep. 2001.

[126] a Dodge, K. Fluri, E. Verpoorte, and N. F. de Rooij, “Electrokinetically driven microfluidic chips with surface-modified chambers for heterogeneous immunoassays.,” *Anal. Chem.*, vol. 73, no. 14, pp. 3400–9, Jul. 2001.

[127] D. Juncker, H. Schmid, U. Drechsler, H. Wolf, M. Wolf, B. Michel, N. de Rooij, and E. Delamarche, “Autonomous microfluidic capillary system.,” *Anal. Chem.*, vol. 74, no. 24, pp. 6139–44, Dec. 2002.